THE HONG KONG
POLYTECHNIC UNIVERSITY
香港理工大學
Pao Yue-kong Library
包玉剛圖書館

Copyright Undertaking

This thesis is protected by copyright, with all rights reserved.

By reading and using the thesis, the reader understands and agrees to the following terms:

1. The reader will abide by the rules and legal ordinances governing copyright regarding the use of the thesis.
2. The reader will use the thesis for the purpose of research or private study only and not for distribution or further reproduction or any other purpose.
3. The reader agrees to indemnify and hold the University harmless from and against any loss, damage, cost, liability or expenses arising from copyright infringement or unauthorized usage.

IMPORTANT

If you have reasons to believe that any materials in this thesis are deemed not suitable to be distributed in this form, or a copyright owner having difficulty with the material being included in our database, please contact lbsys@polyu.edu.hk providing details. The Library will look into your claim and consider taking remedial action upon receipt of the written requests.

Pao Yue-kong Library, The Hong Kong Polytechnic University, Hung Hom, Kowloon, Hong Kong

http://www.lib.polyu.edu.hk

IN-SITU TRANSMISSION ELECTRON MICROSCOPY CHARACTERIZATIONS ON DYNAMICAL PROPERTIES OF TWO-DIMENSIONAL MATERIALS

ZHENG FANGYUAN

PhD

The Hong Kong Polytechnic University

2021

The Hong Kong Polytechnic University

Department of Applied Physics

In-Situ Transmission Electron Microscopy Characterizations on Dynamical Properties of Two-Dimensional Materials

ZHENG Fangyuan

A thesis submitted in partial fulfillment of the requirements for the degree of Doctor of Philosophy

August 2021

CERTIFICATE OF ORIGINALITY

I hereby declare that this thesis is my own work and that, to the best of my knowledge and belief, it reproduces no material previously published or written, nor material that has been accepted for the award of any other degree or diploma, except where due acknowledgement has been made in the text.

_____ (Signed)

_____ZHENG Fangyuan_____(Name of student)

ABSTRACT

During the past decade, two-dimensional (2D) materials are under explosive growth. They are well known for having extraordinary mechanical, chemical, electrical and optical properties owing to their ultrathin structures and outstanding flexibilities. Apart from the most popular 2D materials such as graphene or hexagonal boron nitride, transition metal dichalcogenides (TMDs), as a big 2D family, also have a wide range of applications for high electron mobility and extraordinary mechanical properties. All these physical features are related to bandgaps and directly decided by their atomic structures. Therefore, observation of atomic structures under the effect of strain provides the intrinsic understanding of dynamically related properties in 2D materials.

In this thesis, four types of mechanical behaviors in dimensional order are identified with the change of atomic structures in 2D materials: grain boundaries (GBs) (1D), phase transition (2D), fracture (2D) and wrinkling (3D). The pristine 2D materials in experiments include graphene, MoS_2 and ReS_2. With the help of scanning transmission electron microscopy (STEM), continuous change of crystal lattice can be observed in nanoscale. Electron beam irradiation from (S)TEM provides the energy to introduce strain on monolayer materials under atomic resolution and at the same time, scanning tunneling microscopy (STM) applies direct strain for lower magnification deformation and electrical tests. Related statistics, modeling and DFT calculation are conducted to explain the mechanism behind experimental phenomenon. In monolayer ReS_2, a systematic classification of mobile and pinned GBs is clarified. According to the high/low crystal plane index and whether the rhenium atomic arrangements on both sides of GBs are consistent or not, the GBs in ReS_2 can be divided into four categories and more detailed types. With similar *in situ* method,

electron beam drives phase transition on ReS_2 by creating atomic defects and introducing strain, the atomic structure of secondary phase is clearly observed. Apart from this, fracture process and cracks extension are also observed under electron beam irradiation, while the lattice reconstruction occurs on the tip of the crack under the influence of shear stress. The continuous deformation and van der Waals (vdW) force influence in wrinkling are observed when a monolayer graphene being cracked from its multilayer flake. Thus the critical length of stable wrinkles is calculated from the wrinkling and wrinkle elimination process.

In conclusion, *in situ* (S)TEM is employed as an ideal method to measure the mechanical properties of 2D materials. The present works shed light on the future mechanical engineering, facilitating the high strength and high toughness as well as potential functionalities in 2D materials.

LIST OF PUBLICATIONS

(1) Fangyuan Zheng, Lingli Huang, Lok-Wing Wong, Jin Han, Yuan Cai, Ning Wang, Qingming Deng, Thuc Hue Ly, and Jiong Zhao, "The Mobile and Pinned Grain Boundaries in 2D Monoclinic Rhenium Disulfide", **Advanced Science**, 2020, 7(22), 2001742.

(2) Fangyuan Zheng, Wai Chung Lam, Ka Hei Lai, Lingli Huang, Lok Wing Wong, Yisong Zhang, Zhangyuan Yan, Chak Chung Sham, Quoc Huy Thi, Thuc Hue Ly, and Jiong Zhao, "Synchronized Structure and Surface Tension Measurement on Individual Secondary Aerosol Particles by Low-Voltage Transmission Electron Microscopy", **Environmental Science & Technology Letters,** 2020, 7(8), 560-566.

(3) Fangyuan Zheng, Quoc Huy Thi, Lok Wing Wong, Qingming Deng, Thuc Hue Ly, and Jiong Zhao, "Critical Stable Length in Wrinkles of Two-Dimensional Materials", **ACS Nano**, 2020, 14(2), 2137–2144.

(4) Fangyuan Zheng, Lok Wing Wong, Jiong Zhao, and Thuc Hue Ly, "A Novel Class of Two-Dimensional Materials: Transition Metal Dichalcogenides", **21st Century Nanoscience–A Handbook**, 2020, 6-1-6-25.

(5) Lingli Huang, Fangyuan Zheng, Qingming Deng, Quoc Huy Thi, Lok Wing Wong, Yuan Cai, Ning Wang, Chun-Sing Lee, Shu Ping Lau, Manish Chhowalla, Ju Li, Thuc Hue Ly, and Jiong Zhao, "In Situ Scanning Transmission Electron Microscopy Observations of Fracture at the Atomic Scale", **Physical review letters**, 2020, 125(24), 246102.

(6) Lingli Huang, Fangyuan Zheng, Qingming Deng, Quoc Huy Thi, Lok Wing Wong, Yuan Cai, Ning Wang, Chun-Sing Lee, Shu Ping Lau, Thuc Hue Ly, and Jiong Zhao, "Anomalous fracture in two-dimensional rhenium disulfide", **Science advances**, 2020, 6(47), eabc2282.

(7) Tianyue Wang, Fangyuan Zheng, Guanqi Tang, Jiupeng Cao, Peng You, Jiong Zhao, and Feng Yan, "2D WSe2 Flakes for Synergistic Modulation of Grain Growth and Charge Transfer in Tin-Based Perovskite Solar Cells", **Advanced Science**, 2021, 2004315.

(8) Lingli Huang, Quoc Huy Thi, Fangyuan Zheng, Xin Chen, Yee Wa Chu, Chun-Sing Lee, Jiong Zhao, and Thuc Hue Ly, "Catalyzed Kinetic Growth in Two-Dimensional MoS2", **Journal of the American Chemical Society**, 2020, 142(30), 13130-13135.

(9) Lok-Wing Wong, Lingli Huang, Fangyuan Zheng, Quoc Huy Thi, Jiong Zhao, Qingming Deng, and Thuc Hue Ly, "Site-specific electrical contacts with the two-dimensional materials", **Nature communications**, 2020, 11(1), 1-10.

(10) Xiandi Zhang, Jia Yan, Fangyuan Zheng, Jiong Zhao, and Lawrence Yoon Suk Lee, "Designing charge transfer route at the interface between WP nanoparticle and g-C3N4 for highly enhanced photocatalytic CO2 reduction reaction", **Applied Catalysis B: Environmental**, 2021, 286, 119879.

(11) Lingli Huang, Tiefeng Yang, Lok Wing Wong, Fangyuan Zheng, Xin Chen, Ka Hei Lai, Haijun Liu, Quoc Huy Thi, Dong Shen, Chun-Sing Lee, Qingming Deng, Jiong Zhao, and Thuc Hue Ly, "Redox Photochemistry on Van Der Waals Surfaces for Reversible Doping in 2D Materials" **Advanced Functional Materials**, 2021, 31(16), 2009166.

(12) Mengjie Liu, Jeongyeon Lee, Tsung-Cheng Yang, Fangyuan Zheng, Jiong Zhao, Chia-Min Yang, and Lawrence Yoon Suk Lee, "Synergies of Fe Single Atoms and Clusters on N-

Doped Carbon Electrocatalyst for pH-Universal Oxygen Reduction", **Small Methods**, 2021, 5(5), 2001165.

(13) Jiupeng Cao, Guanqi Tang, Peng You, Tianyue Wang, Fangyuan Zheng, Jiong Zhao, and Feng Yan, "Enhanced Performance of Planar Perovskite Solar Cells Induced by Van Der Waals Epitaxial Growth of Mixed Perovskite Films on WS2 Flakes", **Advanced Functional Materials**, 2020, 30(38), 2002358.

(14) Guanqi Tang, Peng You, Qidong Tai, Anneng Yang, Jiupeng Cao, Fangyuan Zheng, Zhiwen Zhou, Jiong Zhao, Paddy Kwok Leung Chan, and Feng Yan, "Solution-Phase Epitaxial Growth of Perovskite Films on 2D Material Flakes for High-Performance Solar Cells", **Advanced Materials**, 2019, 31(24), 1807689.

ACKNOWLEDGEMENTS

This thesis is based on the works I carried out as a Ph.D. student in Department of Applied Physics of the Hong Kong Polytechnic University, Dr. Jiong ZHAO's group. The achievements of these works are under the help of countless researchers including my advisor, my group members, and our cooperation groups. Here, I am showing my grateful appreciates and best wishes to them.

Firstly, I would like to express my sincere gratitude to my supervisor, Dr. Jiong ZHAO, for his noble guidance, invaluable assistance, and support with full encouragement. From my first day in our laboratory to all the following discovery and analysis, Dr. Zhao always teaches me in person and provides profound insights. He also shares with us his experience as a Ph.D. student and the spirits of being a good researcher. I am deeply enlightened by his enthusiasm on science and feel honored to start my academic research under such an advisor.

At the same time, the completion of my works is closely related to the support of my group mates including Dr. Xiaodong ZHENG, Dr. Haiyan JIN, Dr. Wei HAN, Dr. Dengrong SUN, Mr. Lok Wing Wong, Mr. Ka Hei Lai, Mr. Shan JIANG, Mr. Hok Yin WONG, Mr. Zhangyuan YAN and Mr. Chi Shing TSANG. They have given me invaluable help and guidance. I also want to thank Dr. Thuc Hue LY and her group members from the City University of Hong Kong, as a close cooperation team which provides me useful advice and kind assistance during my research study.

Last but not least, I want to show my special appreciation to my dear parents for their endless love and care throughout my Ph.D. study. I would like to thank my best friend Howard for his spiritual support and understanding. I also appreciate all my great friends in Hong Kong, I will always cherish those sweet memories and good times we had together.

TABLE OF CONTENTS

LIST OF FIGURES

LIST OF TABLES

Chapter 1 Introduction

1.1 Introduction on 2D Materials

1.1.1 The Structure of 2D Materials

Two-dimensional (2D) materials is the definition of materials consisting of a single layer or few layers of atoms or molecules. These atoms are combined by strong covalent or ionic bonds within the layers and weak van der Waals forces between the layers. They have unique characteristics and functions due to their distinct 2D structures. At present, 2D photoelectric materials mainly include graphene (GN)[1], topological insulators (TI)[2], transition metal chalcoides (TMDs)[3], black phosphorus (BP)[4], and so on, as shown in Figure 1.1. In 2004,

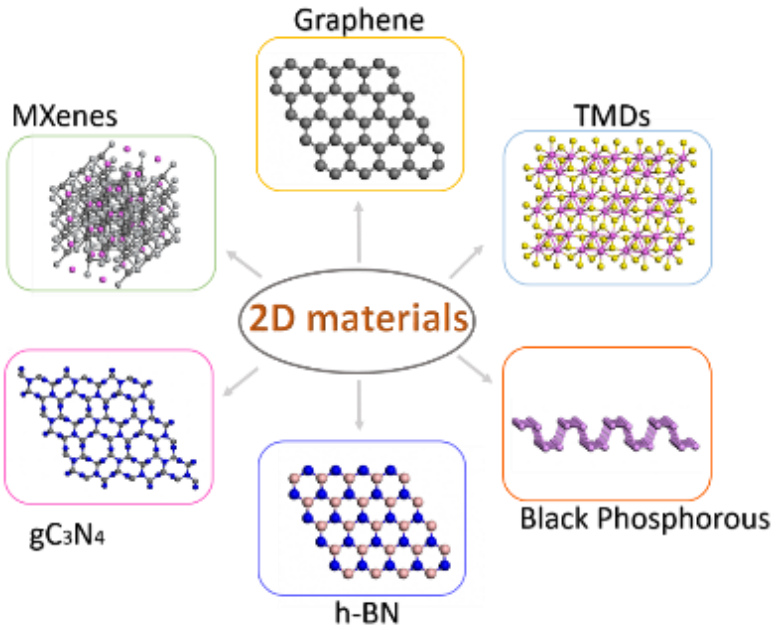

Figure 1.1 The family of 2D materials.

Geim and Novoselov's group obtained graphene by adhesive tape stripping method and studied its related physical properties, which triggered a worldwide research boom on 2D materials.[1]

Graphene, as the first 2D material being discovered, is composed of a hexagonal lattice of monolayer carbon atoms with sp2 hybrid orbitals and packed tightly into a honeycomb structure. With the ultrathin thickness of 0.335 nm, graphene is the thinnest and strongest material known in the world. For the electronic properties, electrons travel very fast in graphene, at about 1/300 of the speed of light, much faster than they would travel in a normal conductor.[5] At the same time, its resistivity is only 10^{-6} Ω·cm, making it the material with the lowest resistivity and best electrical conductivity ever found. For the electronic structure of graphene, the carbon atoms constitute the unit benzene ring form sp2 hybridization through the electrons of the s, px and py orbitals. Two adjacent carbon atoms form a σ bond through the hybrid orbital to form a huge and stable graphene sheet. The remaining pz orbitals of each carbon atom couple with each other to form a so-called large π bond. Due to the strong interaction between the hybrid orbitals from two adjacent carbon atoms, the energy gap between the σ bond and the anti-σ bond (σ*) is very large, so that the energy band formed by σ-bonded electrons and the energy band formed by σ*-bonded electrons are far away from the Fermi energy surface. The weak mutual coupling between the pz orbitals makes the energy split between the π bond and the anti-π bond very small, causing the energy of the π electron to approach the Fermi surface, which becomes the main factor in the electronic properties of graphene.

Another typical family of 2D materials is transition metal dichalcogenides (TMDs) which are semiconductor materials with thin atomic layers. The generalized chemical formula of TMDs material is MX_2, where M presents a transition metal of group 4 to 10 in periodic table of elements and X presents a chalcogen. It includes three layers of atoms which is X, M, and X, respectively. The interatomic bonds between M and X atoms are mainly constituted by van der Waals forces and they are combined by covalent basal plane bonds. For the structure of bulk TMDs, a prominent property is that they have high degree of symmetry in crystal structure. But different from these bulk materials, in TMDs monolayers (as well as other odd layers), there is neither inversion symmetry nor an inversion center. If M belongs to groups of VIB transition metals, MX_2 are semiconductors. On the other side, if M belongs to groups of VB transition metals, MX_2 are metals. Therefore, for further applications, 2D TMDs overcome disadvantages of graphene in many aspects such as electronic, photonic and optoelectronic related fields. The main reason is that graphene does not have a bandgap as a semimetal while the bandgap of some TMDs can increase from indirect to direct when the thickness decreases from bulk to single layer (e.g. bulk MoS_2 has an indirect bandgap of 1.2eV and monolayer MoS_2 has a direct gap of 1.8eV).[6]

1.1.2 Defects in 2D Materials

In an ideal pristine crystal, the atoms are strictly arranged in a regular, periodic lattice in a certain order. However, in the actual crystal, the arrangement of atoms normally has defects during the growth of crystals, such as the thermal fluctuation of atoms and other conditions. According to the geometric characteristics, crystal defects in bulk materials can be divided into

the following three categories in general: point defects, also known as zero-dimensional defects, such as vacancies, interstitials, and doping atoms. Line defects, which are one-dimensional defects commonly seen from the fundamental of edge, screw and mixed dislocations. The third type is planar defects, including grain boundaries, phase boundaries and stacking faults. When the dimension of materials decreases from bulk to 2D, some typical planar defects like grain boundaries and stacking faults should be classified as one-dimensional defects while folding, wrinkling are regarded as two-dimensional defects.[7] Figure 1.2 shows the structure of possible defects on 2D materials.

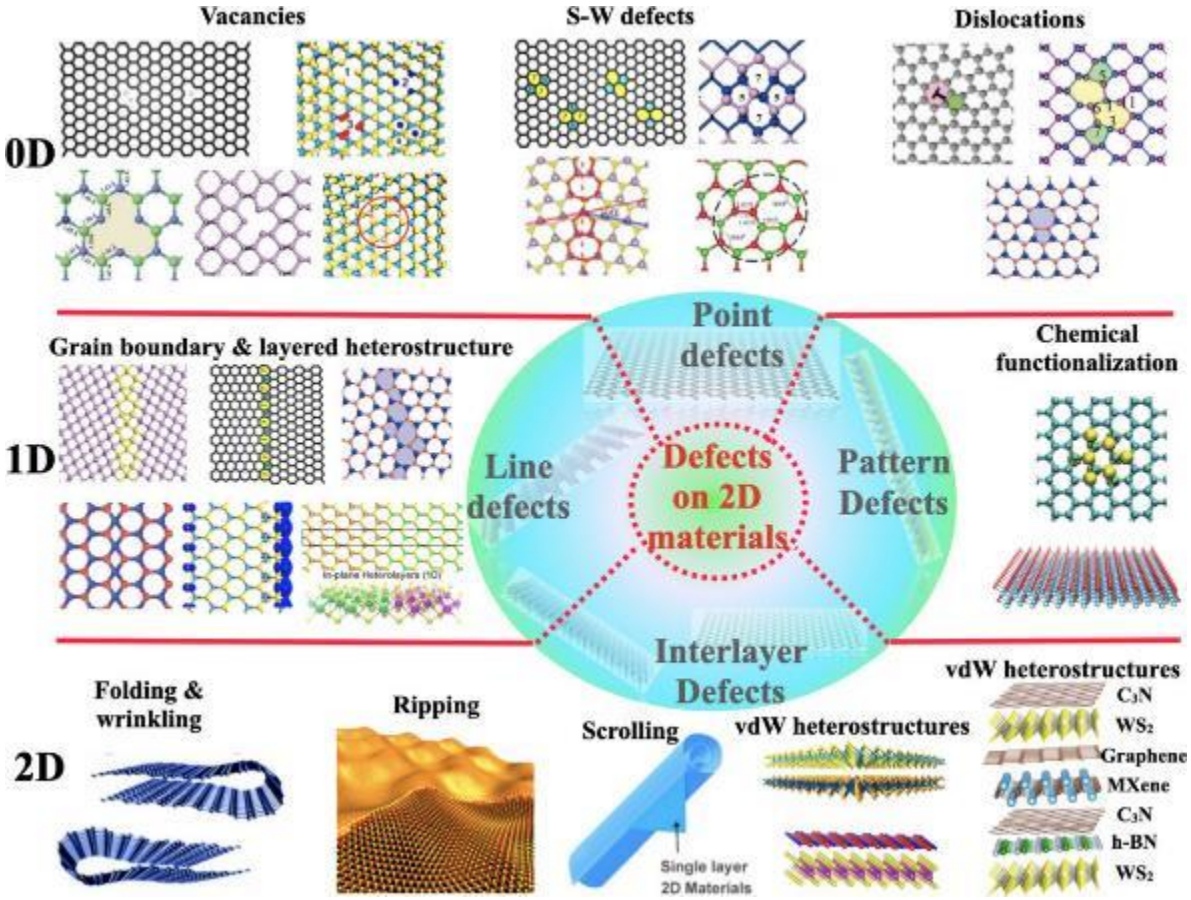

Figure 1.2 The family of defects in 2D materials.[7]

Vacancy is the simplest defect which occurs with the vanishing of atoms. For example, in MoS_2, V_s shows mono sulfur vacancy which has the lowest formation energy; V_{s2} means disulfur vacancy; V_{MoS3} stands for vacancy complex of Mo and nearby three sulfurs which have similar formation energy for S vacancies, and so on.[8] Using first principle calculation to measure the formation energies and thermodynamical charge transition in monolayer MoS_2, in Mo-rich conditions, S vacancies are the most abundant defects among all growth conditions. On the other hand, in S-rich conditions, formation energies are quite high for good-quality crystal growth.[9] Meanwhile, sometimes the lattice atoms may be replaced by other atoms which is called doping. In most doping conditions, the atoms of M or X in MX_2 are replaced by substituting atoms which come from the similar size of ions, electronegativity, valence, and also other member crystal. From previous study, Mn, Nb, Fe, Re, Au, and Co are all potential dopants for the transition metal atoms,[10] while chalcogen site doping may be favorable in sulfur deficient crystals. Except for dopants, atoms can also play the role as adatoms in TMDs monolayers. In this situation, the position of the foreign atoms decides the defects. It can exist either above the metal atoms, or above the chalcogen atoms, or on a metal–chalcogen bond, and above or within the center of hexagonal voids.

Line defects always have a prominent influence on the properties of materials. One of the most common line defects, grain boundaries (GBs), are usually not perfectly straight and are linked with various GB kinks that can have important influences on the material properties.[11] As reported in previous studies, not only traditional GBs but also bilayer overlapped junctions have been observed in chemical vapor deposition(CVD)-grown monolayer materials. An atomically stitched GB can be initially formed between the merged monolayer grains and

provides abundant structural defects for nucleation.[12] The parameter which is largely influenced by GBs is the bandgap, and it is the reason that some optical and electronic properties change with the appearance of GBs. Since the thickness of 2D TMDs is ultrathin, they can own a broad range of semiconducting bandgaps with different compounds.

Another type of defects here we define as three-dimensional defects exit specifically in 2D materials includes folding, wrinkling, scrolling, rippling, and stacking faults. The most common 3D defects of TMDs monolayer is folding or wrinkling. It is well known single layer TMDs have good flexibility which is easy to fold. The tensile stress and strain on the edge of the curve are key parameters in calculating the dynamical properties in folding. Previous research tried to reconstruct 3D folded structures for different kinds of membranes to fit the continuum mechanics model.[13] If the armchair fold is collapsed, AB stacking can be formed. The curvature on the edge reflects the in-plane tensile/compressive strain applied on the material. For ripples on 2D materials, in MoS_2 they have a space-dependent surface potential and charge distribution which are originated from the local tensile strain due to the mismatched lattice constant with that of substrate. On the other side, the surface potential is relatively uniform in 2D MoS_2 nanostructures without ripples.[14] The difference of ripples results from the existing local strain during the process of synthesis. For the study of various kinds of defects in TMDs monolayers, the alignment of atoms and related mechanical parameters such as stress and strain play important roles. Using patterning from AFM, TEM (HRTEM), mapping and modeling can illustrate the relationship of these factors clearly.

1.1.3 Applications of 2D Materials

Two-dimensional(2D) materials hold a wide range of applications in many fields such as energy storage, electronic devices, biological and photonic devices. Figure 1.3 shows the fields where 2D TMDs has good performances at.[15] At the same time, the defects mentioned above from 0D to 3D have prominent influences on 2D materials, sometimes can change the

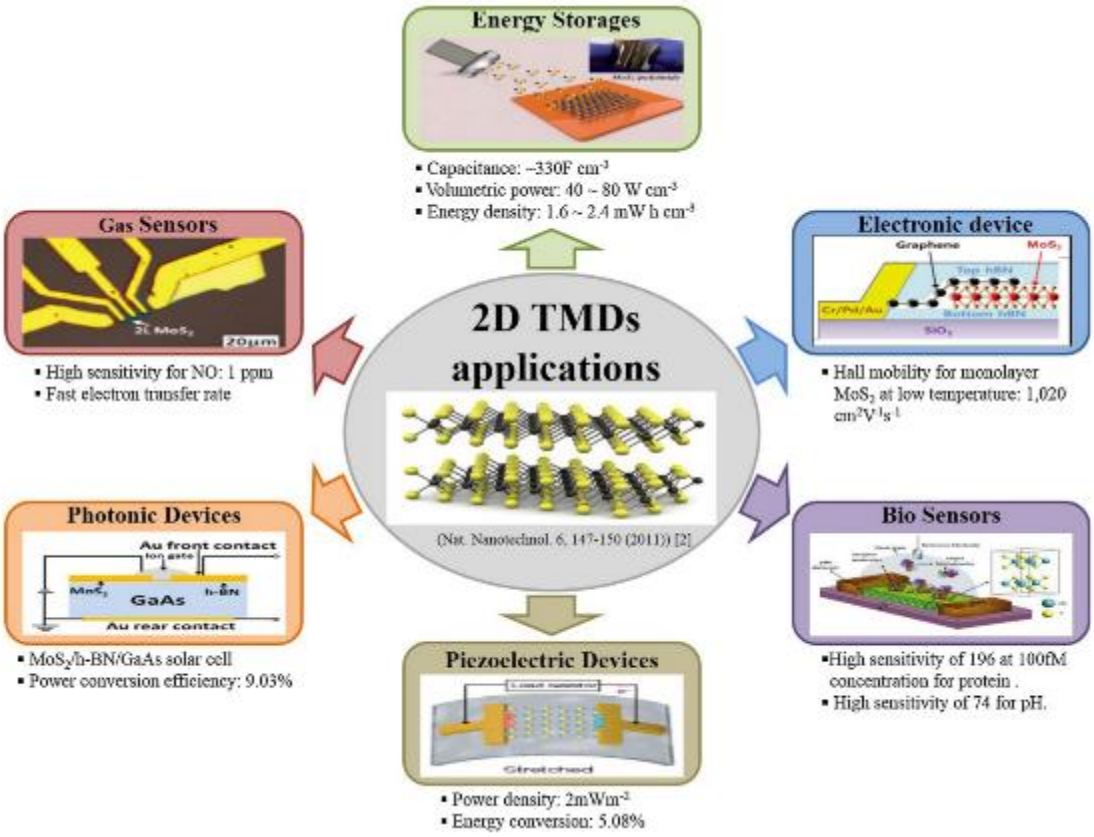

Figure 1.3 The application of 2D TMDs in devices.[15]

properties of pristine materials to a great extent. The bandgap of 2D TMDs decides the electronic and optical properties of materials, especially on semiconductors. It can be controlled by doping [16], strain [17] and defect engineering.[18] The band structure is significantly influenced by GBs, and it is the reason that some optical and electronic properties

change abruptly with occurrences of GBs. Apart from that, 2D TMDs own exotic properties which include indirect to direct bandgap crossover as the number of atomic layer decreases.

The lateral and vertical heterostructures made of 2D TMDs also have been realized and their novel electrical/optical properties especially at the sharp interfaces have been experimentally verified. For synthesis of lateral heterostructures, they can be created mainly via CVD growth,[19] while vertical heterostructures have been demonstrated via both CVD or mechanical exfoliation.[20] It has been reported in vertical heterostructures the interaction of interlayers tuned from no coupling to strong coupling.[21] The top layer of MoS_2 and bottom layer of WS_2 are aligned in one area while the MoS_2 turns into bottom and WS_2 becomes top layer in the other area to conduct the test.[22] The result implies that the change of optical properties comes from the different lattice distance in heterostructures and pristine materials.

In mechanical aspect, the physical properties of 2D materials vary a lot depending on the bending/rippling structures, and the mechanical bending/rippling/buckling of 2D materials are key factors in the emergent applications such as active materials for wearable devices,[23] diffusive membranes for energy devices,[24] or nanoelectromechanical (NEMS) devices.[25] For 2D materials, the strain energy is embodied in the ultrathin area, which directly reflects the stress and elastic modulus. In some cases in monolayer membrane, the sample across a hole and strain is applied at the central part by a tiny tip, the bending modulus is small enough to ignore. The load is balanced by the pretension of the membrane and scales linearly with vertical deflection under small loads.[26] When the load is large, it is dominated by the stiffness of the

membrane with a cubic relationship. The elastic modulus of MoS_2 is similar with many other TMDs material, which is about half of the value in the strongest 2D material, graphene.

1.2 Mechanical Behaviors of 2D Materials

The mechanical behaviors have been well noticed in various materials on both bulk and 2D cases since they are closely related to the defects in materials. When a mechanical loading is applied, all the defects as mentioned above can be generated. 0D defects (vacancies mainly) can aggregate 1D defects, such as GBs. Some 2D defects also consist of vacancies, for example, the vacancies can cause phase transitions on 2D materials and normally make a great change on the electronic properties. Slightly different from the literature above,[7] in our work, we define folding, wrinkling and out of plane wrapping as 3D defects. The geometry of these defects are in 3D space even they are formed by 2D layers.

1.2.1 One-Dimensional Dynamic Process: Grain Boundary Mobility

The structures and novel properties of emergent 2D materials have been unveiled over the last decade.[27] From the high-symmetric graphene,[28,29] to the low-symmetric black phosphorous (BP),[30,31] numerous 2D van der Waals (vdW) layered materials with atomic thickness have been discovered.[32-35] Very recently, monoclinic 2D materials such as rhenium disulfide (ReS_2) and rhenium diselenide ($ReSe_2$) with the ever lowest symmetry in 2D have been fabricated and drawn much attentions for their outstanding anisotropic properties.[36,37] On the other hand, it

has been shown that the grain boundaries (GBs) prevalently existed in many 2D materials especially when they are synthesized by chemical vapor deposition (CVD) growth.[38]

The remarkable electrical[39] and mechanical effects[40] from these GBs on 2D materials have been highlighted. Figure 1.4 shows the change of electronic structure of WS_2 with grain boundaries. Grain boundaries are usually caused by different types of dislocations and defects. From the experiment in Figure 1.4,[39] grain boundaries result from 6|8 dislocation brings localized in-gap states on the band gap of WS_2, which can be sinks of charge carriers and it influences the electronic transport in monolayer WS_2. The results also show the 5|7 dislocation makes a different change of the band gap on materials from this work. Another previous study tested the strain-stress under the influence of different grain boundaries in h-BN, as shown in Figure 1.5.[40] The two sides of grains can be defined by the domain directions, some of them are symmetric on two side and some are asymmetric. The strain-stress curves show that all of the fractures are brittle but the critical failure strain can be different from 11% to 21%. Regarding the atomic structures, the GBs in high-symmetric 2D materials, such as graphene and molybdenum disulfide (MoS_2) have been well documented.[28,41] It illustrates GBs in high symmetry 2D materials consist of in-plane dislocations or atomic defects, therefore, a

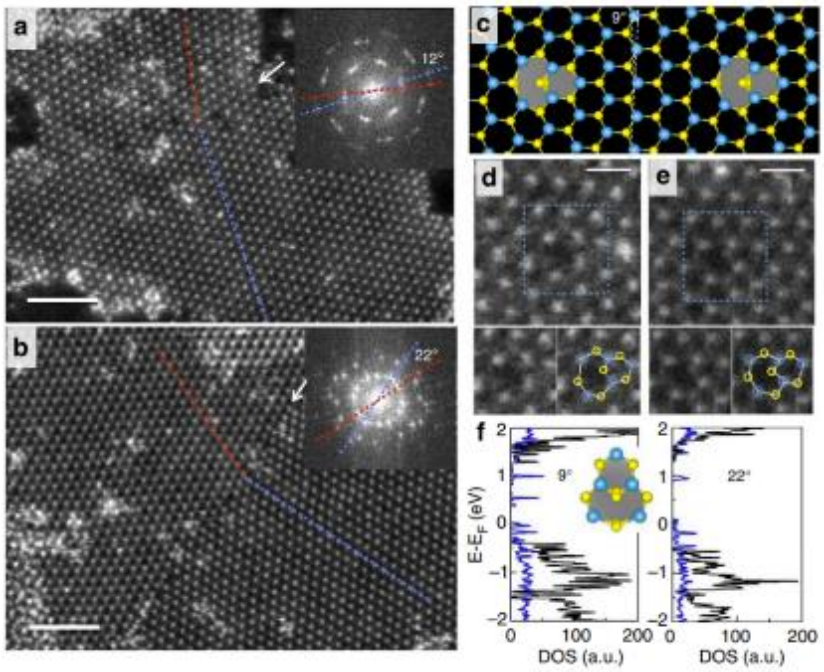

Figure 1.4 Atomic structure and electronic properties of WS_2 with grain boundaries. (a, b) HAADF images of WS_2 with different angles of grain boundaries. Scale bar=2nm. (c) Atomic model of the dislocations. (d, e) HAADF images of two different types of dislocations. Scale bar=0.5nm. (f) Total electronic density of states for the 9° and 22° grain boundaries composed of 6|8 structures.[39]

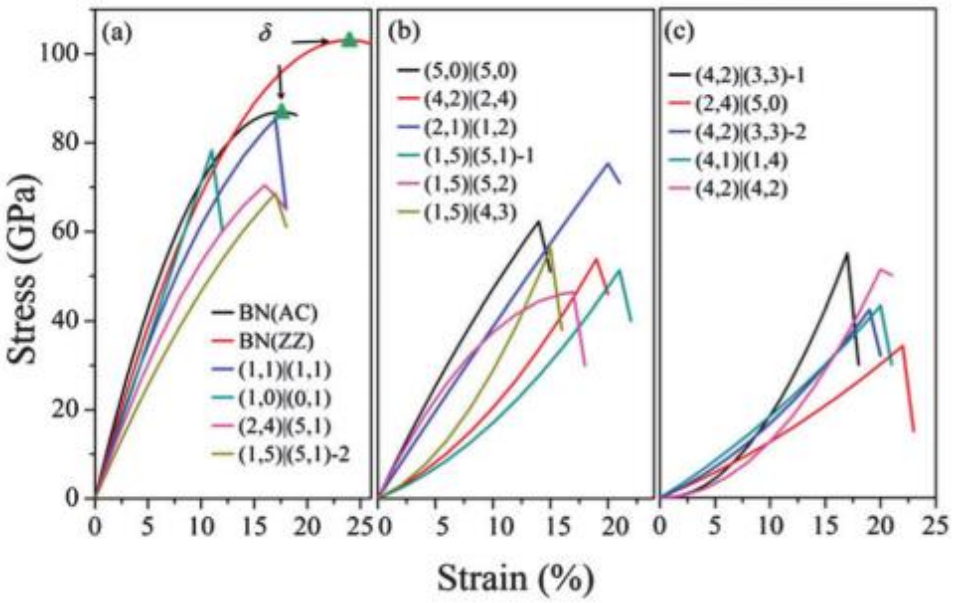

Figure 1.5 Stress–strain curves of GBs on the h-BN surface and a pristine h-BN along its armchair and zigzag directions.[40]

relatively high energy barrier is requested to trigger the GB movement. [42,43] Herein, through the high resolution atomic-scale transmission electron microscopy (TEM) characterizations and atomistic density functional theory (DFT) simulations, the GBs in 2D materials with lowest symmetry--the monoclinic 2D ReS_2, is considered as an ideal sample. Apparently, the GB types are greatly enriched by the asymmetric structure, in particular the twinning boundaries (TB). Meanwhile, the distinct GB kinetics is also unusual and endows larger mechanical deformability to 2D ReS_2.

For the GB types, in graphene GBs can be classified into low-angle (LA) twinning GBs made of piled-up (Stone-Wales) dislocations and high angle (HA) irregular GBs.[44] These two are defined by the angle of the lattice orientations on the two sides of GBs and they are commonly observed in bulk and nanomaterials. Both of them can move under shear stress and the velocity by climb has a linear relationship under the external shear stress. From Figure 1.6 it is not difficult to find the velocity of HA irregular GBs is higher than that in LA GBs under the same

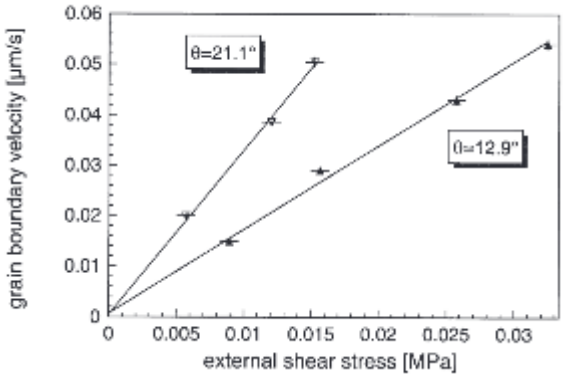

Figure 1.6 Grain boundary velocity on the external shear stress for two <112>-tilt boundaries in LA and HA GB cases.[44]

external shear stress.[44] In 2D monolayer (1L) MoS_2 or other similar hexagonal phase TMDs, except for the LA twin GBs and HA GBs above, the break of inversion symmetry additionally introduces the 180° mirror GBs (or inversion GB).[45,46] They are observed in MoS_2 for the first time and can be easily distinguished by the orientation of Mo and S in a hexagonal lattice structure like shown in Figure 1.7. It is easy to tell that the two orientations have different contrasts under dark-field (DF) mode of TEM.

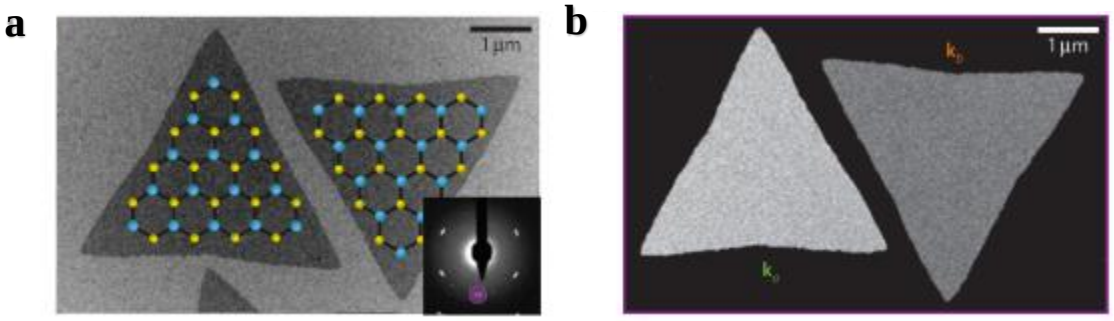

Figure 1.7 TEM images of two different 180° mirror symmetric orientations of MoS2. (a) Bright-field TEM image of two triangles with S-zigzag edge orientations. (b) Dark-field TEM image of the two flakes.[45]

Moreover, all the GBs in 2D MoS_2 can be sub-divided into two categories ('up' and 'down') due to the lack of inversion symmetry. Different dislocation core structures belonging to two respective categories have been observed by us.[47] Figure 1.8 gives a systematic summary on the types of GBs in MoS_2, apart from common HA and LA GBs in bulk materials, GBs can be divided by whether the two side are coherent or not. The mirror boundary with a rotation of 60° was also captured by STEM. It worth noticing in 2D materials GBs can be clearly observed and distinguished as long as their atomic images are obtained. Generally, all these GBs observed in 2D materials are formed during the sample growth stages for dynamical reasons,[48]

specifically, by the stitching of single-crystalline flakes grown from different nuclei.[49] Apart from growth, defects created by electron irradiation and annealing can also generate new GBs within the pristine single-crystalline graphene.[50, 51] However, the generation, movement

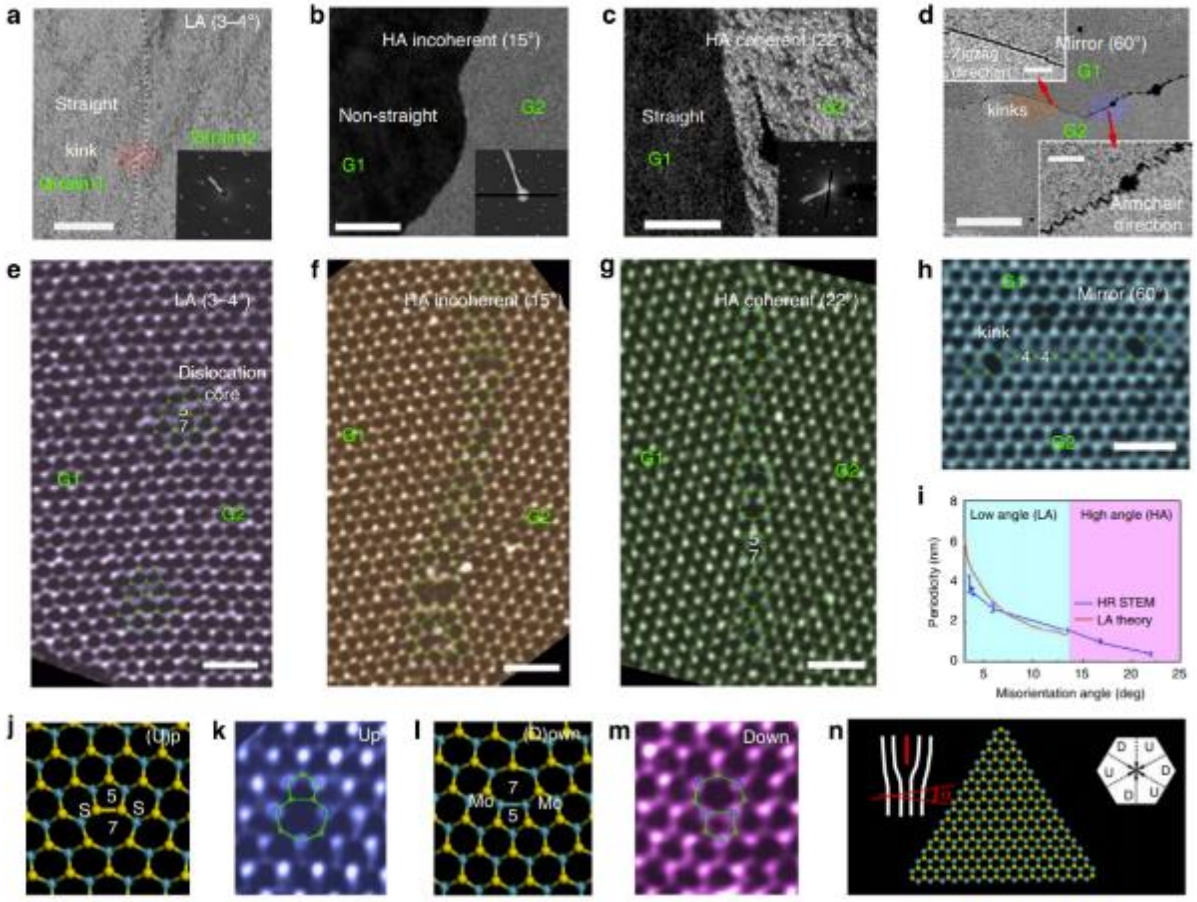

Figure 1.8 TEM characterization of the MoS_2 GBs showing misorientation angle dependence.[47]

and annihilation of dislocations usually require high energies in most of the defect-less 2D materials. Besides, owning to the high energy of in-plane stacking fault (SF), the mechanical twinning process[52] is normally not allowed in high-symmetric 2D materials. As a result, the

presence of GBs and lack of dislocation/twinning dynamics in 2D materials lead to poor ductility in polycrystalline 2D materials.[53]

1.2.2 Two-Dimensional Dynamic Process: Phase Transition

Originated from symmetry breaking, 2D structures are vulnerable to Peierls instability[54] which causes charge density wave (CDW)[55] phenomena. TMDs with predominant van der Waals (vdW) layered structures and weak interlayer interactions, indeed favor the formation of various CDW phases.[56,57] As result of electron-photon coupling, there are strong deviations from Fermi liquid theory in CDW phases (Figure 1.9). Among TMDs, ReS_2, which contains d^3 ions[58] and Fermi surface nesting along two directions (*a*, *b*), follows the diamond chain

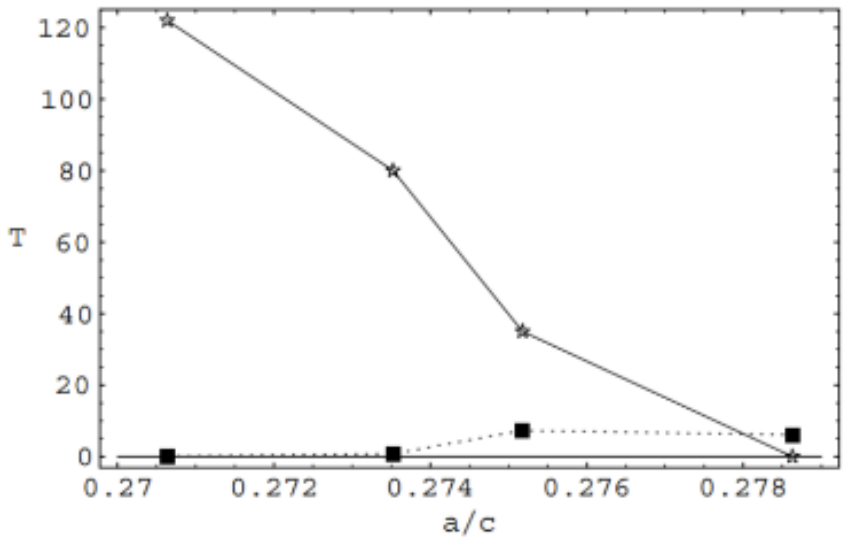

Figure 1.9 Phase diagram of $TaSe_2$, TaS_2, $NbSe_2$, and NbS_2 from left to right, stars stand for T_{CDW} and filled squares stand for Tc.[56]

clustering of Re ions (*viz.* T″ phase, space group: P-1).[59] A remarkable bandgap arising from the dimerization clustering of Re ions endows ReS_2 very attractive electronic and optical properties, particularly in its 2D form, the monolayer (1L) ReS_2.[60] Figure 1.10 shows the DFT calculation of the band structure of the most stable phase T″ in ReS_2. No matter it is bulk or monolayer, they both have direct bandgap and are semi-conductors. Thus, the thickness of ReS_2 does not influence the property of conductivity, which is very different from conventional TMDs such as MoS_2, WS_2 and WSe_2.

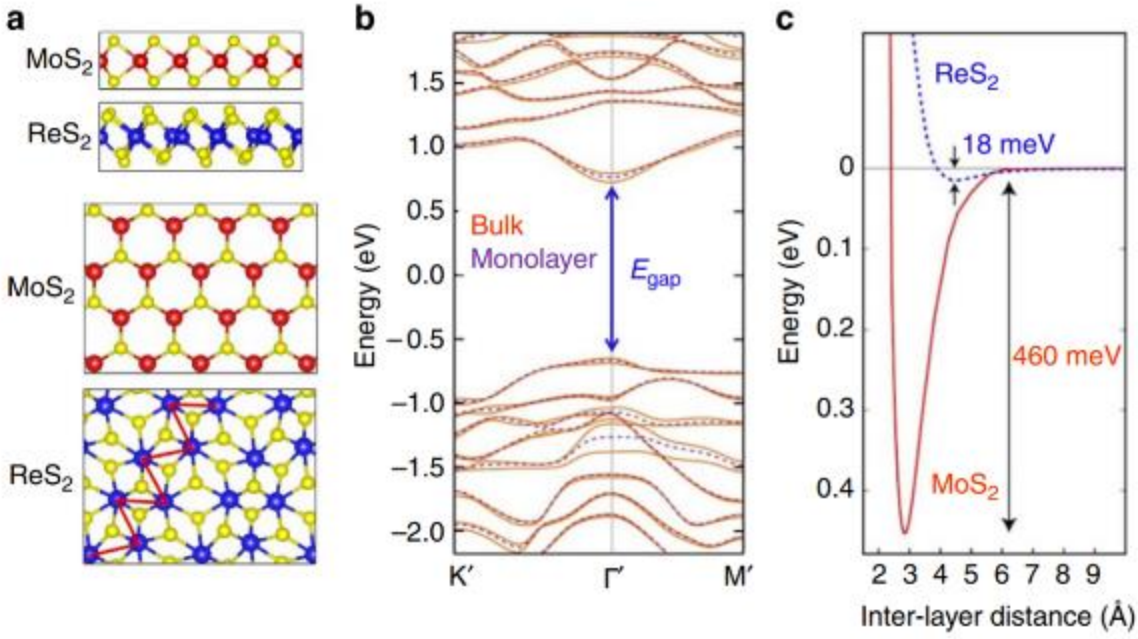

Figure 1.10 Different crystal structure and band structure of ReS_2 from conventional TMDs. (a) Side and Top view of MoS_2 and ReS_2. (b) DFT calculated electronic band structure of bulk (orange solid curves) and monolayer (purple dashed curves) ReS_2. (c) The calculated total energy of the system as a function of interlayer separation.[60]

Conventional phase engineering methods include straining,[62] temperature,[63,64] laser[65,66] or electronic/chemical doping.[67,68] Figure 1.11 shows the 3 steps of phase transition in TMDs materials on an expanding substrate.[69] In the first step, only 2H phase deforms elastically and

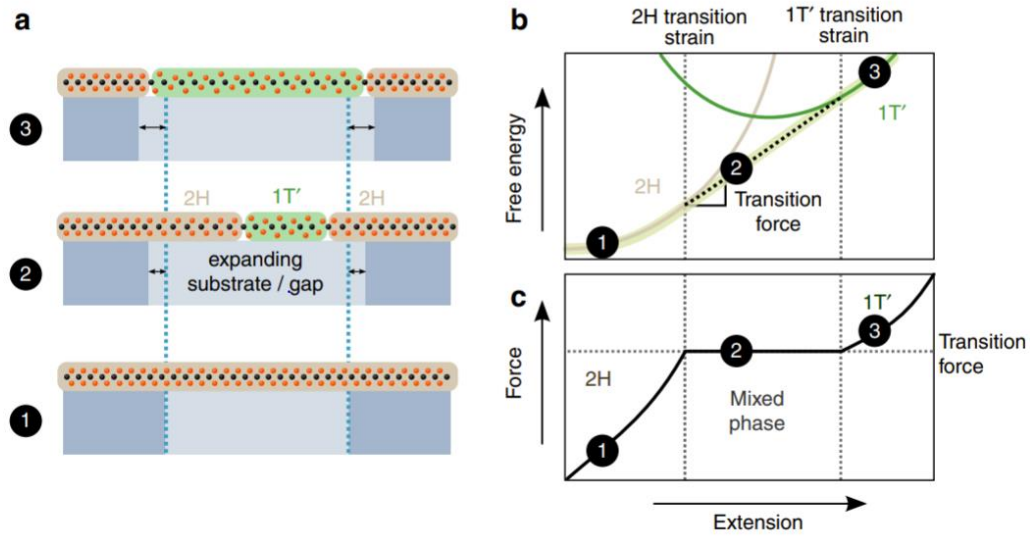

Figure 1.11 Phase coexistence under an applied force or extension. (a) A schematic diagram of tensile mechanical deformation showing 3 steps of phase transition of TMDs on substrates. (b) The relationship of 2H/1T'' Helmholtz free energy landscape and extension. (c) The relationship of force and extension.[69]

there is no phase transition observed. In step 2, between 2H and 1T′ energy surfaces, there is a common tangent of lowest free-energy path. Afterwards the lowest energy phase turns in T′ phase as the completion of phase transition. However, for the most popular 2H TMDs, MoS_2, early studies show large equibiaxial deformations but no phase transition in experiment, which is because of the high T′-H energy difference in MoS_2.[69] Another study presents the direct observation of coexistence of two phases on MoS_2 by doping.[70] The modeling of atomic

structure, TEM characterization and elemental mapping are exhibited in Figure 1.12. A carbon-doping induced phase transition method is used to obtain MoS_2 with both stable T and H phases. Apart from all these methods mentioned above, vacancy-triggered straining technique serves as the most precise one, enabling the scalable "atomic lithography" for future devices.[71] STM techniques is applied to improve the hydrogen lithography on atomic silicon. In practice, on a substrate of 10 × 10 nm^2, the patterns can be written by changing the voltage of electron and the height of STM tips.[71] Meanwhile, under the help of hydrogen repassivation technique, the errors can be erased. Lithography in atomic scale is well controlled in this case (Figure 1.13).

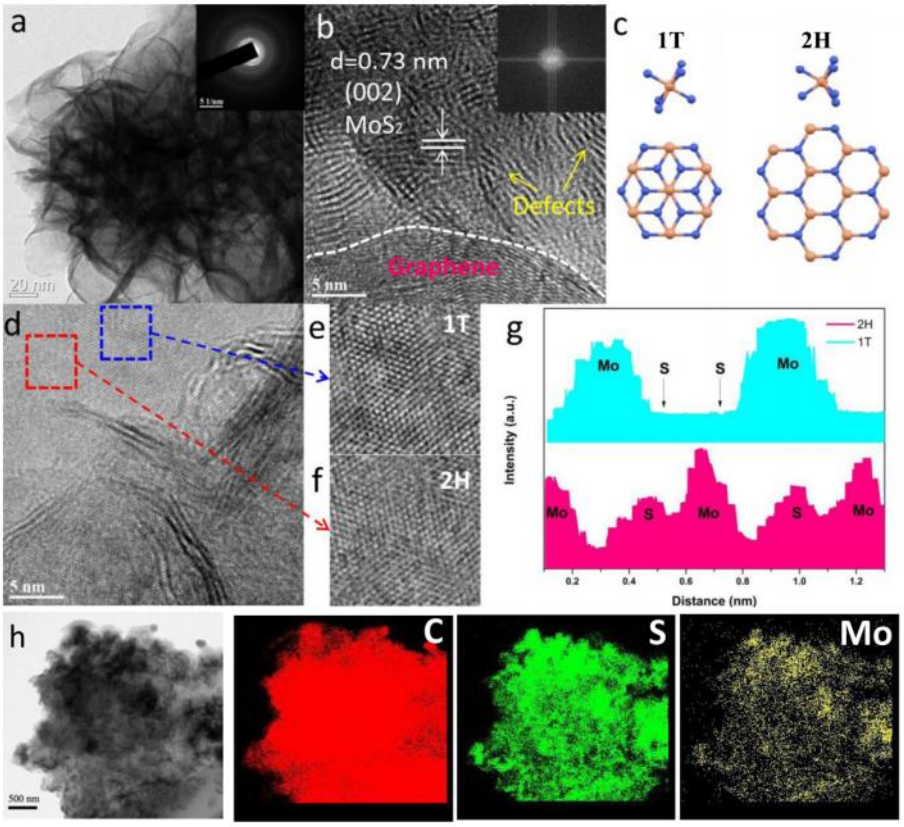

Figure 1.12 Phase transition of MoS_2 under doping. (a, b) TEM image of C+MoS_2 @GR-10W. (c) Atomic structure of different phases. (e, f) HRTEM image of different areas in (d). (g) intensity profiles down the lines. (h) EDS elemental mapping of the sample.[70]

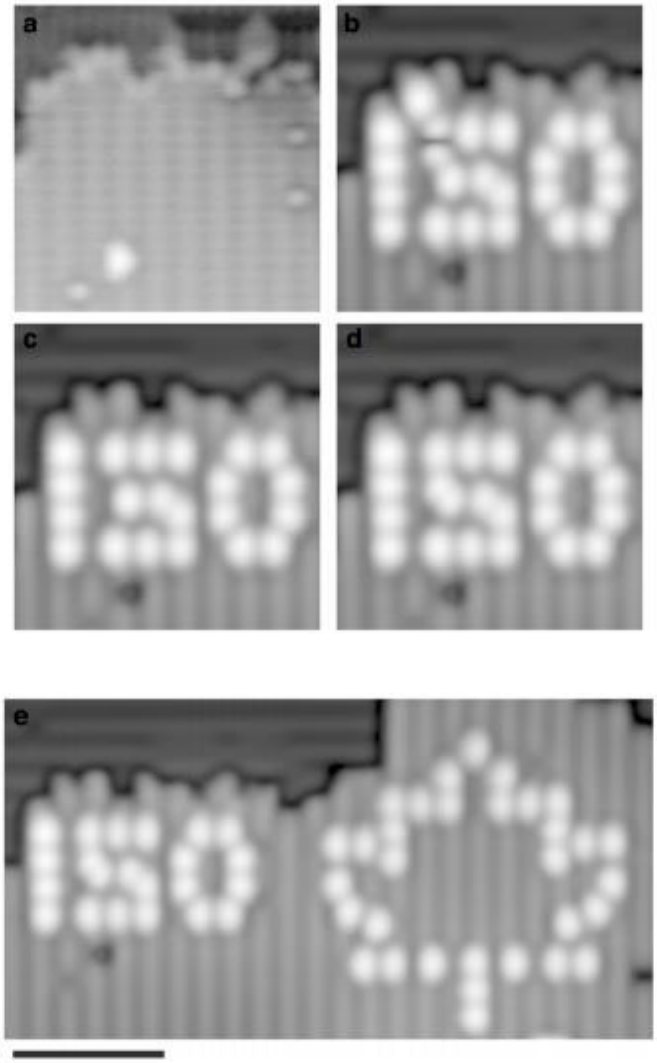

Figure 1.13 The fabrication and correction of lithography on a silicon substrate under (a) 1.4V, (b)-1.7V, (c,d) errors being erased using hydrogen repassivation technique. (e) the lithography in a larger substrate. Scale bar = 5nm.[71]

Phase engineering in materials have been extensively employed to modulate the electrical, mechanical, optical and other functional properties.[72-75] In emergent 2D materials,[76] phase engineering is also highly attractive owing to the inherent polymorphism in the low

dimension.[77] For instance, hexagonal (H) and tetragonal (T/T′/T_d) phases[78] in 2D TMDs provide excellent platform for phase transition applications, e.g., memory[79] and neuromorphic devices.[80] Metallic T or T′ phases in 2D MoS_2 and $MoTe_2$ have been used in high quality heterojunctions[81] or Ohmic electrical contacts.[82] The contact resistance of 1T and 2H phases is tested as two types of devices in Figure 1.14. The results show the 1T phase is metallic

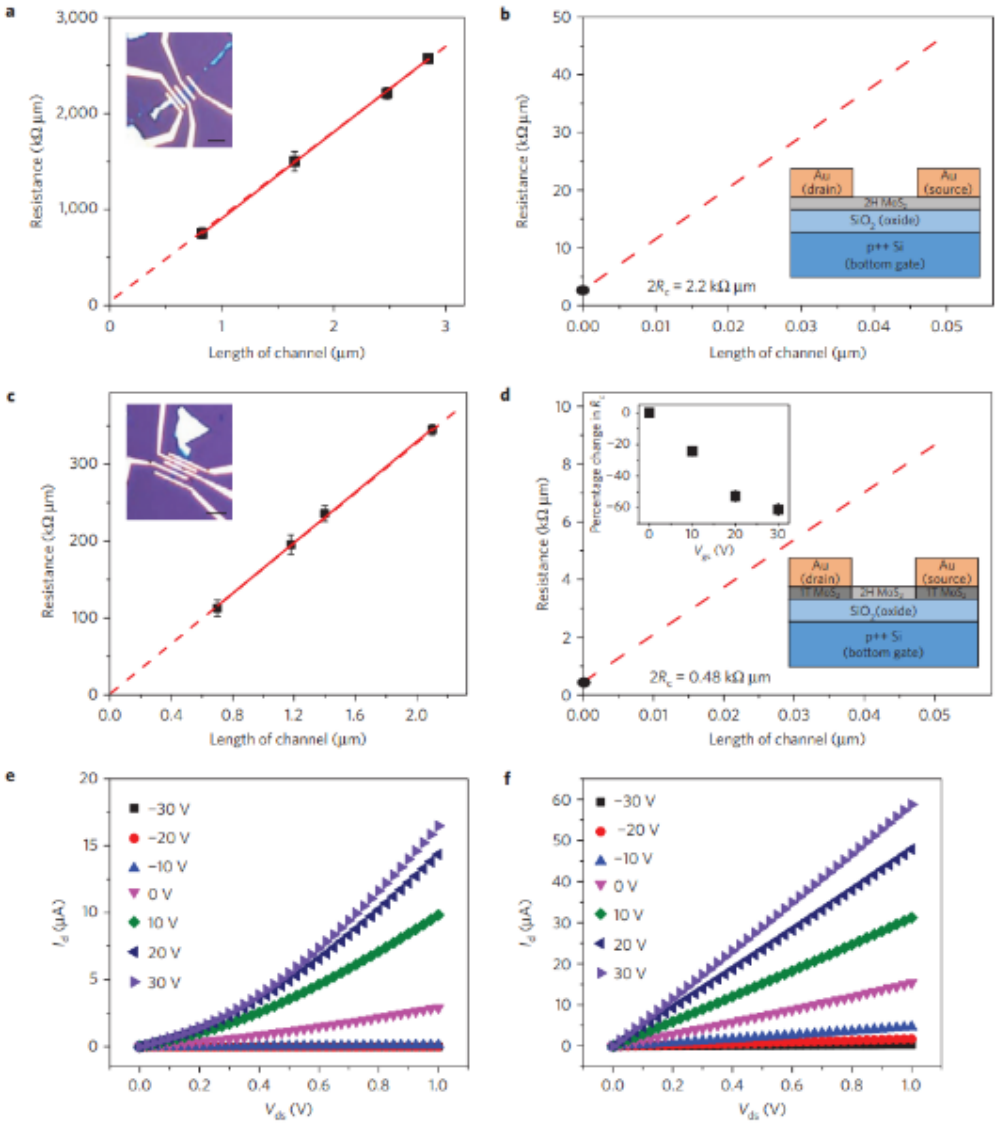

Figure 1.14 Test of contact resistance of 1T and 2H phases. (a-d) Resistance versus 2H channel lengths for Au deposited directly on the 2H phase, (e, f) Drain current characteristics of back-

gated FETs for 0-1 V drain-source voltages and gate–source voltages ranging from −30 V to 30 V.[81]

which can be locally induced on semiconducting 2H phase. Comparing with 2H phase, 1T has much lower resistance values. At the same time, from Figure 1.14e, f, the relationship of drain current and drain-source voltage shows Schottky behaviour for gold directly onto the 2H phase and linear behaviour for the 1T electrodes.[81] The atomic mechanism of H-T phase transition in 2D MoS_2 has been unveiled by ADF-STEM, the exotic Re dopants were found critical for T phase nucleation.[83] Contrary to the extensively investigated H-T phase transition,[69,70,84] the transition between metallic T phase and their CDW phases with zigzag, ribbon or

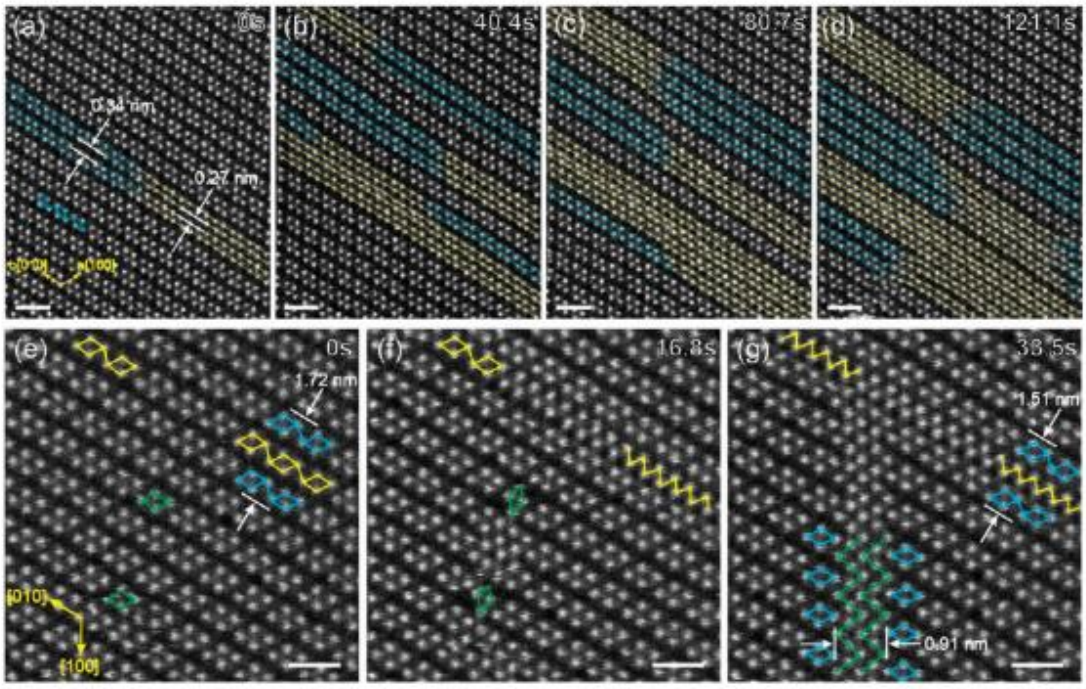

Figure 1.15 (a-d) A series of HAADF images on the distortion of lattice space when the monolayer ReS_2 is exposed under STEM. (e-g) A series of HAADF images on the zipped triple diamond chains when the monolayer ReS_2 is exposed under STEM.[85]

diamond shape clustering of metal ions is less understood. The T″ phase of ReS_2 was observed to zip up under electron beam.[85] As shown in Figure 1.15, the energy from electron beam causes S defects, therefore there is distortion in the lattice and the lattice distance expands or shrinks in different areas in the series of lower magnification. In the figures under higher magnification, the motion of Re atoms forms new lattice chain which has an angle of about 60° with domain lattice direction (Figure 1.15g). The atomic structure in these area turns to be different from pristine distorted T phase and becomes more symmetric. However, the process and mechanism behind phase transition has not been explained in details in pervious works. Nonetheless, the lack of stability of T or T′ phases should be attributed to the strong tendency of Peierls instability.[54,86]

1.2.3 Two-Dimensional Dynamic Process: Fracture and Crack Extension

Fracture of materials can be classified into two main types: brittle and plastic [87]. Plasticity is associated with deformation, including dislocation, twining, amorphorization, etc., which is initiated in the stress-focused crack tip zone when the local stress level exceeds the thresholds.[88] The formation, propagation and structure of cracks determine the failure mechanics of engineered materials. Despite decades of study,[89-91] however, atomic resolution imaging of crack tip and its propagation have remained elusive. [92] This has led to notable discrepancies between theoretical models and experiments, especially in nanoscale it is difficult to capture the fracture process as the comparison with theoretical results.[93-99] For modeling, MD simulation can provide the break and extension of cracks in different 2D

materials in atomic scale.[99, 100] As the result, simulation of the cracking process has been modelled in atomic scale, describing how the bond break and rotation of atoms based on Griffith load. (Figure 1.16a, b) After the crack-tip bond breaking, there is a bond rotation on the symmetric two sides with defects on each side (Figure 1.16c). Figure 1.16d-f illustrates the rotation of bonds separates the pentagon and heptagon, which can lead to symmetric and asymmetric cleavage fracture in cracking. While some controlled (referred to as stopped) cracks have been imaged in TEM.[100,101] The chaotic and unexpected atomistic fracture mechanism[102-104] has revealed the strain fields in propagating cracks, in connection with the classical fracture theories.[105,106] The fundamental limitation in designing fracture resistant materials using elastic stress analysis is the presence of cracks that increase the local stresses

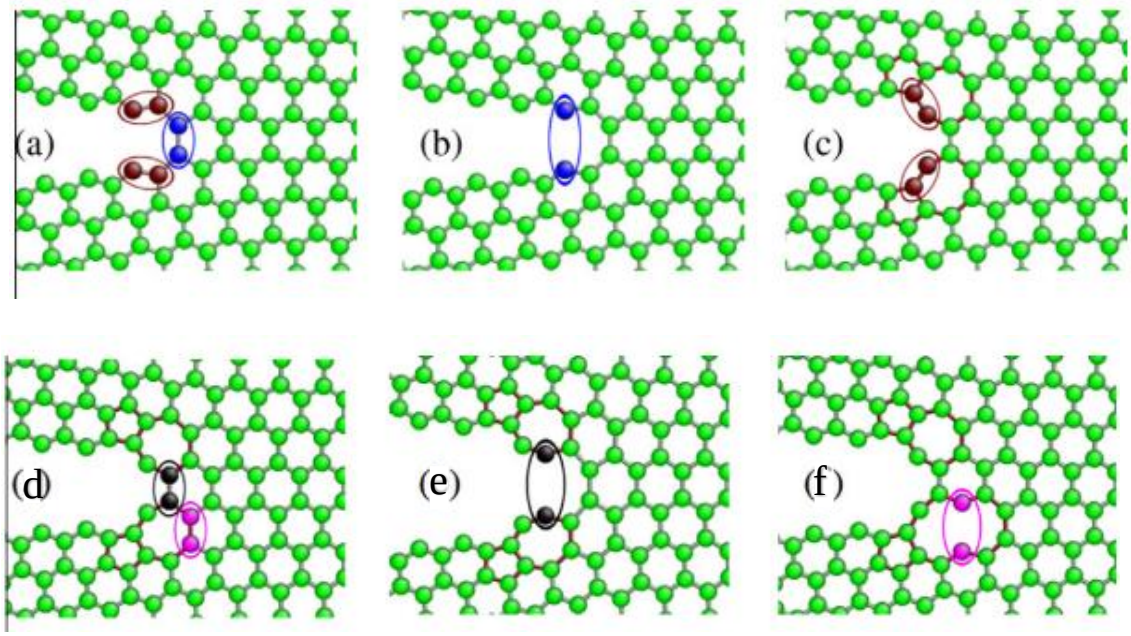

Figure 1.16 Process of crack –tip breaking in graphene. (a, b) Extension of crack by a crack-tip blue bond, (c) 90° rotation of the brown bond, (d) crack after the bond rotation, (e) symmetric and (f) asymmetric atomic structure after the bond broken.[99]

near crack tips--causing real components to fail at much lower stresses than in ideal specimens. Despite their importance, while some fracture tests in nanoscale[107,108] like TEM observations[109,110] on the blunted crack tip zones were reported recently. Figure 1.17. gives clear atomic structure of MoS_2 which is captured during cracking under an aberration-corrected

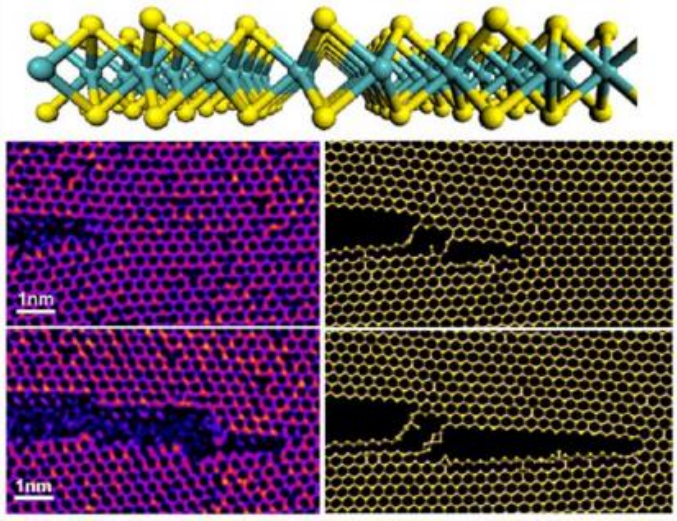

Figure 1.17 AC-TEM images and MD simulation of crack propagation on a monolayer MoS_2.[109]

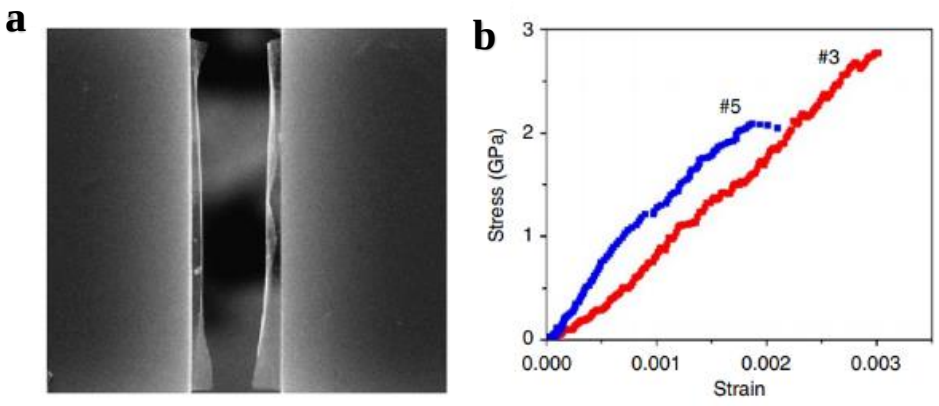

Figure 1.18 (a) The SEM image of graphene membrane after fracture, (b) stress-strain curve of graphene during cracking.[110]

TEM with the corresponding MD model. The process shows one Mo-S bond on the tip is broken and defects are generated, meanwhile the propagation of crack can be clearly observed. On the other hand, the atomic structure of graphene is more difficult to be observed directly. Figure 1.18 shows the nanomechanical test on the fracture of a graphene membrane, observed under scanning electron microscope (SEM).[110] The relationship of strain-stress has been recorded and tested statistically, where the fracture behavior is consistent with the brittle fracture behavior that follows the classic Griffith theory and the toughness has also been calculated. However, the atomic structure of crack tips – whether they are atomically sharp or blunt – in brittle materials remains unresolved.[102,103] While theoretical calculations[106] describe far field stress in front of or behind the crack tips, they are less successful in explaining the divergent stress field near the crack tip because the atomic cohesive forces are well beyond linear elastic regime, but still provide bonding across the crack faces.[104] Atomistic simulations of crack tips [96-99, 111, 112] require details of interatomic forces, which could be obtained experimentally.

Regarding crack dynamics, both of the continuum theory[113] and atomic models/simulations[99,100] assumed directional propagation of stress wave along the crack path, which is usually harmonic. However, many macroscopic experiments have revealed large discrepancies between the cracks in real brittle materials and the dynamical fracture theories. For example, the crack extension mode and velocity can be different in LEFM model and the MD results, which suggesting there are unknown mechanisms.[114] Figure 1.19 shows the reduced load on a silicon single crystal, which presents a model for the brittle cracking behavior

of silicon. The result presents threshold crack speed can be caused by the localized phase

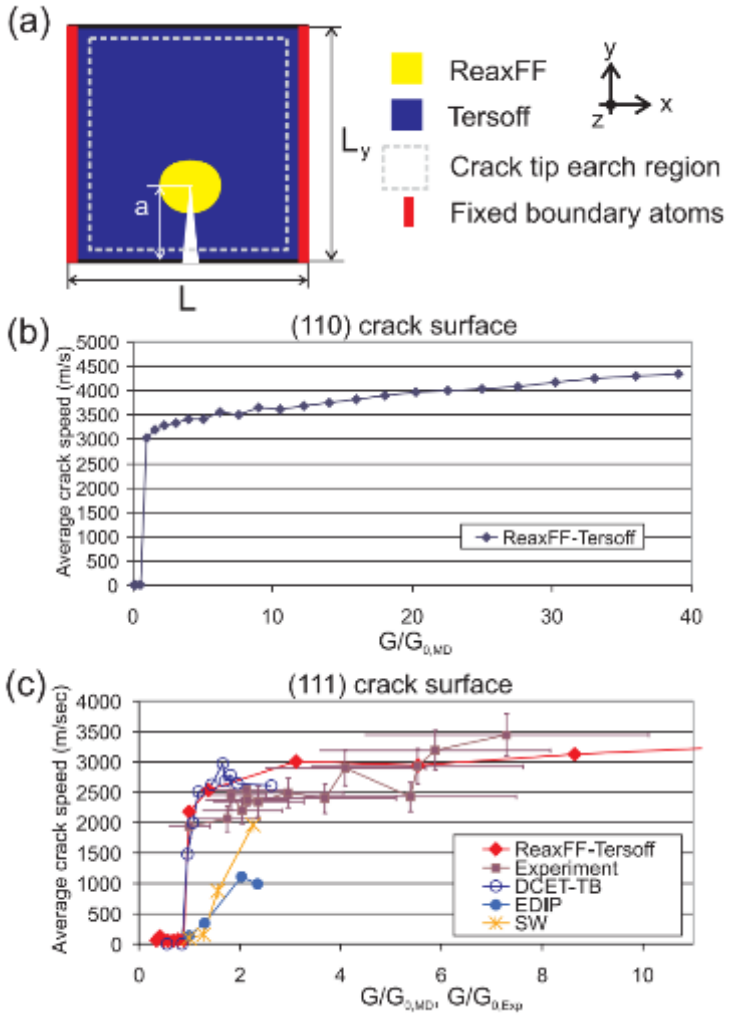

Figure 1.19 (a) Geometry of a crack extending model; (b) relationship of crack extending speed and the reduced load in (110) crack surface; (c) relationship of crack extending speed and the reduced load in (111) crack surface.[114]

transition of the lattice structure of the material, which means the rearrangement of the atoms can influence the mechanical properties and change the fracture behavior. When the loading strain is applied, the crystal orientates from two different lattice direction systems ([110] and [111] in this case). The inharmonic atomic motions induced by the specific atomic configurations in crack tips can serve as additional thermal dissipation pathways for the

cracking, and lower the crack velocity.[94] The central difficulty in experimental real-time capture on atomic structure of a fast propagating crack is the tradeoff between the spatial resolution and temporal resolution in conventional microscopes. With the help of *in situ* STEM, it is achievable to characterize cracks in 2D materials[115] which are ideal samples to study the fundamentals of cracks with atomic resolutions. The extension cracks in MoS_2 has been capture by HAADF with *in situ* STEM mode as shown in Figure 1.20.[116] The 80kV acceleration voltage from electron beam of STEM with a resolution of 0.07 nm provides enough energy for the propagation of the crack on monolayer. Different from

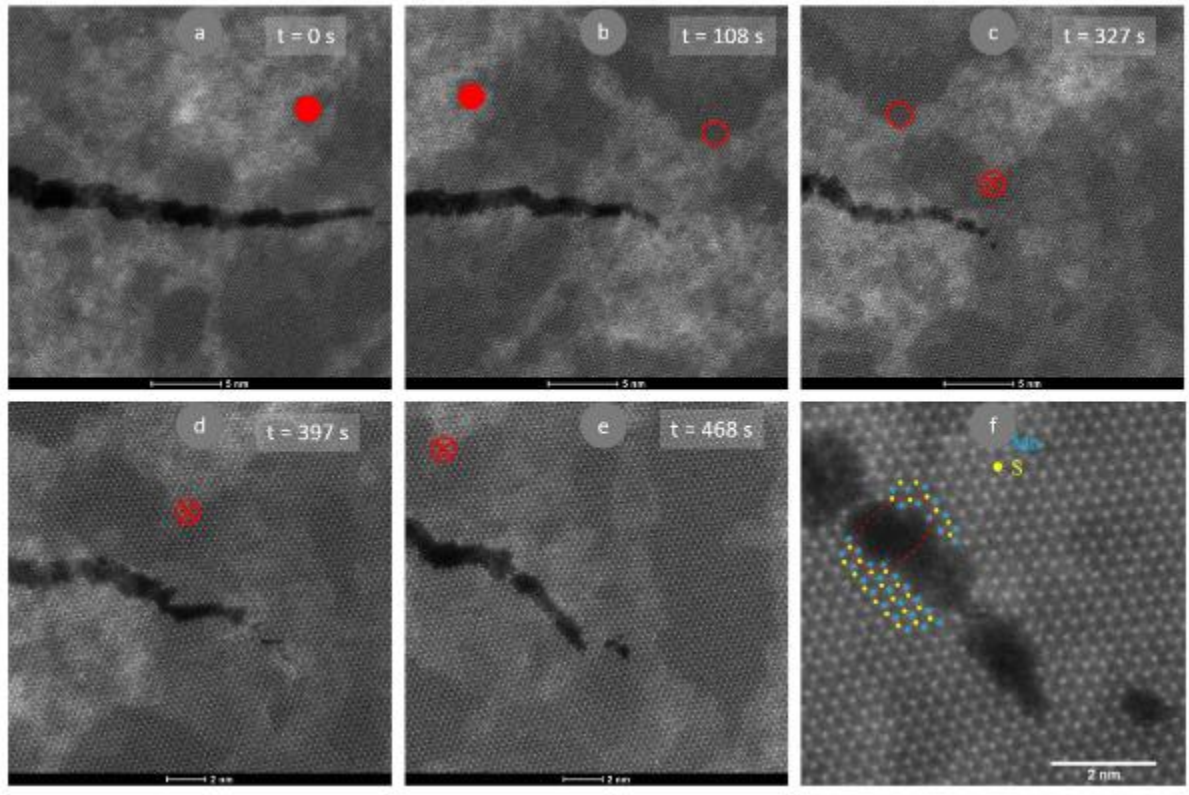

Figure 1.20 HAADF image of crack propagation in monolayer MoS_2.[116]

cracks under mechanical loading, there is usually atomic defects generated by electron beam, but here it is negligible since no structural damage is observed. Most of the crack edge is along

the zig-zag than the arm-chair, even though the energy of arm-chair is lower. This phenomenon is caused by the strain field, it also illustrates that the fracture in MoS_2 is not brittle. Also, the crack direction can switch from one zig-zag plane to another zig-zag plane, influenced by various factors such as defects and contamination on the surface of the material. The ultrahigh flexibility and lattice switching capability of 2D MoS_2 membranes allows for the angstrom-scale displacement control in the vicinity of crack tip.

In another study on crack propagation in MoS_2, the plastic deformation zone in crack tips are observed to relieve the stress and strain, enlarging the mechanical energy absorption area

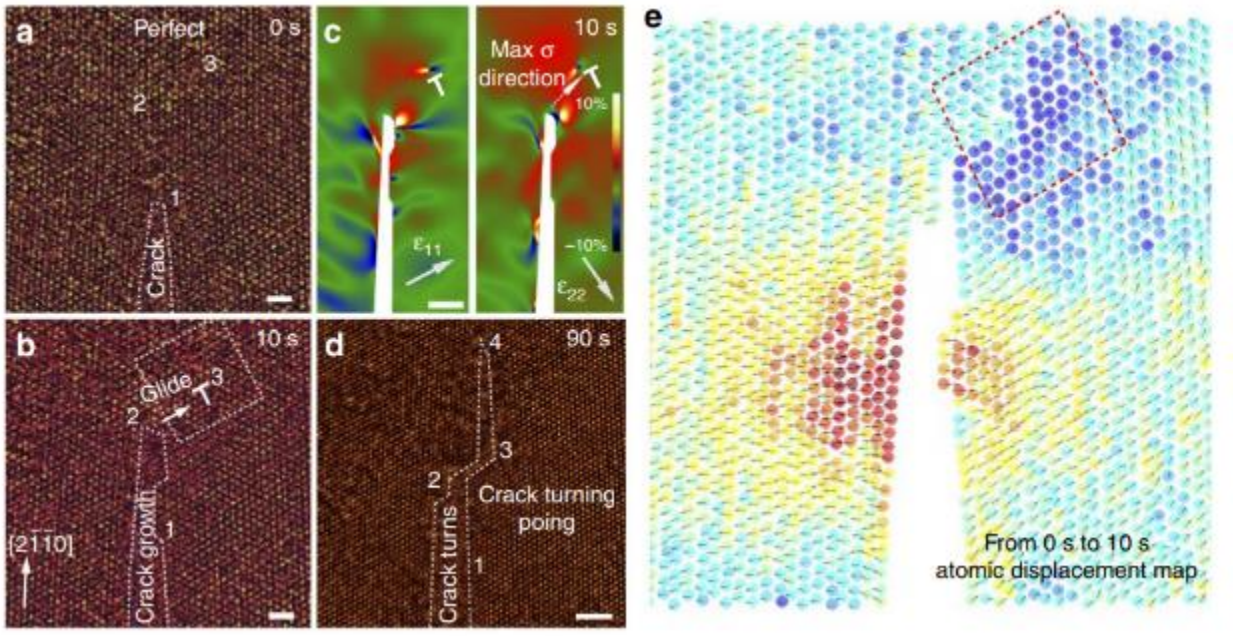

Figure 1.21 The *in situ* TEM observation of crack propagation in monolayer MoS_2. (a, b, d) the TEM observation of crack in different moments; (c) the strain distribution of the tip of the crack; (e) the atomic model of the displacement from 0s to 10s.[117]

during fracture.[117] The mapping of strain distribution near crack is based on the atomic images of monolayer MoS_2. It has been noticed there is usually dislocations near the tip of cracks and more dislocations can be generated with the extension of cracks. Figure 1.21c shows the geometric phase analysis (GPA) of the tensile strain, it indicates that the direction of maximum tensile strain is always towards new dislocation. From the atomic figures and modeling, the slip plane of monolayer MoS_2 can be recognized, thus the type of fracture behavior can also be decided.

1.2.4 Three-Dimensional Dynamic Process: Wrinkling

Wrinkles widely exist in the natural and artificial membranes, they can store considerable elastic (bending) energy in case suitable boundary conditions are imposed. Normally, wrinkles are unstable if the boundaries or fixtures are allowed to relax.[118] Mechanical description of wrinkles is generally based on the continuum theory[**Error! Reference source not found.**120] mostly on a stretched film. The relationship of the wavelength and amplitude of wrinkles is measured and results can be extended to tensile as well as shear anisotropic inelastic sheets. In the experiment, the wrinkles are made on a polyethylene sheet with the thickness of 0.01cm and 12cm width (Figure 1.22a), the linear trend of wavelength and amplitude is also measured (Figure 1.22b).[119] Similar experiment is conducted in another work to measure the geometry of wrinkling.[120] It works on the wrinkles not only on thin films but also on thick solid materials like apple or skin. The result illustrates the relationship of compression strain, bending stiffness and effective elastic foundation of stiffness. For the mechanism behind, the formation of

wrinkles is caused by the geometric packing constraint. The bending stiffness influences short wavelength and the effective elastic foundation of stiffness influences long wavelength, they work together to decide the geometry of wrinkles on an elastic film.

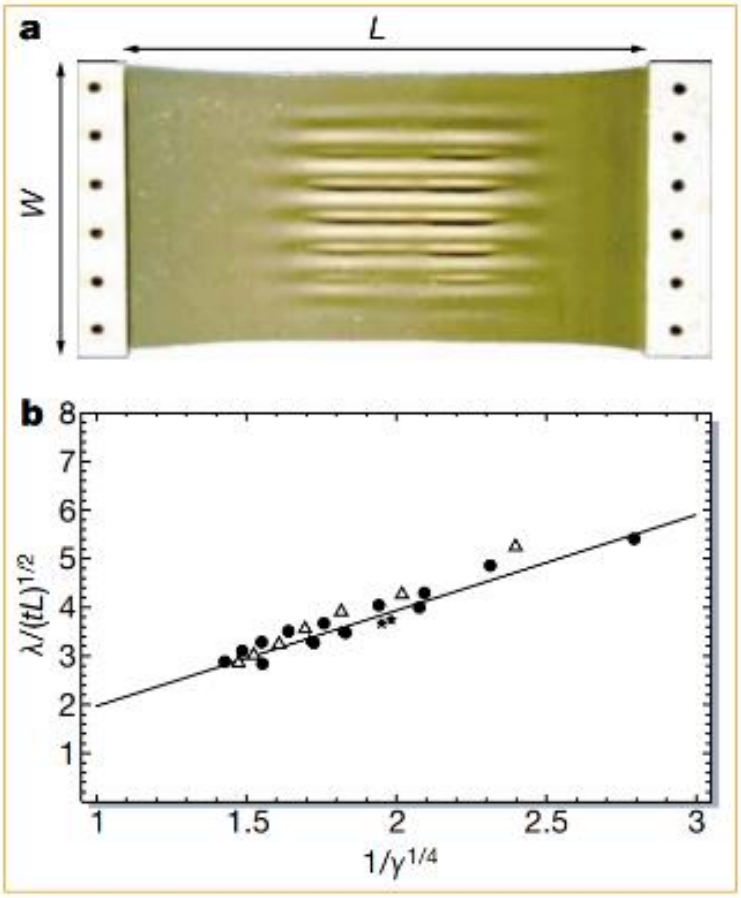

Figure 1.22. Wrinkles in an elastic film. (a) Photograph of the film under a uniaxial tensile strain. (b) Plot of the relationship between the wavelength and amplitude.[119]

For the smaller bending rigidity of thinner membranes, winkling is more easily triggered. However, for membranes with thickness down to atomic-scale, influences from the significant surface interactions should be taken into account and the continuum mechanics does not suit

atomic or nano-sized objects,[121] which create substantial difficulties on the mechanical analysis (Figure 1.23).

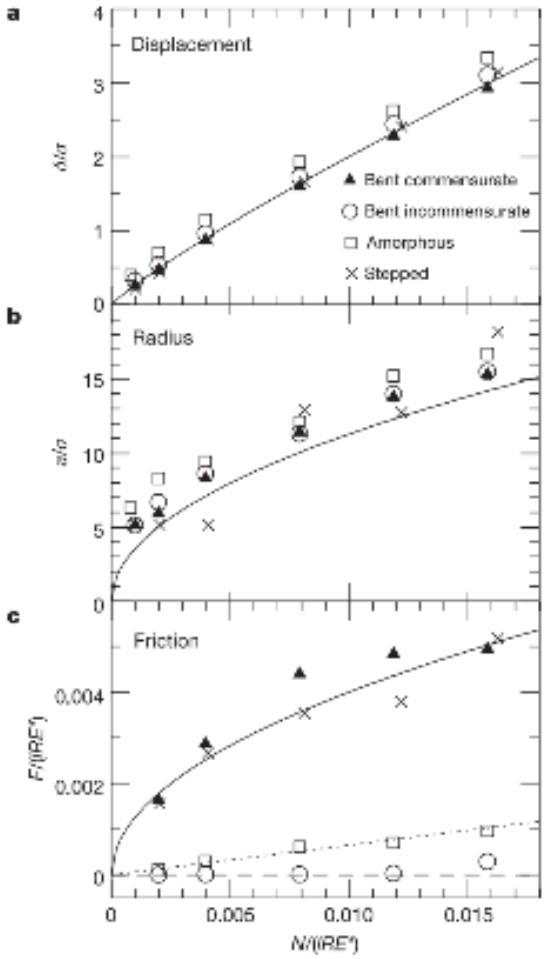

Figure 1.23 Relationship of normal load with normal displacement, contact radius and friction force. (a) Plots of normal displacement under normal load. (b) Plots of contact radius under normal load. (c) Plots of static friction under normal load.[121]

When it comes to 2D materials,[122122123] such as graphene and MoS_2 mono-atomic layer which are known to have ultra-thin atomic-layered membranes,[124-126] their properties caused by high flexibility attract a lot of interest during recent years. Specifically, nanotubes with nm-

diameters can be formed by folded[127] or creased[128] 2D membranes[129, 130]. Meanwhile, wrinkles are frequently observed with compressive or bending stress on 2D materials, particularly with respect to the substrates.[131] As shown in Figure 1.24, the relationship of radius and potential energy can be told for the crumpled graphene sheets. The surface area of graphene changes with the deformation, as a result the conductivity changes as well. The self-folding of graphene continuously creates different radius values and the potential energy decreases with the reduction of radius. The linear trend of logarithm on equilibrium radius versus the logarithm of initial length which illustrates the self-adhesion decrease the energy. Even without intention, wrinkles can be formed during the fabrication and especially

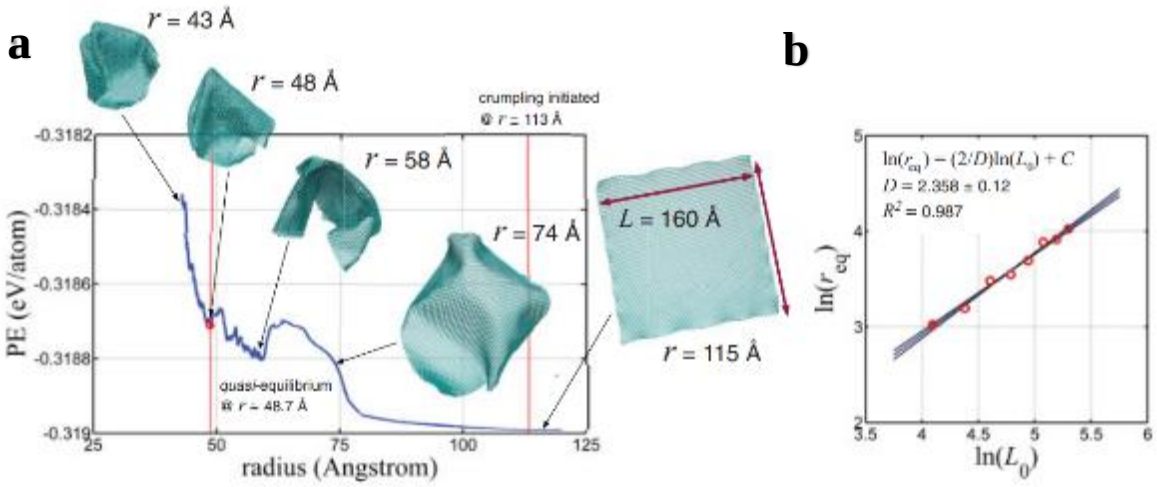

Figure 1.24 (a) Change of potential energy during crumpling when the radius changes. (b) The linear regression of the logarithm of equilibrium radius and the logarithm of initial length.[131]

the post-processing/transferring of 2D materials,[132] suggesting the undermined performances in applications. DFT calculation gives the accurate and maximum value of the interaction energy on the substrate than several other empirical force fields, as shown in Figure 1.25. The

mechanical, electrical/electronic and thermal properties can all be potentially influenced by wrinkles.[133] For example, the ripples can influence the bandgap of a monolayer graphene and change the rate of carrier puddles. On mechanical properties, the wavelength and amplitude of wrinkles are effected by the van der Waals forces in single layer materials which cause different bending behaviour. Crumples can easily influence the electronic properties in the

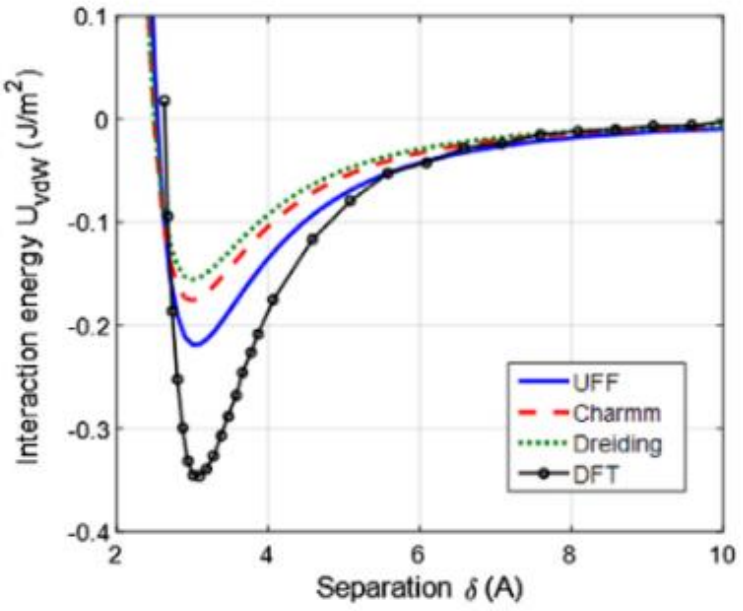

Figure 1.25 Interaction energy between graphene and silicon oxide, calculated by DFT and empirical force fields.[132]

applications as strain sensing or energy storage devices. The brief relationship of the formation defects and properties in graphene is summarized in Figure 1.26. In another aspect, wrinkles, particularly with designable textured architectures, play important roles in stretchable and flexible devices[134] as well as in nano-fluidic devices[135], which enrich the application areas of 2D materials.

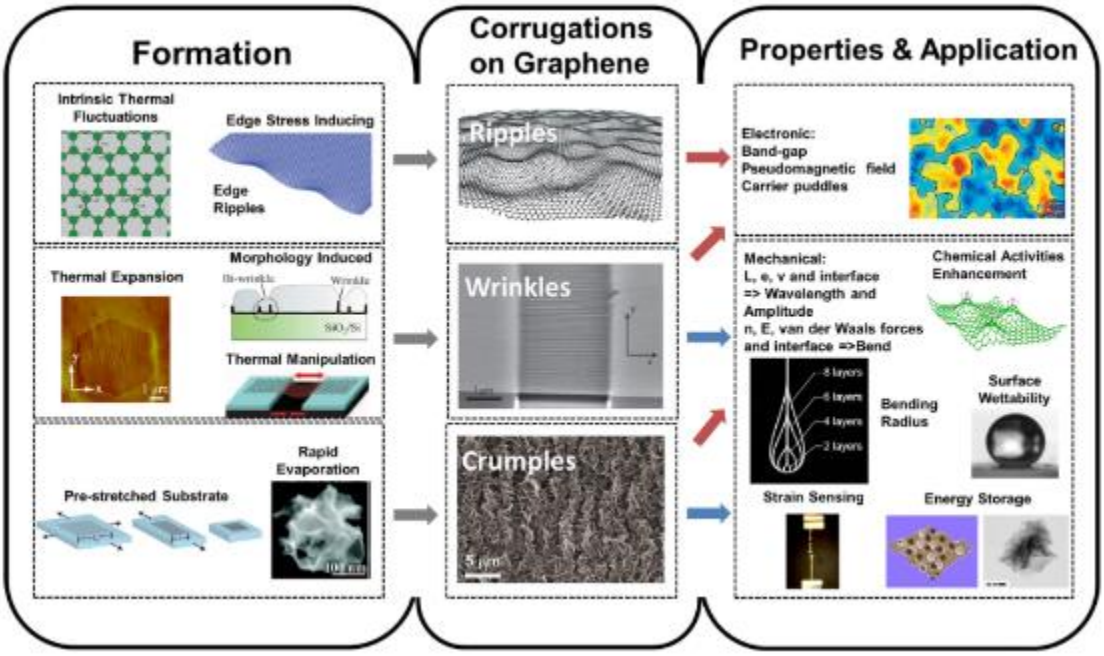

Figure 1.26 A summary illustration of corrugations on graphene formation, properties and application. Gray arrows stand for formation of corrugations on graphene, redarrows indicate electronic properties and blue arrows for other properties.[133]

Wrinkles in 2D materials have been recently studied by atomic force microscopy (AFM)[136], scanning tunnelling microscopy (STM)[137] and TEM[138], their structures as well as the modulated electronic band structures which are quite different from the flat zones.[139] However, the mechanical stability and the dynamical behaviour of individual wrinkles have not been clearly addressed, especially by direct experimental observation under nanoscale, to compare with theoretical DFT calculation.[140] So far, in experiments, only the accessible basal-plane

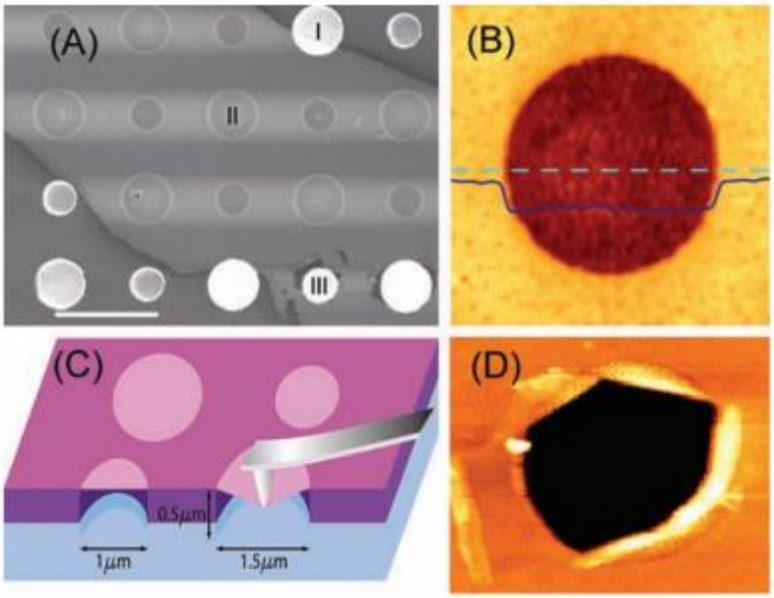

Figure 1.27 Images of free standing graphene monolayer. (a) Scanning electron micrograph of suspended monolayer graphene. (b) AFM image of a completed graphene membrane. (c) Schematic diagram of nanoindentation from AFM tip on monolayer graphene. (d) AFM image of a fractured graphene membrane.[141]

tensile tests on 2D materials has been achieved by nanoindentation from AFM.[141] From the AFM results, different size of diamond tips on cantilevers are used to make the hole and folding behaviour occurs spontaneously since the graphene membrane is freestanding. The AFM figures and schematic diagram are shown in Figure 1.27 and in this way, the relationship of load force and indentation depth of each tip can be measured. However, at present, the continuous flexural properties of 2D materials and the quantitative descriptions are still in absence.

1.3 Challenges and Opportunities in 2D Materials Study: *In Situ* (S)TEM

1.3.1 2D Materials under (S)TEM

Among various structure characterization methods of materials, TEM is one of the most popular and powerful tools. The accelerated and concentrated electron beam from electron gun in TEM is sent onto a very thin sample, and the electrons collide with the atoms in the sample to change direction, resulting in elastic and inelastic scattering. The density and thickness of the sample decides the scattering angle thus images with different brightness and darkness can be formed.[142] With the development of modern TEM such as Cs correctors, it is becoming more and more important for atomic characterizations, especially for the 2D materials. By using TEM, the morphology of the samples and the crystal structures can be unambiguously resolved. Selected area electron diffraction (SAED) shows the crystal structures in reciprocal space, while in TEM especially STEM images, the spatial and elemental information on single atomic scale can be directly identified. Figure 1.28 shows the morphology of MoS_2 with different layer thicknesses by HRTEM. The Moiré patterns are formed due to the rotation angel between the layers. Their SAED patterns are both six-folded symmetric with different diffraction spot sets corresponding to the different layers.[143]

In another case, the heterostructure is observed by *in situ* TEM method. Figure 1.29 shows the heterostructures of ReS_2/WS_2 and MoS_2/WS_2.[144] In ReS_2/WS_2, layers are twisted in a

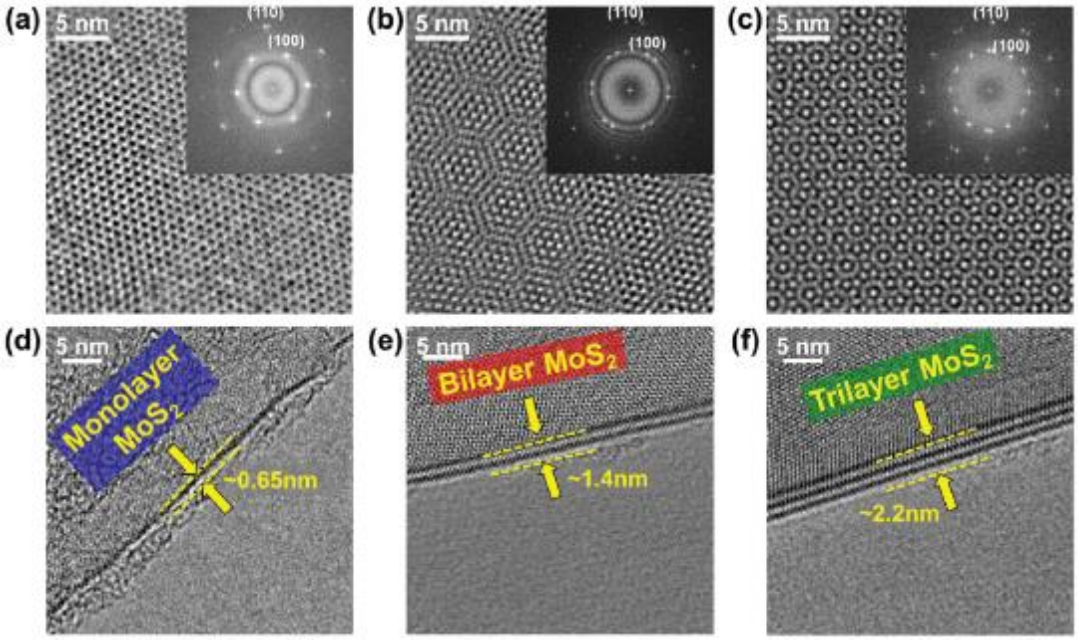

Figure 1.28 HRTEM images of MoS_2 with 1, 2, 3 layers and their corresponding diffraction patterns.[143]

certain angle which can be measured from FFT. The atomic structure of vertical stacking is characterized from HRTEM and the Moire pattern showing in HRTEM also illustrates the interlayer twisting angle of the material. The image of multilayer MoS_2/WS_2 is clearly observed by HRTEM on a SiO_2 substrate which indicates the seamless heterointerface of different layers.

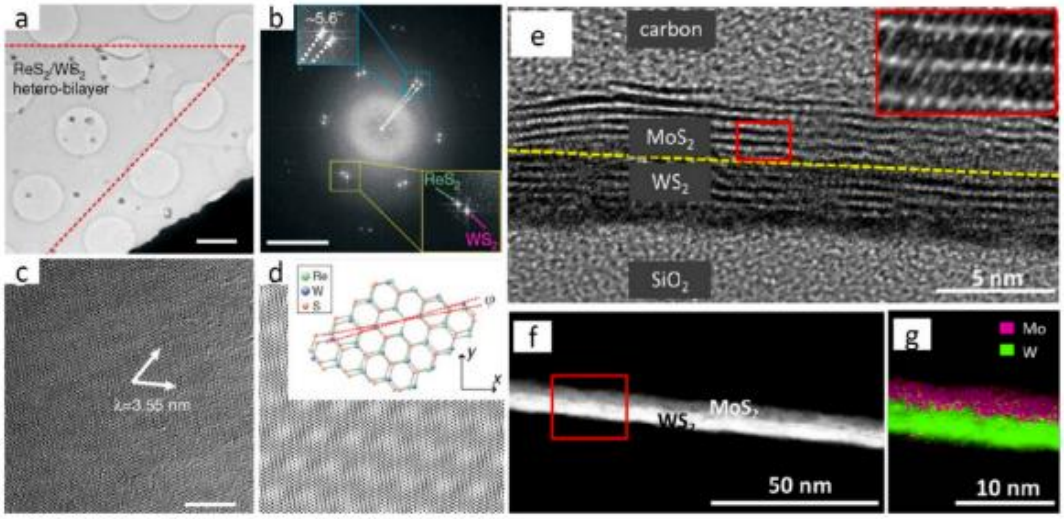

Figure 1.29 The heterostructure of different TMDs materials. (a) The TEM low-magnification of ReS_2/WS_2. (b)SAED pattern of bilayer in (a). (c, d) HRTEM image of the heterostructure of bilayer. (e) Multilayer heterostructure of MoS_2/WS_2. (f, g) EDS mapping of cross-sectional STEM-ADF image of a vertically stacked MoS_2/WS_2 heterostructure.[144]

1.3.2 2D Materials under *In Situ* (S)TEM

In STEM mode, previous works have tried to observed the change of atomic structures driven by the electron beam energy. With the converged electron beam in STEM mode, lithography engineering can be conducted on 2D materials. The electron-driven techniques are used not only in the understanding of fundamental properties of materials but also in nanocircuits and devices engineering.[145-147] On $Mo_xW_{1-x}Se_2$, the change of shape on the edge under electron energy has been well captured. Figure 1.30 exhibits the shape evolution of an initial nanowire-terminated parallelogram pore.[148] The initial pore with a

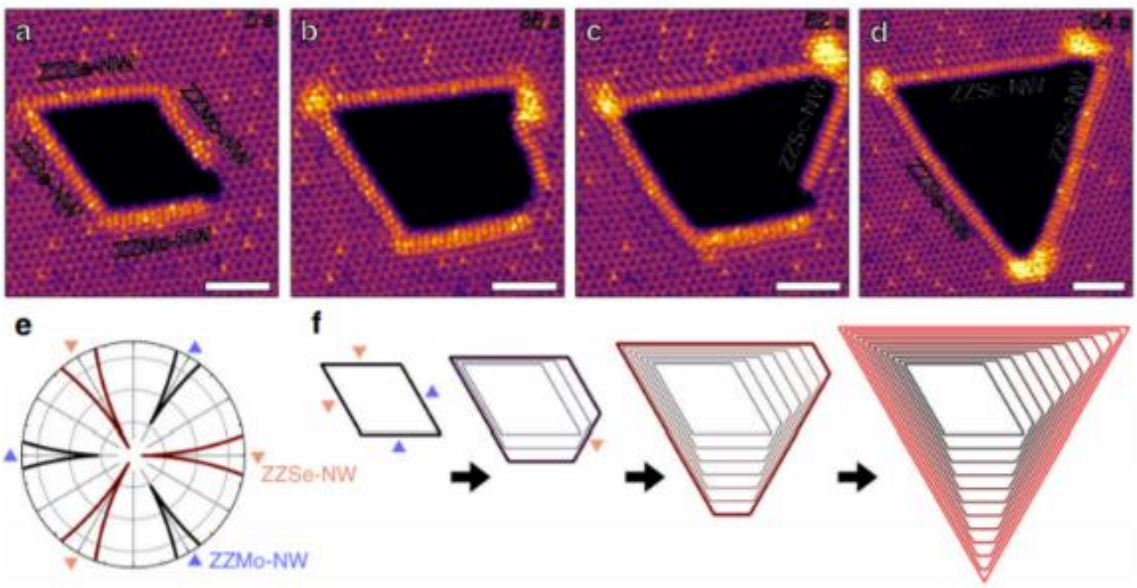

Figure 1.30 (a-d) The change of edge on $Mo_xW_{1-x}Se_2$ under electron beam driven scanning. (e) Polar plot of etching rates of different types of edges. (f) Simulated etching progress of of (a-d). Scale bar =2nm.[148]

parallelogram shape changes into triangle shape on Se-nanowire and Mo-nanowire sides and the two Mo-nanowire sides disappears as time goes by. The simulation of the whole process is schematized in Figure 1.30f.

The phase lithography driven by electron beam was firstly conducted on a MoS_2 monolayer sample (Figure 1.31).[149] The phase transition from pristine 2H to 1T was observed when the beam scans on the material. Between the two phases, there are boundaries

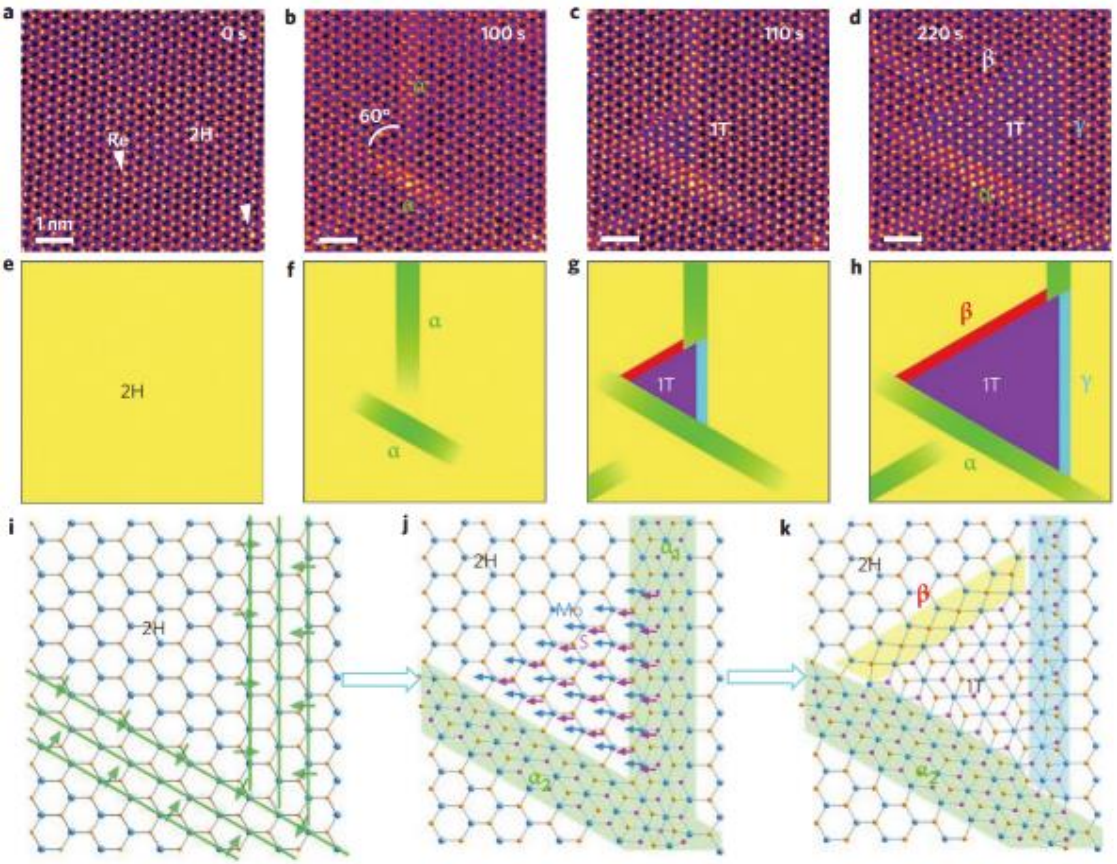

Figure 1.31 Process of phase transition on MoS_2 from 2H to 1T phase. (a-d) The HAADF image of atomic structure. (e-h) Schematic diagrams of different phases areas. (i-k) Simulation of atomic movement during phase transition.[149]

which are different on different lattice orientation directions, this is due to the point defects of Mo and S under the strain. The dynamic process here is complicated, phase boundaries, initial phase and final phase are all decided by the gliding planes, and the phase transition is triggered by the accumulating negative charge from the electron beam irradiation. The energy on the movement of the atoms largely depends on the lattice orientations so there are three types of boundaries according to three directions of MoS_2 atomic structure.

Despite the analysis on 2D TMDs by (S)TEM for years, understanding on dynamical mechanism on defects, phase transition and doping engineering in atomic scale is still lacking. The relationship between bandgaps and atomic structure has not being figured out. At the same time, dynamical properties in mesoscale or nanoscale owning to the reduced dimensions as well as broken of symmetry and topology are under discovery. Further studies by (S)TEM are promising to provide a better understanding on the atomic and dynamic properties of 2D materials.

1.4 Objective of Research

Currently, 2D materials has been observed and analyzed by various characterizations and modes. For the *in situ* tests on 2D materials, many studies use characterization methods such as SEM, AFM or OM and test the change of dynamical, electronic and optical properties in devices. However, these methods mainly provide a macroscopical (in micrometer scale or above) observation on the deformation of samples. The relationship of atoms, electrons with energy in atomic level is hard to achieve without direct characterization in nanoscale. During the last few years, the popularity of (S)TEM makes the atomic figures with high resolutions acquirable, but the *in situ* continuous change of atoms has barely been captured. The main barrier is the difficulty of applying strains precisely in nanoscale while recording the change of crystal lattice at the same time. In our work, we want to realize the *in situ* strain application in atomic resolution mainly using (S)TEM with the help of STM when the properties tests are needed.

In the first strategy, for the electron beam-driven dynamical studies, we employ JEM-ARM200F transmission electron microscope (TEM) operated with a 60 kV accelerating voltage on monolayer ReS_2. Atomic structures in grain boundaries, phase transition and fracture behavior can be clearly observed and the electron beam can provide enough energy to cause defects without damaging the sample. Controlling the density of irradiation by converging the beam can generate different defects on 2D materials, at the same time, the real-time change of lattice structure can be captured by STEM. In the second strategy, for wrinkling behaviors, a force from out-of-plane direction is needed. A tungsten (W) tip with the width of

several nanometers made by corrosion is fixed on a Nanofactory STM-TEM holder. Generation and elimination of wrinkles can be created on samples inside TEM with the control on the movement of the W tip, and the whole process is recorded in the video. This setup can also be used for conductivity test, combining with Keithley 2400 with a LabVIEW program using for I-V data collection.

With the above methods, we obtain the structure of pristine monolayer first, and generate different dynamical deformations including cracks, grain boundaries, as well as different phases. The continuous changes of lattice structure are recorded every 10 to 20 seconds such as the propagation of cracks, switch of mobile grain boundaries, as well as the process of phase transitions. For analysis, mechanical modeling provides the quantified calculations of dynamical properties and DFT calculation theoretically explains the phenomenon from experiments. Combining the atomic figures and theoretical calculation results, we are able to make a comprehensive understanding on the dynamical properties in atomic level, the energy of the crystal structures and defects, together with the direct observation of morphology on 2D materials.

Reference:

1. Novoselov, K. S.; Geim, A. K.; Morozov, S. V.; Jiang, D. E.; Zhang, Y.; Dubonos, S. V.; Firsov, A. A. Electric field effect in atomically thin carbon films. *Science* **2004**, *306*, 666-669.
2. Hasan, M. Z.; Kane, C. L. Colloquium: topological insulators. *Reviews of modern physics* **2010**, 82, 3045.
3. Splendiani, A.; Sun, L., Zhang, Y.; Li, T.; Kim, J.; Chim, C. Y.; Wang, F. Emerging photoluminescence in monolayer MoS_2. *Nano letters* **2010**, 10, 1271-1275.
4. Li, L.; Yu, Y.; Ye, G. J.; Ge, Q.; Ou, X.; Wu, H.; Zhang, Y. Black phosphorus field-effect transistors. *Nature nanotechnology* **2014**, 9, 372-377.
5. Neto, A. C.; Guinea, F.; Peres, N. M.; Novoselov, K. S.; Geim, A. K. The electronic properties of graphene. *Reviews of modern physics* **2009**, 81, 109.
6. Radisavljevic, B.; Radenovic, A.; Brivio, J.; Giacometti, V.; Kis, A. Single-layer MoS_2 transistors. *Nature nanotechnology* **2011**, 6, 147-150.
7. Khossossi, N.; Singh, D.; Ainane, A.; Ahuja, R. Recent progress of defect chemistry on 2D materials for advanced battery anodes. *Chemistry–an asian journal* **2020**, 15, 3390-3404.
8. Hong, J.; Hu, Z.; Probert, M.; Li, K.; Lv, D.; Yang, X.; Zhang, Z. Exploring atomic defects in molybdenum disulphide monolayers. *Nature communications* **2015**, 6, 1-8.
9. Cao, D.; Shen, T.; Liang, P.; Chen, X.; Shu, H. Role of chemical potential in flake shape and edge properties of monolayer MoS_2. *The journal of physical chemistry c* **2015**, 119, 4294-4301.
10. Wang, Y.; Li, S.; Yi, J. Electronic and magnetic properties of Co doped MoS_2 monolayer. *Scientific reports* **2016**, 6, 1-9.

11. Liu, Z.; Amani, M.; Najmaei, S.; Xu, Q.; Zou, X.; Zhou, W.; Lou, J. Strain and structure heterogeneity in MoS_2 atomic layers grown by chemical vapour deposition. *Nature communications* **2014**, 5, 1-9.
12. Najmaei, S.; Liu, Z.; Zhou, W.; Zou, X.; Shi, G.; Lei, S.; Lou, J. Vapour phase growth and grain boundary structure of molybdenum disulphide atomic layers. *Nature materials* **2013**, 12, 754-759.
13. Zhao, J.; Deng, Q.; Ly, T. H.; Han, G. H.; Sandeep, G.; Rümmeli, M. H. Two-dimensional membrane as elastic shell with proof on the folds revealed by three-dimensional atomic mapping. *Nature communications* **2015**, 6, 1-6.
14. Luo, S.; Hao, G.; Fan, Y.; Kou, L.; He, C.; Qi, X.; Zhong, J. Formation of ripples in atomically thin MoS_2 and local strain engineering of electrostatic properties. *Nanotechnology* **2015**, 26, 105705.
15. Choi, W.; Choudhary, N.; Han, G. H.; Park, J.; Akinwande, D.; Lee, Y. H. Recent development of two-dimensional transition metal dichalcogenides and their applications. *Materials today* **2017**, 20, 116-130.
16. Yang, L.; Majumdar, K.; Liu, H.; Du, Y.; Wu, H.; Hatzistergos, M.; Ye, P. D. Chloride molecular doping technique on 2D materials: WS_2 and MoS_2. *Nano letters* **2014**, 14, 6275-6280.
17. Lu, N.; Guo, H.; Li, L.; Dai, J.; Wang, L.; Mei, W. N.; Zeng, X. C. MoS_2/MX_2 heterobilayers: bandgap engineering via tensile strain or external electrical field. *Nanoscale* **2014**, 6, 2879-2886.

18. Tongay, S.; Suh, J.; Ataca, C.; Fan, W.; Luce, A.; Kang, J. S.; Ogletree, F. Defects activated photoluminescence in two-dimensional semiconductors: interplay between bound, charged, and free excitons. *Scientific reports* **2013**, 3, 2657.
19. Cong, C.; Shang, J.; Wu, X.; Cao, B.; Peimyoo, N.; Qiu, C.; Yu, T. Synthesis and optical properties of large - area single - crystalline 2D semiconductor WS_2 monolayer from chemical vapor deposition. *Advanced optical materials* **2014**, 2, 131-136.
20. Chen, Z.; Biscaras, J.; Shukla, A. Optimal light harvesting in 2D semiconductor heterostructures. *2D materials* **2017**, 4, 025115.
21. Xia, J.; Yan, J.; Wang, Z.; He, Y.; Gong, Y.; Chen, W.; Shen, Z. Strong coupling and pressure engineering in WSe_2–$MoSe_2$ heterobilayers. *Nature physics* **2021**, 17, 92-98.
22. Tongay, S.; Fan, W.; Kang, J.; Park, J.; Koldemir, U.; Suh, J.; Sinclair, R. Tuning interlayer coupling in large-area heterostructures with CVD-grown MoS_2 and WS_2 monolayers. *Nano letters* **2014**, 14, 3185-3190.
23. Zheng, Z.; Zhang, T.; Yao, J.; Zhang, Y.; Xu, J.; Yang, G. Flexible, transparent and ultra-broadband photodetector based on large-area WSe_2 film for wearable devices. *Nanotechnology* **2016**, 27, 225501.
24. Chhowalla, M.; Liu, Z.; Zhang, H. Two-dimensional transition metal dichalcogenide (TMD) nanosheets. *Chemical society reviews* **2015**, 44, 2584-2586.
25. Kirkpatirck, S. R.; Siahmakoun, A.; Adams, T. M.; Wang, Z. U.S. Patent No. 7,444,812. *Washington, DC: U.S. Patent and Trademark Office* **2008**.
26. Liu, K.; Yan, Q.; Chen, M.; Fan, W.; Sun, Y.; Suh, J.; Ji, J. Elastic properties of chemical-vapor-deposited monolayer MoS_2, WS_2, and their bilayer heterostructures. *Nano letters* **2014**, 14, 5097-5103.

27. Novoselov, K. S.; Mishchenko, O. A.; Carvalho, O. A.; Neto, A. C. 2D materials and van der Waals heterostructures. *Science* **2016**, 353(6298).

28. Huang, P. Y.; Ruiz-Vargas, C. S.; Van Der Zande, A. M.; Whitney, W. S.; Levendorf, M. P.; Kevek, J. W.; Muller, D. A. Grains and grain boundaries in single-layer graphene atomic patchwork quilts. *Nature* **2011**, 469, 389-392.

29. Gass, M. H.; Bangert, U.; Bleloch, A. L.; Wang, P.; Nair, R. R.; Geim, A. K. Free-standing graphene at atomic resolution. *Nature nanotechnology* **2008**, 3, 676-681.

30. Hultgren, R.; Gingrich, N. S.; Warren, B. E. The atomic distribution in red and black phosphorus and the crystal structure of black phosphorus. *The journal of chemical physics* **1935**, 3, 351-355.

31. Liu, Y.; Zhao, J.; Li, Z., Mu, C.; Ma, W.; Hu, H.; Yan, H. Aggregation and morphology control enables multiple cases of high-efficiency polymer solar cells. *Nature communications* **2014**, 5, 1-8.

32. Ci, L.; Song, L.; Jin, C.; Jariwala, D.; Wu, D.; Li, Y.; Ajayan, P. M. Atomic layers of hybridized boron nitride and graphene domains. *Nature materials* **2010**, 9, 430-435.

33. Mahatha, S. K.; Patel, K. D.; Menon, K. S. Electronic structure investigation of MoS_2 and $MoSe_2$ using angle-resolved photoemission spectroscopy and ab initio band structure studies. *Journal of physics: condensed matter* **2012**, 24, 475504.

34. Keyshar, K.; Gong, Y.; Ye, G.; Brunetto, G.; Zhou, W.; Cole, D. P.; Ajayan, P. M. Chemical vapor deposition of monolayer rhenium disulfide (ReS_2). *Advanced materials* **2015**, 27, 4640-4648.

35. Liu, B.; Fathi, M.; Chen, L.; Abbas, A.; Ma, Y.; Zhou, C. Chemical vapor deposition growth of monolayer WSe_2 with tunable device characteristics and growth mechanism study. *ACS nano* **2015**, 9, 6119-6127.
36. Liu, E.; Fu, Y.; Wang, Y.; Feng, Y.; Liu, H.; Wan, X.; Xing, D. Integrated digital inverters based on two-dimensional anisotropic ReS_2 field-effect transistors. *Nature communications* **2015**, 6, 1-7.
37. Wolverson, D.; Crampin, S.; Kazemi, A. S.; Ilie, A.; Bending, S. J. Raman spectra of monolayer, few-layer, and bulk ReSe2: an anisotropic layered semiconductor. *ACS nano* **2014**, 8, 11154-11164.
38. Ly, T. H.; Chiu, M. H.; Li, M. Y.; Zhao, J.; Perello, D. J.; Cichocka, M. O.; Lee, Y. H. Observing grain boundaries in CVD-grown monolayer transition metal dichalcogenides. *ACS nano* **2014**, 8, 11401-11408.
39. Azizi, A.; Zou, X.; Ercius, P.; Zhang, Z.; Elías, A. L.; Perea-López, N.; Alem, N. Dislocation motion and grain boundary migration in two-dimensional tungsten disulphide. *Nature communications* **2014**, 5, 1-7.
40. Ding, N.; Wu, C. M. L.; Li, H. The effect of grain boundaries on the mechanical properties and failure behavior of hexagonal boron nitride sheets. *Physical chemistry chemical Physics* **2014**, 16, 23716-23722.
41. Karvonen, L.; Säynätjoki, A.; Huttunen, M. J.; Autere, A.; Amirsolaimani, B.; Li, S.; Sun, Z. Rapid visualization of grain boundaries in monolayer MoS_2 by multiphoton microscopy. *Nature communications* **2017**, 8, 1-8.

42. Liu, T. H.; Gajewski, G.; Pao, C. W.; Chang, C. C. Structure, energy, and structural transformations of graphene grain boundaries from atomistic simulations. *Carbon* **2011**, 49, 2306-2317.
43. Zou, X.; Liu, Y.; Yakobson, B. I. Predicting dislocations and grain boundaries in two-dimensional metal-disulfides from the first principles. *Nano letters* **2013**, 13, 253-258.
44. Winning, M.; Gottstein, G.; Shvindlerman, L. S. Stress induced grain boundary motion. *Acta materialia* **2001**, 49, 211-219.
45. Van Der Zande, A. M.; Huang, P. Y.; Chenet, D. A.; Berkelbach, T. C.; You, Y.; Lee, G. H.; Hone, J. C. Grains and grain boundaries in highly crystalline monolayer molybdenum disulphide. *Nature materials* **2013**, 12, 554-561.
46. Ghorbani-Asl, M.; Enyashin, A. N.; Kuc, A.; Seifert, G.; Heine, T. Defect-induced conductivity anisotropy in MoS_2 monolayers. *Physical review B* **2013**, 88, 245440.
47. Ly, T. H.; Perello, D. J.; Zhao, J.; Deng, Q.; Kim, H.; Han, G. H.; Lee, Y. H. Misorientation-angle-dependent electrical transport across molybdenum disulfide grain boundaries. *Nature communications* **2016**, 7, 1-7.
48. He, Y.; Tang, P.; Hu, Z.; He, Q.; Zhu, C.; Wang, L.; Liu, Z. Engineering grain boundaries at the 2D limit for the hydrogen evolution reaction. *Nature communications* **2020**, 11, 1-12.
49. Ly, T. H.; Perello, D. J.; Zhao, J.; Deng, Q.; Kim, H.; Han, G. H.; Lee, Y. H. Misorientation-angle-dependent electrical transport across molybdenum disulfide grain boundaries. *Nature communications* **2016**, 7, 1-7.
50. Lin, Z.; Carvalho, B. R.; Kahn, E.; Lv, R.; Rao, R.; Terrones, H.; Terrones, M. Defect engineering of two-dimensional transition metal dichalcogenides. *2D materials* **2016**, 3, 022002.

51. Kurasch, S.; Kotakoski, J.; Lehtinen, O.; Skákalová, V.; Smet, J.; Krill III, C. E.; Kaiser, U. Atom-by-atom observation of grain boundary migration in graphene. *Nano letters* **2012**, 12, 3168-3173.

52. Dumay, A.; Chateau, J. P.; Allain, S.; Migot, S.; Bouaziz, O. Influence of addition elements on the stacking-fault energy and mechanical properties of an austenitic Fe–Mn–C steel. *Materials science and engineering: A* **2008**, 483, 184-187.

53. Lin, Z.; Carvalho, B. R.; Kahn, E.; Lv, R.; Rao, R.; Terrones, H.; Terrones, M. Defect engineering of two-dimensional transition metal dichalcogenides. *2D materials* **2016**, 3, 022002.

54. Peierls, R. E. Quantum Theory of Solids. *Clarendon Press* **1996**.

55. Whangbo, M. H.; Canadell, E. Analogies between the concepts of molecular chemistry and solid-state physics concerning structural instabilities. Electronic origin of the structural modulations in layered transition metal dichalcogenides. *Journal of the American chemical society* **1992**, 114, 9587-9600.

56. Neto, A. C. Charge density wave, superconductivity, and anomalous metallic behavior in 2D transition metal dichalcogenides. *Physical review letters* **2001**, 86, 4382.

57. Gruner, G. Density Waves in Solids. *CRC press* **2018**.

58. Wildervanck, J. C.; Jellinek, F. The dichalcogenides of technetium and rhenium. *Journal of the less common metals* **1971**, 24, 73-81.

59. Webb, J. L.; Hart, L. S.; Wolverson, D.; Chen, C.; Avila, J.; Asensio, M. C. Electronic band structure of ReS_2 by high-resolution angle-resolved photoemission spectroscopy. *Physical review B* **2017**, 96, 115205.

60. Tongay, S.; Sahin, H.; Ko, C.; Luce, A.; Fan, W.; Liu, K.; Wu, J. Monolayer behaviour in bulk ReS_2 due to electronic and vibrational decoupling. *Nature communications* **2014**, 5, 1-6.

61. Tsen, A. W.; Hovden, R.; Wang, D.; Kim, Y. D.; Okamoto, J.; Spoth, K. A.; Pasupathy, A. N. Structure and control of charge density waves in two-dimensional 1T-TaS_2. *Proceedings of the national academy of sciences* **2015**, 112, 15054-15059.

62. Hatt, A. J.; Spaldin, N. A.; Ederer, C. Strain-induced isosymmetric phase transition in $BiFeO_3$. *Physical review B* **2010**, 81, 054109.

63. Arav, A.; Zeron, Y.; Leslie, S. B.; Behboodi, E.; Anderson, G. B.; Crowe, J. H. Phase transition temperature and chilling sensitivity of bovine oocytes. *Cryobiology* **1996**, 33, 589-599.

64. Braun-Munzinger, P.; Stachel, J.; Wetterich, C. Chemical freeze-out and the QCD phase transition temperature. *Physical review B* **2004**, 596, 61-69.

65. Diedrich, F.; Peik, E.; Chen, J. M.; Quint, W.; Walther, H. Observation of a phase transition of stored laser-cooled ions. *Physical review letters* **1987**, 59, 2931.

66. Lysenko, S.; Rúa, A.; Vikhnin, V.; Fernández, F.; Liu, H. Insulator-to-metal phase transition and recovery processes in VO_2 thin films after femtosecond laser excitation. *Physical review B* **2007**, 76, 035104.

67. Kimber, S. A.; Kreyssig, A.; Zhang, Y. Z.; Jeschke, H. O.; Valentí, R.; Yokaichiya, F.; Argyriou, D. N. Similarities between structural distortions under pressure and chemical doping in superconducting $BaFe_2As_2$. *Nature materials* **2009**, 8, 471-475.

68. Zheng, Y. R.; Wu, P.; Gao, M. R.; Zhang, X. L.; Gao, F. Y.; Ju, H. X.; Yu, S. H. Doping-induced structural phase transition in cobalt diselenide enables enhanced hydrogen evolution catalysis. *Nature communications* **2018**, 9, 1-9.

69. Duerloo, K. A. N.; Li, Y.; Reed, E. J. Structural phase transitions in two-dimensional Mo- and W-dichalcogenide monolayers. *Nature communications* **2014**, 5, 1-9.

70. Gao, B.; Du, X.; Li, Y.; Ding, S.; Xiao, C.; Song, Z. Deep phase transition of MoS_2 for excellent hydrogen evolution reaction by a facile C-doping strategy. *ACS applied materials & interfaces* **2019**, 12, 877-885.

71. Achal, R.; Rashidi, M.; Croshaw, J.; Churchill, D.; Taucer, M.; Huff, T.; Wolkow, R. A. Lithography for robust and editable atomic-scale silicon devices and memories. *Nature communications* **2018**, 9, 1-8.

72. Rao, C. R.; Rao, G. S.; Ramdas, S. Phase transformations and electrical properties of bismuth sesquioxide. *The journal of physical chemistry* **1969**, 73, 672-675.

73. Zuo, R.; Fang, X.; Ye, C. Phase structures and electrical properties of new lead-free $(Na_{0.5}K_{0.5})NbO_3$–$(Bi_{0.5}N_{0.5})TiO_3$ ceramics. *Applied physics letters* **2007**, 90, 092904.

74. Filip, R.; Kubiak, K.; Ziaja, W.; Sieniawski, J. The effect of microstructure on the mechanical properties of two-phase titanium alloys. *Journal of materials processing technology* **2003**, 133, 84-89.

75. Verleur, H. W.; Barker Jr, A. S.; Berglund, C. N. Optical properties of VO_2 between 0.25 and 5 eV. *Physical review* **1968**, 172, 788.

76. Mas-Balleste, R.; Gomez-Navarro, C.; Gomez-Herrero, J.; Zamora, F. 2D materials: to graphene and beyond. *Nanoscale* **2011**, 3, 20-30.

77. Yang, H.; Kim, S. W.; Chhowalla, M.; Lee, Y. H. Structural and quantum-state phase transitions in van der Waals layered materials. *Nature physics* **2017**, 13, 931-937.

78. Chau, K. W.; Yang, Y. C.; Geil, P. H. Tetragonal→ twinned hexagonal crystal phase transformation in polybutene-1. *Journal of materials science* **1986**, 21, 3002-3014.

79. Chhowalla, M.; Liu, Z.; Zhang, H. Two-dimensional transition metal dichalcogenide (TMD) nanosheets. *Chemical society reviews* **2015**, 44, 2584-2586.

80. Zhu, X.; Li, D.; Liang, X.; Lu, W. D. Ionic modulation and ionic coupling effects in MoS_2 devices for neuromorphic computing. *Nature materials* **2019**, 18, 141-148.

81. Kappera, R.; Voiry, D.; Yalcin, S. E.; Branch, B.; Gupta, G.; Mohite, A. D.; Chhowalla, M. Phase-engineered low-resistance contacts for ultrathin MoS_2 transistors. *Nature materials* **2014**, 13, 1128-1134.

82. Cho, S.; Kim, S.; Kim, J. H.; Zhao, J.; Seok, J.; Keum, D. H.; Yang, H. Phase patterning for ohmic homojunction contact in $MoTe_2$. *Science* **2015**, 349, 625-628.

83. Lin, Y. C.; Dumcenco, D. O.; Huang, Y. S.; Suenaga, K. Atomic mechanism of the semiconducting-to-metallic phase transition in single-layered MoS_2. *Nature nanotechnology* **2014**, 9, 391-396.

84. Huang, H. H.; Fan, X.; Singh, D. J.; Zheng, W. T. Recent progress of TMD nanomaterials: phase transitions and applications. *Nanoscale* **2020**, 12, 1247-1268.

85. Lin, Y. C.; Komsa, H. P.; Yeh, C. H.; Bjorkman, T.; Liang, Z. Y.; Ho, C. H.; Suenaga, K. Single-layer ReS_2: two-dimensional semiconductor with tunable in-plane anisotropy. *ACS nano* **2015**, 9, 11249-11257.

86. Coleman, L. B.; Cohen, M. J.; Sandman, D. J.; Yamagishi, F. G.; Garito, A. F.; Heeger, A. J. Superconducting fluctuations and the Peierls instability in an organic solid. *Solid state communications* **1973**, 12, 1125-1132.

87. Anderson, T. L. Fracture mechanics: fundamentals and applications. *CRC press* **2017**.

88. Parks, D. M. A stiffness derivative finite element technique for determination of crack tip stress intensity factors. *International journal of fracture* **1974**, 10, 487-502.

89. Yang, Y.; Li, X.; Wen, M.; Hacopian, E.; Chen, W.; Gong, Y.; Lou, J. Brittle fracture of 2D $MoSe_2$. *Advanced materials* **2017**, 29, 1604201.

90. Zhang, P.; Ma, L.; Fan, F.; Zeng, Z.; Peng, C.; Loya, P. E.; Lou, J. Fracture toughness of graphene. *Nature communications* **2014**, 5, 1-7.

91. Alava, M. J.; Nukala, P. K.; Zapperi, S. Statistical models of fracture. *Advances in physics* **2006**, 55, 349-476.

92. Bitzek, E.; Kermode, J. R.; Gumbsch, P. Atomistic aspects of fracture. *International journal of fracture* **2015**, 191, 13-30.

93. Cook, J.; Gordon, J. E. A mechanism for the control of crack propagation in all-brittle systems. Proceedings of the royal society of London. Series A. *Mathematical and physical sciences* **1964**, 282, 508-520.

94. Rice, J. R.; Thomson, R. Ductile versus brittle behaviour of crystals. *The philosophical magazine: a journal of theoretical experimental and applied physics* **1974**, 29, 73-97.

95. Hutchinson, J. W. Singular behaviour at the end of a tensile crack in a hardening material. *Journal of the mechanics and physics of solids* **1968**, 16, 13-31.

96. Abraham, F. F.; Brodbeck, D.; Rafey, R. A.; Rudge, W. E. Instability dynamics of fracture: a computer simulation investigation. *Physical review letters* **1994**, 73, 272.

97. Hauch, J. A.; Holland, D.; Marder, M. P.; Swinney, H. L. Dynamic fracture in single crystal silicon. *Physical review letters* **1999**, 82, 3823.

98. Zhang, Z.; Kutana, A.; Yakobson, B. I. Edge reconstruction-mediated graphene fracture. *Nanoscale* **2015**, 7, 2716-2722.

99. Terdalkar, S. S.; Huang, S.; Yuan, H., Rencis; J. J., Zhu, T.; Zhang, S. Nanoscale fracture in graphene. *Chemical physics letters* **2010**, 494, 218-222.

100. Clarke, D. R.; Faber, K. T. Fracture of ceramics and glasses. *Journal of physics and chemistry of solids* **1987**, 48, 1115-1157.

101. Lawn, B. R.; Hockey, B. J.; Wiederhorn, S. M. Atomically sharp cracks in brittle solids: an electron microscopy study. *Journal of materials science* **1980**, 15, 1207-1223.

102. Lawn, B. R.; Jakus, K.; Gonzalez, A. C. Sharp vs blunt crack hypotheses in the strength of glass: a critical study using indentation flaws. *Journal of the American ceramic society* **1985**, 68, 25-34.

103. Bando, Y.; Ito, S.; Tomozawa, M. Direct observation of crack tip geometry of SiO_2 glass by high-resolution electron microscopy. *Journal of the American ceramic society* **1984**, 67, C-36.

104. Tan, H.; Yang, W. Nonlinear motion of crack tip atoms during cleavage processes. *International journal of fracture* **1996**, 77, 199-212.

105. Griffith, A. A. VI. The phenomena of rupture and flow in solids. *Philosophical transactions of the royal society of london. Series A, containing papers of a mathematical or physical character* **1921**, 221, 163-198.

106. Irwin G. R.; Plastic zone near a crack and fracture toughness. *Sagamore research conference proceedings* **1961**, 4, 63-78.

107. Lee, C.; Wei, X.; Kysar, J. W.; Hone, J. Measurement of the elastic properties and intrinsic strength of monolayer graphene. *Science* **2008**, 321, 385-388.

108. Ly, T. H.; Zhao, J.; Cichocka, M. O.; Li, L. J.; Lee, Y. H. Dynamical observations on the crack tip zone and stress corrosion of two-dimensional MoS_2. *Nature communications* **2017**, 8, 1-7.

109. Wang, S.; Qin, Z.; Jung, G. S.; Martin-Martinez, F. J.; Zhang, K.; Buehler, M. J.; Warner, J. H. Atomically sharp crack tips in monolayer MoS_2 and their enhanced toughness by vacancy defects. *ACS nano* **2016**, 10, 9831-9839.

110. Zhang, P.; Ma, L.; Fan, F.; Zeng, Z.; Peng, C.; Loya, P. E.; Lou, J. Fracture toughness of graphene. *Nature communications* **2014**, 5, 1-7.

111. Swadener, J. G.; Baskes, M. I.; Nastasi, M. Molecular dynamics simulation of brittle fracture in silicon. *Physical review letters* **2002**, 89, 085503.

112. Holland, D.; Marder, M. Ideal brittle fracture of silicon studied with molecular dynamics. *Physical review letters* **1998**, 80, 746.

113. Khan, A. S.; Huang, S. Continuum theory of plasticity. **1995**. *John Wiley & Sons*.

114. Buehler, M. J.; Tang, H.; Van Duin, A. C.; Goddard III, W. A. Threshold crack speed controls dynamical fracture of silicon single crystals. *Physical review letters* **2007**, 99, 165502.

115. Chhowalla, M.; Shin, H. S.; Eda, G.; Li, L. J.; Loh, K. P.; Zhang, H. The chemistry of two-dimensional layered transition metal dichalcogenide nanosheets. *Nature chemistry* **2013**, 5, 263-275.

116. Wang, B.; Islam, Z.; Zhang, K.; Wang, K.; Robinson, J.; Haque, A. Role of sulphur atoms on stress relaxation and crack propagation in monolayer MoS_2. *Nanotechnology* **2017**, 28, 365703.

117. Cerda, E.; Ravi-Chandar, K.; Mahadevan, L. Thin films: wrinkling of an elastic sheet under tension. *Nature* **2002**, 419, 579-580.

118. Cerda, E.; Mahadevan, L. Geometry and physics of wrinkling. *Physical review letters* **2003**, 90, 074302.

119. Ly, T. H.; Zhao, J.; Cichocka, M. O.; Li, L. J.; Lee, Y. H. Dynamical observations on the crack tip zone and stress corrosion of two-dimensional MoS_2. *Nature communications* **2017**, 8, 1-7.

120. Rayleigh, L. *Theory of sound vol. 1*, **1945**, 396.

121. Luan, B.; Robbins, M. O. The breakdown of continuum models for mechanical contacts. *Nature* **2005**, 435, 929.

122. Zhu, W.; Low, T.; Perebeinos, V.; Bol, A. A.; Zhu, Y.; Yan, H.; Avouris, P. Structure and electronic transport in graphene wrinkles. *Nano letters* **2012**, 12, 3431-3436.

123. Xu, M.; Liang, T.; Shi, M.; Chen, H. Graphene-like two-dimensional materials. *Chemical reviews* **2013**, 5, 3766-3798.

124. Butler, S. Z.; Hollen, S. M.; Cao, L.; Cui, Y.; Gupta, J. A.; Gutiérrez, H. R. Progress, challenges, and opportunities in two-dimensional materials beyond graphene. *ACS nano* **2013**, 4, 2898-2926.

125. Novoselov, K. S.; Geim, A. K.; Morozov, S. V.; Jiang, D.; Zhang, Y.; Dubonos, S. V.; Firsov, A. A. Electric field effect in atomically thin carbon films. *Science* **2004**, 306, 666-669.

126. Novoselov, K. S.; Fal, V. I.; Colombo, L.; Gellert, P. R.; Schwab, M. G.; Kim, K. A roadmap for graphene. *Nature* **2012**, 490, 192-200.

127. Mak, K. F.; Lee, C.; Hone, J.; Shan, J.; Heinz, T. F. Atomically thin MoS_2: a new direct-gap semiconductor. *Physical review letters* **2010**, 105, 136805.

128. Seifert, G.; Terrones, H.; Terrones, M.; Jungnickel, G.; Frauenheim, T. Structure and electronic properties of MoS_2 nanotubes. *Physical review letters* **2000**, 85, 146.

129. Qin, L. C.; Zhao, X.; Hirahara, K.; Miyamoto, Y.; Ando, Y.; Iijima, S. Materials science: the smallest carbon nanotube. *Nature* **2000**, 408, 50.

130. Ortolani, L.; Cadelano, E.; Veronese, G. P.; Degli Esposti Boschi, C.; Snoeck, E.; Colombo, L.; Morandi, V. Folded graphene membranes: mapping curvature at the nanoscale. *Nano letters* **2012**, 12, 5207-5212.

131. Cranford, S. W.; Buehler, M. J. Packing efficiency and accessible surface area of crumpled gra-phene. *Physical review B* **2011**, 84, 205451.

132. Akinwande, D.; Brennan, C. J.; Bunch, J. S.; Egberts, P.; Felts, J. R.; Gao, H.; Liechti, K. M. A review on mechanics and mechanical properties of 2D materials—Graphene and beyond. *Extreme mechanics letters* **2017**, 13, 42-77.

133. Deng, S.; Berry, V. Wrinkled, rippled and crumpled graphene: an overview of formation mechanism, electronic properties, and applications. *Materials today* **2016**, 19, 197-212.

134. Hu, H. W.; Haider, G.; Liao, Y. M.; Roy, P. K.; Ravindranath, R.; Chang, H. T.; Chen, Y. F. Wrinkled 2D materials: a versatile platform for low-threshold stretchable random lasers. *Advanced materials* **2017**, 29, 1703549.

135. Park, S. M.; Huh, Y. S.; Craighead, H. G.; Erickson, D. A method for nanofluidic device prototyping using elastomeric collapse. *Proceedings of the national academy of sciences* **2009**, 106, 15549-15554.

136. Meng, L.; Su, Y.; Geng, D.; Yu, G.; Liu, Y.; Dou, R. F.; He, L. Hierarchy of graphene wrinkles induced by thermal strain engineering. *Applied physics letters* **2013**, 103, 251610.

137. Xu, P.; Neek-Amal, M.; Barber, S. D.; Schoelz, J. K.; Ackerman, M. L.; Thibado, P. M.; Peeters, F. M. Unusual ultra-low-frequency fluctuations in freestanding graphene. *Nature communications* **2014**, 5, 3720.

138. Meyer, J. C.; Geim, A. K.; Katsnelson, M. I.; Novoselov, K. S.; Booth, T. J.; Roth, S. The structure of suspended graphene sheets. *Nature* **2007**, 446, 60–63.

139. Pereira, V. M.; Neto, A. C.; Liang, H. Y.; Mahadevan, L. Geometry, mechanics, and electronics of singular structures and wrinkles in graphene. *Physical review letters* **2010**, 105, 156603.

140. Wei, Y.; Wang, B.; Wu, J.; Yang, R.; Dunn, M. L. Bending rigidity and Gaussian bending stiffness of single-layered graphene. *Nano letters* **2012**, 13, 26-30.

141. Lee, C.; Wei, X.; Kysar, J. W.; Hone, J. Measurement of the elastic properties and intrinsic strength of monolayer graphene. *Science* **2008**, 321, 385-388.

142. Williams, D. B.; Carter, C. B. The transmission electron microscope. *In transmission electron microscopy* **1996**. Springer, Boston, MA.

143. Jeon, J.; Jang, S. K.; Jeon, S. M.; Yoo, G.; Jang, Y. H.; Park, J. H.; Lee, S. Layer-controlled CVD growth of large-area two-dimensional MoS_2 films. *Nanoscale* **2015**, 7, 1688-1695.

144. Mendes, R. G.; Pang, J.; Bachmatiuk, A.; Ta, H. Q.; Zhao, L.; Gemming, T.; Rümmeli, M. H. Electron-driven in situ transmission electron microscopy of 2D transition metal dichalcogenides and their 2D heterostructures. *ACS nano* **2019**, 13, 978-995.

145. Zhu, Y.; Li, Y.; Arefe, G.; Burke, R. A.; Tan, C.; Hao, Y.; Hone, J. C. Monolayer molybdenum disulfide transistors with single-atom-thick gates. *Nano letters* **2018**, 18, 3807-3813.

146. Gao, J.; Kim, Y. D.; Liang, L.; Idrobo, J. C.; Chow, P.; Tan, J.; Koratkar, N. Transition-metal substitution doping in synthetic atomically thin semiconductors. *Advanced materials* **2016**, 28, 9735-9743.

147. Lin, J.; Cretu, O.; Zhou, W.; Suenaga, K.; Prasai, D.; Bolotin, K. I.; Pantelides, S. T. Flexible metallic nanowires with self-adaptive contacts to semiconducting transition-metal dichalcogenide monolayers. *Nature nanotechnology* **2014**, 9, 436-442.

148. Sang, X.; Li, X.; Zhao, W.; Dong, J.; Rouleau, C. M.; Geohegan, D. B.; Unocic, R. R. In situ edge engineering in two-dimensional transition metal dichalcogenides. *Nature communications* **2018**, 9, 1-7.

149. Lin, Y. C.; Dumcenco, D. O.; Huang, Y. S.; Suenaga, K. Atomic mechanism of the semiconducting-to-metallic phase transition in single-layered MoS_2. *Nature nanotechnology* **2014**, 9, 391-396.

Chapter 2 Grain Boundaries and Their Mobility in 2D ReS_2

2.1 Introduction

As is well known, 2D ReS_2 has monoclinic atomic structure (Figure 2.1). The six S atoms are bonded with the central Re atom in distorted tetragonal (T′) coordination.[1] In line with the enhanced atomic dynamics on surfaces, the facile atomic reconstructions (including the Re diamond-chain zipping/unzipping) in 2D ReS_2 have been observed.[2] In this connection, the

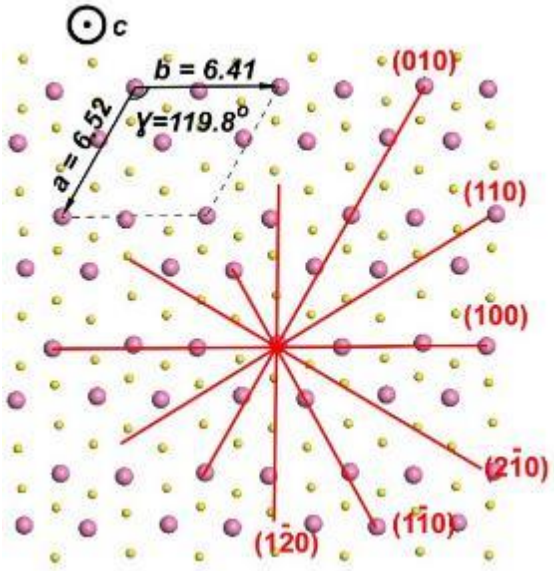

Figure 2.1 Schematic diagram of monoclinic atomic structure of 2D ReS_2, six low-index planes are highlighted.

twinning and twin boundaries (TBs) can be rendered by the lattice orientation switching in 2D ReS_2. Basically, like the standard mechanical TBs, the TBs here can be nucleated and driven by mechanical straining in 2D ReS_2. Here we classify all the GBs in ReS_2 into four subgroups, by high/low-index and coherent/incoherent, respectively (Figure 2.2). The low/high-index refers to the Miller Index for the GB planes (also used for the name of GBs below, see Figure 2.1) for the six low-index planes in ReS_2. The six low-index planes in ReS_2 include (010), (100), (110), (2-10), (1-10) and (1-20). High-index usually refers to the vicinal planes of the low-index planes. Coherency of GB is determined by the periods of both side of crystals at the GB planes, while coherent GB means a perfect matching and no interfacial strain.

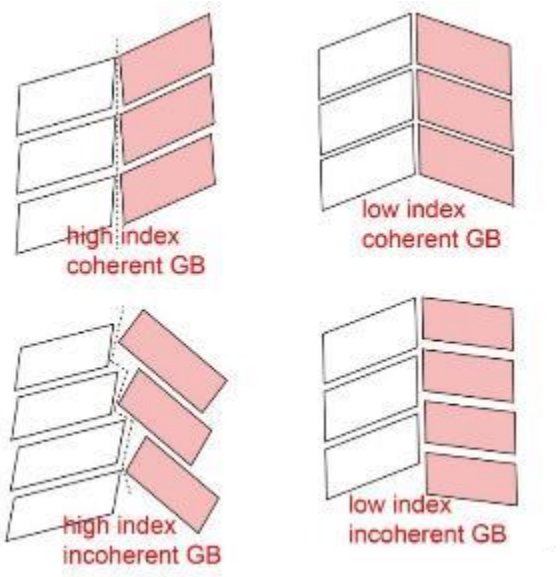

Figure 2.2 Schematic diagram of 4 groups of GBs in ReS_2, divided by miller index and coherence at GBs.

2.2 Method and Experiments

2.2.1 Sample Growth and Transition

2D 1L ReS_2 was grown by method of atmospheric CVD on a c-face sapphire substrate with a size of 1cm×1cm. The precursor for the two quartz boats were Ammonium perrhenate (NH4ReO4) (Aldrich, 99.999 %) and Sulfur powder (Aldrich, 99.998 %), with 1:50 of the weight ratio. The temperature of sulfur and substrate were precisely controlled by a two-zone splitting tube furnace. Argon gas was used carrier gas to deliver the sulfur vapor to substrate during deposition process. The sulfur zone rose to 200 ° C, while the substrate area reached 850 ° C within 30 minutes, and then was held for 10 minutes.

Through the well-known poly (methyl methacrylate) (PMMA)-assisted technology, CVD-grown ReS_2 was transferred to the TEM grid. Using spin coating, a thin layer of PMMA formed on the grown sapphire substrate at 3000 rpm for 50 seconds. Supported by PMMA, 1L ReS_2 was immersed in deionized water at 75°C for two hours and fell off the substrate. The PMMA/ReS_2 layer was then transferred to a Quantifoil TEM grid and dried at ambient temperature. In the end, the PMMA film was gently removed by acetone vapor.

2.2.2 (S)TEM Characterizations and Free Edge

The STEM JEM-ARM200F with aberration correction at an acceleration voltage of 60 kV was used which equipped with a CEOS spherical (Cs) aberration corrector. The vacuum during the

measurement was kept at 1.3×10^{-7} mbar, and the electron beam current was 13 μA. The size of the scanning probe is *ca*. 1.5 Å. For image acquisition, the camera length on STEM was 120 mm. With a defocus of -4 nm, the acquisition time of HAADF images is 19 μs per pixel to minimize damage and obtain graphics with lower drift. Images of 512 × 512 size pixels is obtained with a CL aperture of 40 μm, and the collection angle ranged from 45 to 180 mrad, to make atomic images with appropriate contrast be obtained. Wiener filtering was applied to HAADF images to reduce noise.

Exposing 2D ReS_2 under the ultra-high beam intensity more than 0.3 pA/nm^2 for 15 to 30 minutes can create controlled circle area with diameter about 100 nm to generate cracks on the sample. After that, microscope was quickly changed into STEM mode and the in-situ experiment started when the sample being exposed under electron beam. Due to the crack dynamics outside the exposed area of the beam, the length of these newly generated crack edges extended. Under the in-plane mechanical loading, the shear stress caused the lattice reconstruction in 1L-ReS_2. With the *in situ* STEM serial capture (time interval 13-20s), the GB dynamics under shear stress can be recorded.

2.2.3 Density Functional Theory Calculations

The first-principles calculations are performed with spin-unrestricted manner by using the Vienna ab initio Simulation Package (VASP) program package[3,4] within the projector augmented wave (PAW)[5] to explore geometries and electronic properties of ReS_2. The exchange-correlation interactions are described with the generalized gradient approximation

(GGA)[6] in the form of the Perdew, Burke, and Ernzernhof (PBE) functional[7]. This kinetic energy cut-off of 450 eV is utilized in all calculations, and the distance of vacuum layer is set to be more than 20 Å, which is sufficiently large to avoid interlayer interactions. The electronic SCF tolerance is set to 10^{-4} eV. Fully relaxed geometries and lattice constant are obtained by optimizing all atomic positions until the Hellmann–Feynman forces are less than 0.02 eV/Å. The k-points samplings with a gamma-centred Monkhorst-Pack scheme[8] are 3×5×1 and 5×9×1 for structural optimizations and electronic properties, respectively .

2.3 Results and Discussions

2.3.1 Dynamics of Grain Boundaries in ReS_2

GBs present in 2D 1L-ReS_2 samples grown by CVD (see Methods) can be originated from two different mechanisms, *viz.*, by direct growth and mechanical strain (Figure 2.3a, b). The flake stitching is quite similar to other 2D materials, but the deformation twining in 2D ReS_2

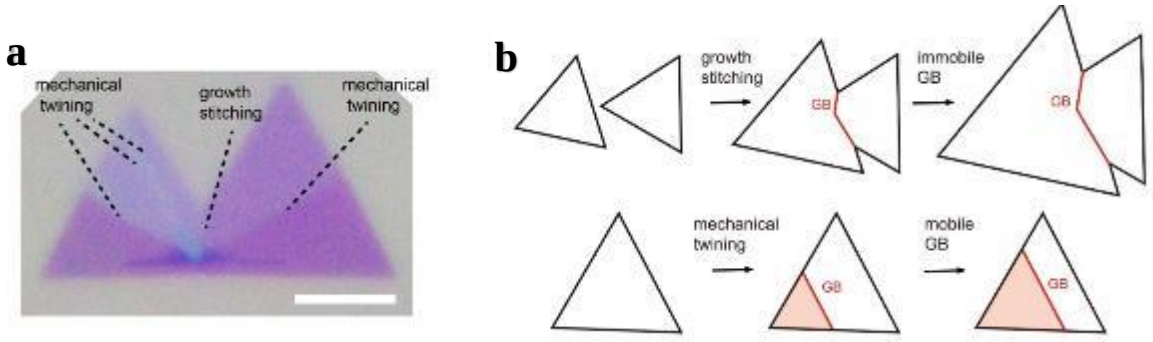

Figure 2.3 (a) Polarized OM image showing grains and GBs in 1L-ReS2 samples from CVD growth, the scale bar is 5µm. (b) Two GB formation mechanisms.

is unique. It should also be noted that the lattices for sulfur (S) atoms may have two types, named as type I and II, which are in mirror symmetry (Figure 2.4a). Blue arrows indicate the S atom movement during transition between I and II. Yellow arrows indicate the easy Re atom movement when the S lattice (either I or II) does not switch. Mechanical loading can reconstruct the lattices of Re atoms (following yellow arrow direction) without transformation

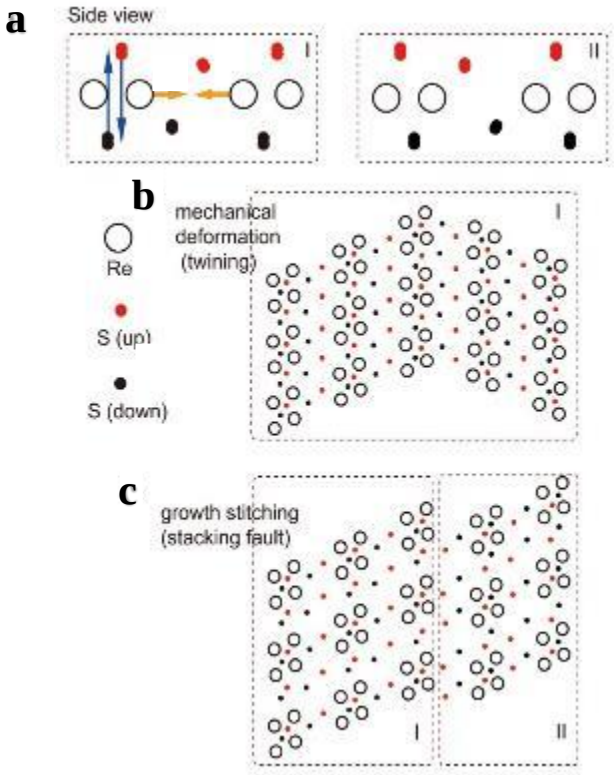

Figure 2.4 (a) Side view arrangements of two mirrored S arrangement (I and II) in 1L-ReS_2, S atoms (upper (red) and lower (black) S atoms with respective to Re atomic plane) and Re atoms (black hollow circles) are shown. (b) Plane-view of mobile boundaries (by mechanical loading) in 1L ReS_2, consisting a single type S atom arrangement (either I or II). (c) The stacking fault (SF) GB consisting of two grains with different (I and II) S arrangements, pinned by S lattices.

of the S lattices (following blue arrow direction) between type I and II, explainable by the fact that rearrangement of S atoms needs to cross the basal plane, while Re atomic rearrangement

not (Figure 2.4a). Thus, the mechanical twinning (Figure 2.4b) should possess pure I or II type S lattice in both side crystals, while the growth stitching (Figure 2.4c), especially the stacking fault (SF) GB as we will introduce below, possess the mixed I/II type S lattices, in another word, they can be pinned by the S lattices.

2.3.2 Library of Grain Boundaries in ReS_2

In our experiments, the as-grown 1L ReS_2 were transferred onto TEM grid by PMMA method,[9] and then characterized by the probe aberration-corrected scanning STEM at the atomic scale (see Methods). All the ReS_2 GB atomic structures have been simulated by DFT method and directly matched with the experimental STEM-annular dark field (ADF) images. First, we take look at the coherent GBs (mainly twin GBs) with the least mismatch and internal strain. The coherent twin GBs can be sub-divided into high-index coherent GB (misorientation angle 0^o-30^o) (Figure 2.5a, b) and low-index coherent GB (Figure 2.5c-i). The former is usually constructed by 2D flake stitching during growth, and they consist of periodic dislocations, resembling ordinary LA GBs. In contrast, the latter (Figure 2.5c-h, except for the SF GB) is able to be formed by strain induced lattice reconstruction (twinning). The slightly distorted tetragonal structure in 2D ReS_2 renders six types of low-index TBs. Upon relaxation, the corresponding lattice shear angles for the twinning grains with respective to the original grains range from 1-3^o, Figure 2.5j shows the ultrasmall shear angle (2.5^o) for lattices (the red (100) plane and dashed blue (010) plane) over the two sides of (1-10) TB. Hence low mechanical

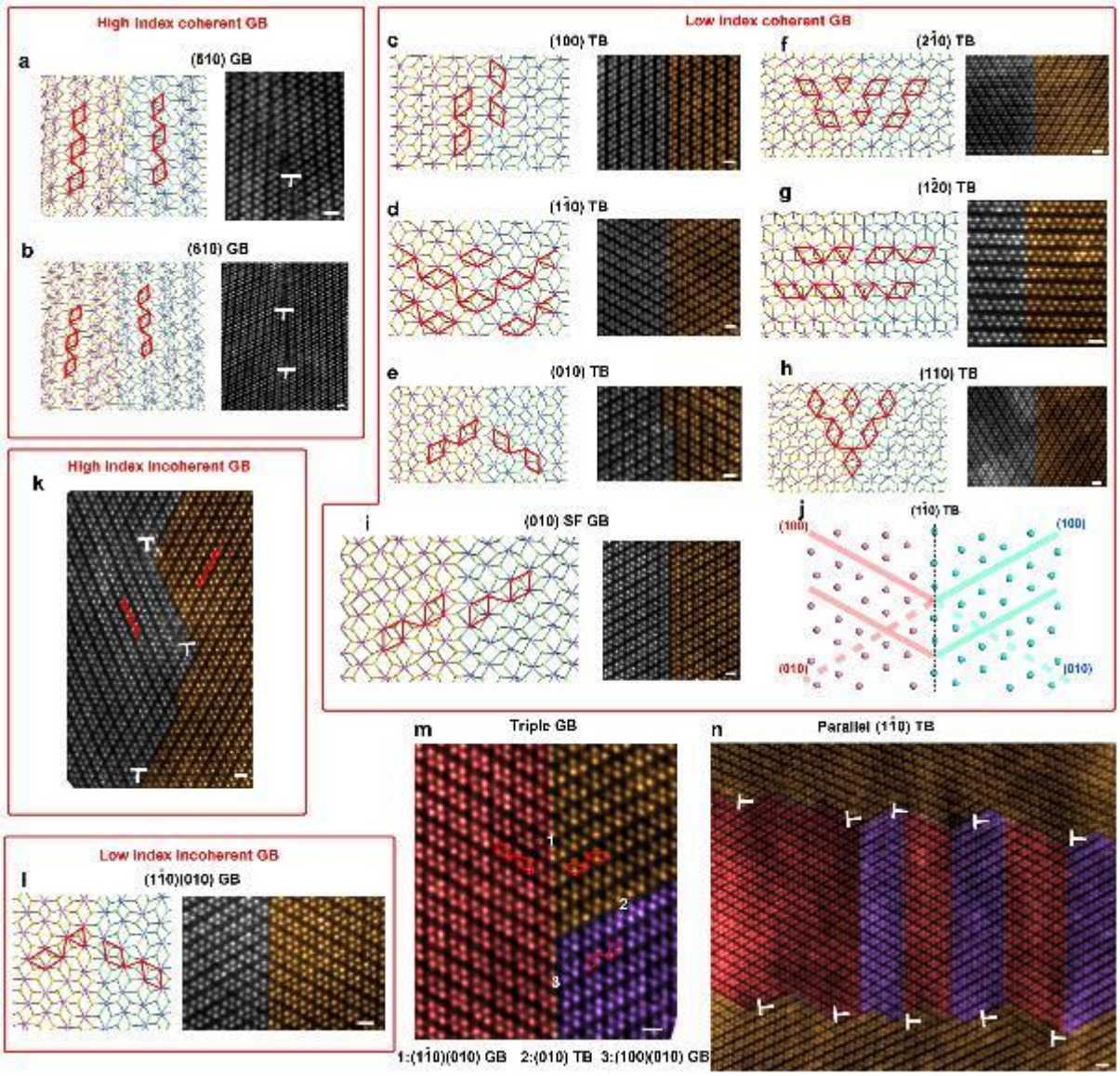

Figure 2.5 A Library of GBs in 1L ReS_2: DFT calculated atomic models (left) and STEM-ADF images (right). (a, b) High index coherent GBs:(510), (610) lattice plane at GBs. Two side crystals of GBs are colored differently. Re diamond chains and dislocations are highlighted by red and white signs. (c-h) Low-index coherent Twinning Boundary (TB). (i) Stacking fault (SF) GB, belonging to low-index coherent GB. (j) Scheme for lattice distortion crossing TBs. (k) Non-straight high-index incoherent GB. (l) One example for low-index incoherent GB. (m) A triple GB with three GBs crossing together. Specific GB types are indicated below by numbers. (n) STEM figure parallel TBs encapsulated by piled up dislocations. Scale bar of STEM figures is 0.5 nm in all figures.

stress is anticipated to enable the twining. If the orientation of TBs is in between the orientations of the above six types (i.e., following higher index planes), the TBs can be decomposed into short sections of low-index TBs possibly separated by dislocations.

Interestingly, the twinning (lattice reconstruction) process in 2D ReS_2 involves a synergistic bonding rearrangement between Re and S atoms. If we focus on the positions of S atoms, actually three types of TBs (Figure 2.5f-h) are exact twinning GBs for both Re and S lattice positions, while the other three types (Figure 2.5c-e) are TBs for only Re lattice positions, and inverse twin GBs for S lattice positions (Figure 2.4b). It is originated from the lack of inverse symmetry (with respect to *c* axis) in 1L ReS_2. As we said, the S lattices are less likely to change the symmetry parity (switch between I and II types) under mechanical loading. This gives rise to a kind of special stacking fault (SF) GB in 1L ReS_2 (Figure 2.4c, Figure 2.5i). Both grains beside such GBs have the same orientation in terms of Re lattices, nevertheless, not in the S lattices. Therefore, the stitching of such edges during growth is prone to produce a SF GB. If both the Re and S lattices are exactly same oriented, perfect stitching with no GBs will occur. In this instance, such SF GBs are not originated by mechanical loading.

Compared to the coherent GBs in 2D ReS_2, incoherent GBs have much higher misfit strain at the GBs. The typical incoherent high angle (HA) (30^o-180^o) GBs (namely incoherent high-index GB) in 2D ReS_2 are shown in Figure 2.5k. The incoherent high-index GBs can be considered as the combination of coherent high-index GBs and incoherent (or coherent) low-

index GBs. In addition to the dislocations as seen in the coherent high-index GBs, the greater lattice mismatches can bend the original straight GBs, decomposing them into zigzag low-index GB sections separated by dislocations, and they are usually generated by growth stitching similar to the coherent high-index GBs. Although the formation energies of the incoherent high-index GBs are higher than coherent high-index GBs, due to the inevitable high angle stitching during growth occasionally, these incoherent GBs can be widely found in CVD-grown samples.

Conversely, the incoherent low-index GBs (Figure 2.5l) are usually observed in bended GBs or complex strain zones, e.g., the triple GB cross (Figure 2.5m). The interfacial lattice misfit strains on the incoherent low-index GBs are hence partially compensated by the circumferential strain relaxation factors, lowering the energy cost for the incoherent GBs. The incoherent low-index GBs can also be pinned at defects, but in general, because the lattice mismatch at these incoherent low-index GBs are quite low (1-2%) and the formation energies are relatively low, they are mobile and freely interact with the aforementioned coherent TBs.

Due to the intrinsic lattice shearing at TBs and lattice mismatch at the incoherent low-index GBs, they inherently tend to be pinned by the dislocations, more precisely, by the strain field of dislocations. One example can be found in Figure 2.5n, the parallel TBs are distributed between perpendicular LA GBs, nucleated and located at the dislocation cores. Overall, the GBs in monoclinic 2D ReS_2 are summarized in Table 2.1. The DFT calculations show the

predominantly lower formation energies for coherent GBs, particularly the low-index TBs. The SF GB has significantly higher energy because of S lattice mismatch.

Classifications	**Name**	**Formation energy (DFT) (eV/nm)**	**Origin**	**Kinetics**
Coherent high-index GB		Medium	Growth	Pinned by dislocations
Coherent Low-index GB	(100) TB	0.20	Mechanical twinning	Mobile
	(1-10) TB	1.16		
	(010) TB	1.75		
	(2-10) TB	2.02		
	(1-20) TB	1.37		
	(110) TB	1.12		
	SF TB	4.82	Growth	Pinned by S lattice
Incoherent high-index GB		High	Growth	Pinned by dislocations
Incoherent Low-index GB	(1-10) (010) GB	1.88	Mechanical	Mobile

Table 2.1 Summary and classification of all GBs in 1L ReS_2.

2.3.3 Stress and Displacement in Grain Boundaries

As we mentioned, the shear stress is responsible for the twining nucleation and TB movement (Figure 2.6a,b), and normally the energy cost for twinning nucleation are much higher than TB

movement.[10] According to the Peierls framework for twinning,[11] the critical stress for twinning can be estimated by

$$\tau(pristine - twinned) = \frac{\Psi(twinned) - \Psi(pri)}{\Delta x(twinned) - \Delta x(pri)}$$

Where τ is the shear stress along the slip planes, Δx is the share displacement of central pair of planes, Ψ is the energy of sheared configurations. The relationship of stress and energy is an integral in Peierls concepts which turns to linear during the calculation between two different orientations. Using the DFT obtained energies and lattice distortions, the critical twinning stresses in 2D ReS_2 are estimated between 4-30 MPa. These values are much lower than the conventional twinning stresses for metals or inorganic bulks (Figure 2.6c),[12] in line with the high-frequency twinning in 2D ReS_2 as we have observed.

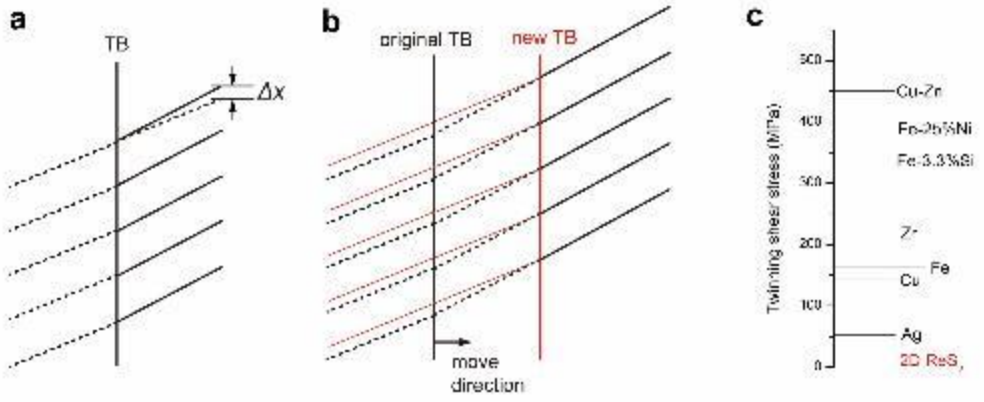

Figure 2.6. Mechanically induced TBs in 1L ReS_2 (a) Schematic of displacement (Δx) of the twining nucleation under share stress. (b) TB movement under shear stress. (c) Comparison of twinning shear stress in 2D ReS_2 with other metals and inorganic materials (data in part adapted from ref [12]).

By using *in situ* STEM technique, the mobile GBs have been real-time observed, which nucleated and moved close to the free edges of 2D ReS_2 (Figure 2.7a-c). During our *in situ* observations, the TBs and incoherent low-index GBs ((1-10) (010) GB) can freely move under the impact of external straining (by electron beam effect on the peripheral areas). No apparent defects or dislocations were generated inside the area of interest (the observation area shown in Figure 2.7a-c). However, in another case (Figure 2.7d-e), an incoherent (1-10) (010) GB was observed to be pinned by series of dislocations (each dislocation was covered by the bright hydrocarbon originated from residual particles during sample growth). Therefore, the kinetics of the group of coherent or incoherent low index GBs are highly dependent on the environment close to the GBs. Due to the lattice mismatch, long incoherent GBs tend to be pinned by (partial) dislocations, while the short incoherent GBs, especially low-index GBs are highly mobile and can actively participate in the lattice reconstructions in 2D ReS_2 under external mechanical loading. More examples on defects (dislocation) pinning can be found in supporting information Figure 2.8.

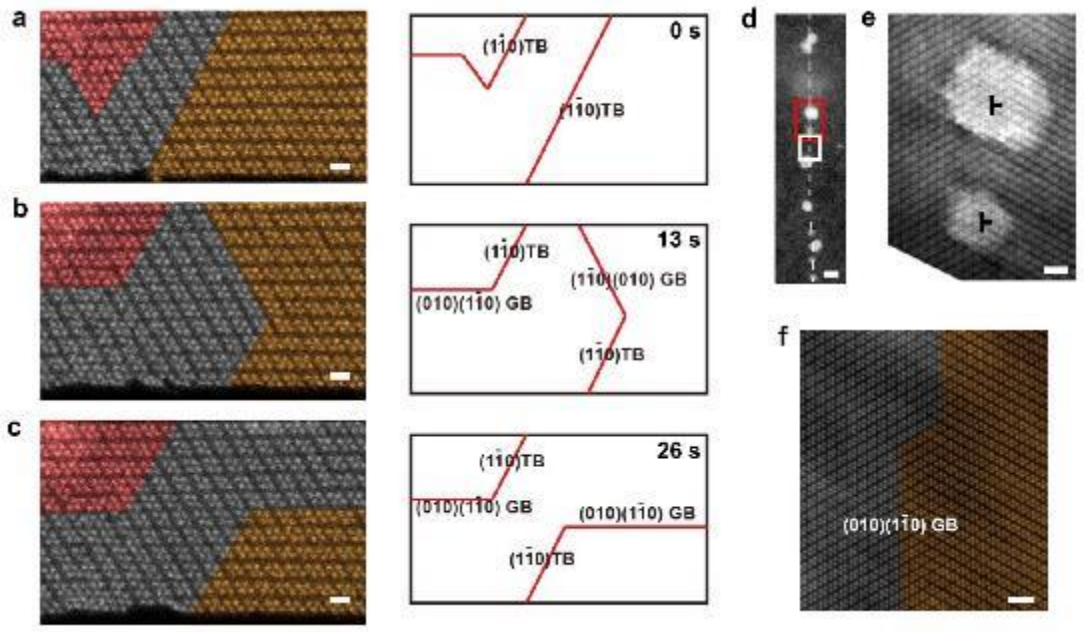

Figure 2.7 *In situ* STEM observations on the kinetics of GBs in 1L ReS_2. (a-c) A serial *in situ* STEM-ADF atomic scale observation on the mobile GBs next to the free edge of 2D ReS_2 during 26 s. Scale bars: 0.5 nm. Right panels highlight the mobile GBs correspondingly. (d-f) The dislocation pinned incoherent low-index GB. (e) and (f) are magnified images for red and white rectangles, respectively. Scale bars in (d): 3.5 nm, (e, f):1 nm.

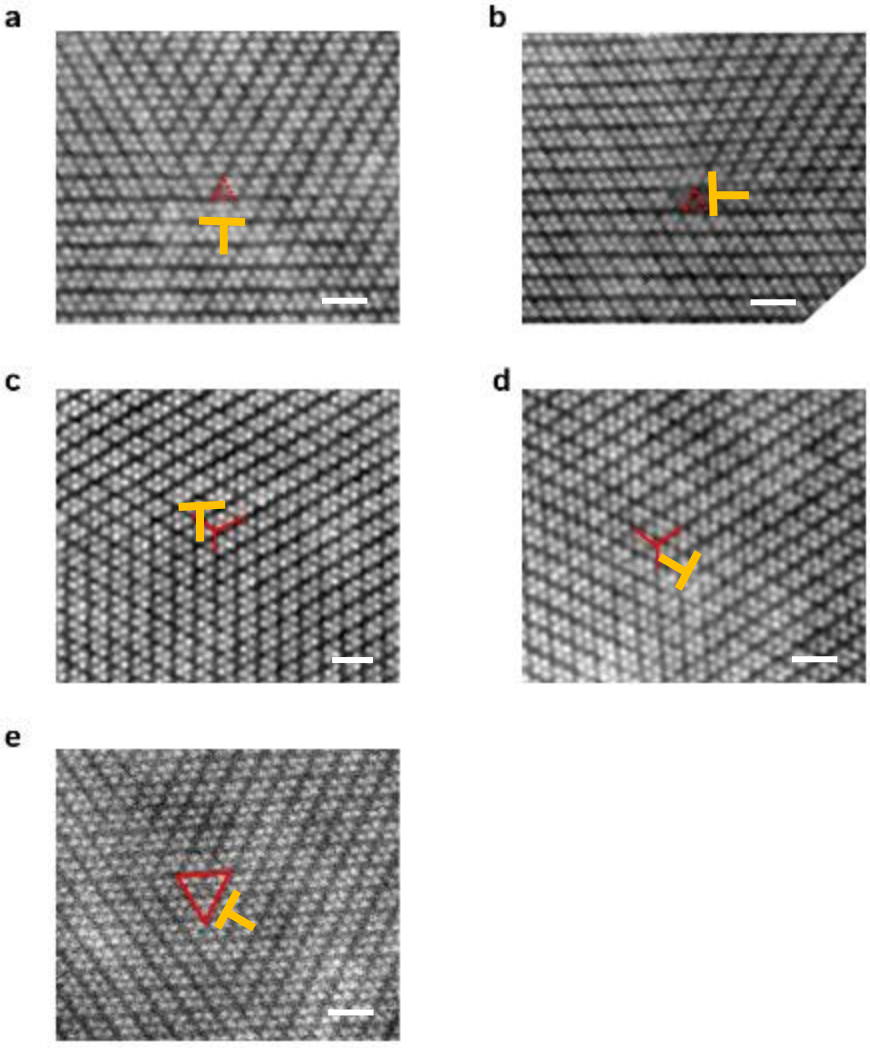

Figure 2.8 STEM-ADF images for pinned GBs by defects. The centered dislocations are marked by yellow signs. Scale bars = 1nm.

Disregarding the surface (edge) effect, all of the straight GBs inside the 2D ReS_2, irrespective of the GB types, are dynamically stable. Kinetics of GBs will be either triggered by the reduction of local curvatures in GBs (driven by GB tensions), or by the external mechanical stresses. Furthermore, these mobile GBs can be pinned by the relatively immobile dislocations, which is opposite to the cases in traditional metals. Usually in bulk metals, the dislocation

dynamics (slip) are slowed down by the relatively immobile GBs or TBs.[13] Therefore, the introducing of GBs or TBs intentionally can be utilized for material strengthening. However, in 2D ReS_2 the inversed sequence for twinning (or lattice reconstruction which produce the incoherent low-index GBs) and the dislocation slip under mechanical deformation have eventually led to the abnormal defect dynamics as we observed.

2.3.4. Density Functional Theory Calculation of Grain Boundaries

We have further investigated the electronic structures by spin-polarized DFT calculations for the coherent low-index, coherent high-index and incoherent-low index GBs, respectively (Figure 2.9). The band structures and the magnetic moments vary widely within different types of GBs. Some GBs have very prominent deep levels, like the (110) TB. While some do not have mid-gap states, like the (100) TB. The deep levels are the keys to the electrical transport control. While the bandgaps also vary from 1.3 to 1.8 eV. Interestingly, three kinds of TBs and the misfit incoherent low index GBs have very large magnetic moments, suggesting the opportunities in magnetic property modulations using mechanical approaches.

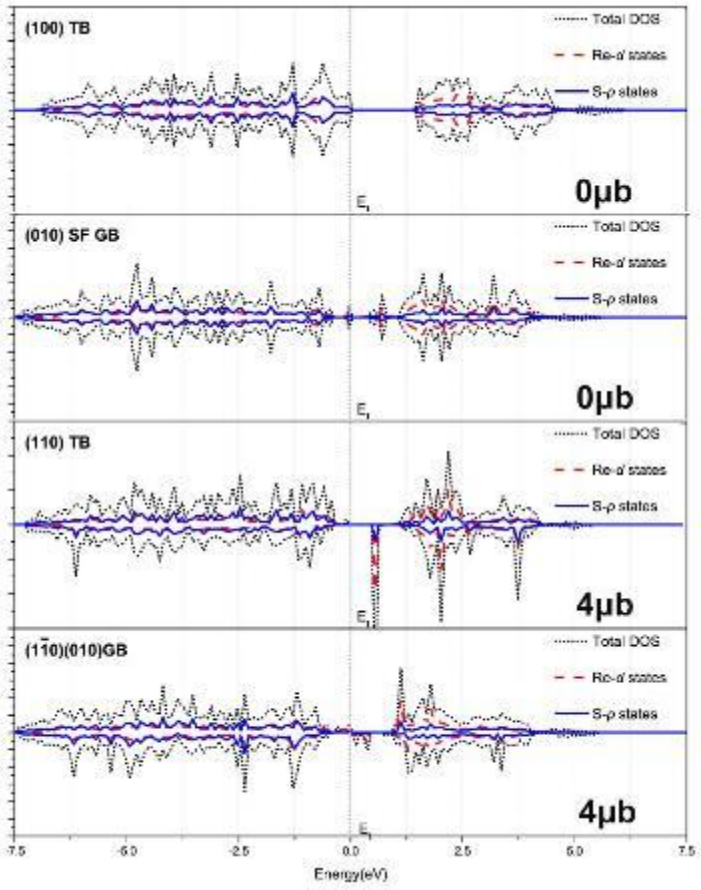

Figure 2.9 The Spin-polarized density of states (DOS) calculated by the DFT for various GBs. DOS (black dot line) and local DOS projected on 5d (red dash line) states of Re as well as 3p of S (blue line) of ReS_2. The Fermi level is set to zero. Calculated magnetic moments are marked in lower-right.

2.3.5 Summary

In conclusion, we have established a complete library for the GBs in monoclinic 2D ReS_2 and rationalized the kinetics of GBs. Different from the immobile GBs in high-symmetric 2D materials previously, the GBs in 2D ReS_2 can be formed by either bottom-up growth or mechanical loading, and the notable kinetics of GBs are also dependent on the GB types. In

particular, the dislocations as well as S lattices can pin the GBs. In this connection, the material properties (e.g., electrical, optical and mechanical properties) will not only be passively impacted by the GBs, in return, the GBs in 2D ReS_2 can be controlled by exterior straining, thereby extending rich possibilities for strain engineering on the electrical, electronic and magnetic properties in such 2D monoclinic materials.

References

1. Liu, Y.; Zhao, J.; Li, Z.; Mu, C.; Ma, W.; Hu, H.; Yan, H. Aggregation and morphology control enables multiple cases of high-efficiency polymer solar cells. *Nature communications* **2014**, 5, 1-8.

2. Lin, Y. C.; Komsa, H. P.; Yeh, C. H.; Bjorkman, T.; Liang, Z. Y.; Ho, C. H.; Suenaga, K. Single-layer ReS_2: two-dimensional semiconductor with tunable in-plane anisotropy. *ACS nano* **2015**, 9, 11249-11257.

3. Kresse, G.; Furthmüller, J. Efficient iterative schemes for ab initio total-energy calculations using a plane-wave basis set. *Physical review B* **1996**, 54, 11169.

4. Kresse, G.; Furthmüller, J. Efficiency of ab-initio total energy calculations for metals and semiconductors using a plane-wave basis set. *Computational materials science* **1996**, 6, 15-50.

5. Blöchl, P. E. Projector augmented-wave method. *Physical review B* **1994**, 50, 17953.

6. Perdew, J. P.; Burke, K.; Ernzerhof, M. Generalized gradient approximation made simple. *Physical review letters* **1996**, 77, 3865.

7. Perdew, J. P.; Ernzerhof, M.; Burke, K. Rationale for mixing exact exchange with density functional approximations. *The Journal of chemical physics* **1996**, 105, 9982-9985.

8. Monkhorst, H. J.; Pack, J. D. Special points for Brillouin-zone integrations. *Physical review B* **1976**, 13, 5188.

9. Najmaei, S.; Liu, Z.; Zhou, W.; Zou, X.; Shi, G.; Lei, S.; Lou, J. Vapour phase growth and grain boundary structure of molybdenum disulphide atomic layers. *Nature materials* **2013**, 12, 754-759.

10. Meyers, M. A.; Vöhringer, O.; Lubarda, V. A. The onset of twinning in metals: a constitutive description. *Acta materialia* **2001**, 49, 4025-4039.

11. Rice, J. R. Dislocation nucleation from a crack tip: an analysis based on the Peierls concept. *Journal of the mechanics and physics of solids* **1992**, 40, 239-271.

12. Kibey, S.; Liu, J. B.; Johnson, D. D.; Sehitoglu, H. Predicting twinning stress in fcc metals: Linking twin-energy pathways to twin nucleation. *Acta materialia* **2007**, 55, 6843-6851.

13. Lu, L.; Chen, X.; Huang, X.; Lu, K. Revealing the maximum strength in nanotwinned copper. *Science* **2009**, 323, 607-610.

Chapter 3 Phase Transition on 2D ReS_2

3.1 Introduction

From experiments and calculations, suppression of Re ion dimerization along either *a* or *b* direction or along both *a* and *b* directions can be enabled, leading to T′ (space group: P21/m) or T (space group: P-3m1) phases, respectively. From DFT results (Figure 3.1), T and T′ phases are stabilized by compressive strain in the 2D layers with selective removal of S atoms. Thus the atomic phase patterning can be achieved by controlling electron beam irradiation. For experiment, *in situ* TEM-STM study reveals the superior conductivity in T/T′ phases, which

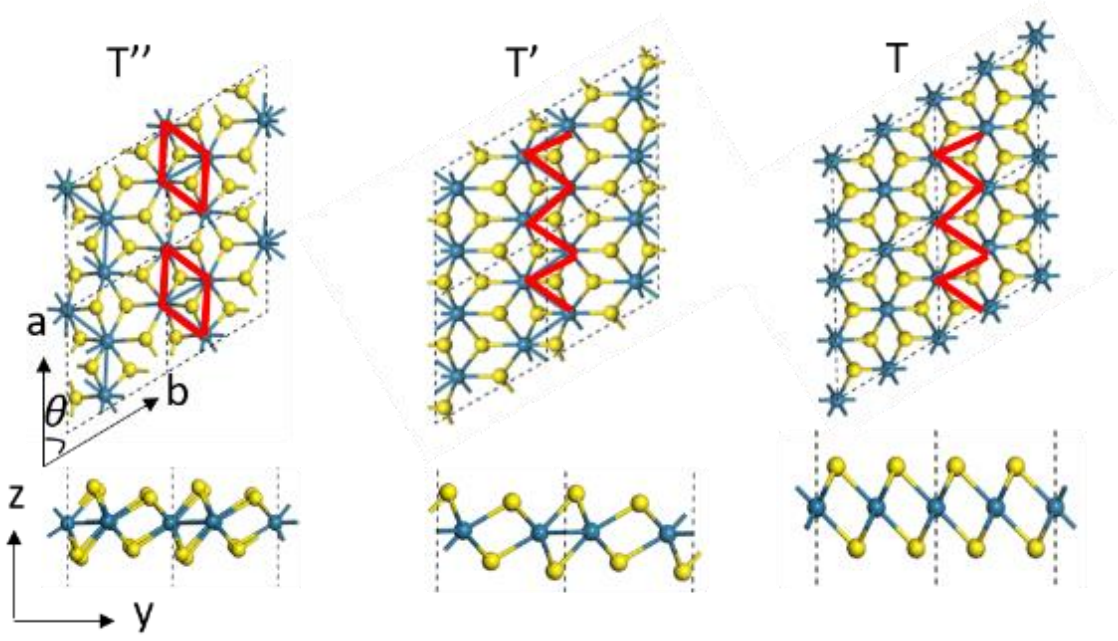

Figure 3.1 Calculated structure of ReS_2 in T'' phase, T' phase and T phase, separately.

means the metallic wires/pads can be directly written in the insulating/semiconductive T″ phase. DFT calculation shows the atomic structure of three possible phases in ReS_2 in total including a newly discovered phase of ReS_2, which is T phase as shown in Figure 3.1. T″ phase is formed by 2*2 unit cells with only inversion symmetry, which makes the structure anisotropic. T′ has a higher symmetry which can be distinguished from the 1*2 basic lattice cell, however, the calculation shows it is a dynamically unstable phase which usually transform very easily. T phase from calculation has the highest symmetry which consists of 1*1 supercell comparing with another two phases, but it hasn't been observed or studied either experimentally or theoretically.

3.2 Method and Experiments

3.2.1 Sample Synthesis and Specimen Preparation

Monolayer ReS_2 was grown on a polished c-face sapphire substrate by CVD method under atmospheric pressure. Sulfur powder (Aldrich, 99.998 %) was put in the upstream zone while ammonium perrhenate (NH_4ReO_4) (Aldrich, 99.999 %) was put in the downstream zone as precursors, with a weight ratio of 1: 50 in a two-zone splitting tube furnace. The polished side of c-face sapphire substrate was towards the top of Re source and the size was 1 cm × 1 cm. To purify the gas atmosphere of tube before heating, 300 standard cubic centimeter per minute (sccm) Argon (Ar) gas was purged for 10 minutes. Then the upstream and downstream zones were heated up at the same time to 200° and 850°C separately in 30 minutes and hold for 10 minutes. The atmosphere during the whole heating process was 80 sccm Ar. 1L ReS_2 grown

in this process is triclinic and highly anisotropic, corresponding to the typical tetragonal (T) phase in TMDs with slightly distorted “diamond”-type superlattices in two directions (***a*** and ***b***).

The CVD-grown ReS_2 was transferred on a TEM grid by PMMA-assisted method. Under the rotate speed of 3000 revolutions per minute for 50 s, the c-face sapphire substrate was covered by a thin layer of PMMA by spin coating. After being immersed in 75°C deionized water for 2 hours, the monolayer ReS_2 detached from the substrate and transferred onto a TEM grid. Then the grid was dried up at ambient temperature, PMMA residue was removed by acetone as the last step.

3.2.2 (S)TEM Characterizations and *In Situ* Phase Transition

A JEM-ARM200F TEM was operated with a 60 kV accelerating voltage on monolayer ReS_2 to avoid the beam damage. The TEM was retrofitted with a Corrected Electron Optical Systems (CEOS) probe spherical (Cs) aberration corrector for atomic resolution in STEM mode. The electron beam current was around 13.5 μA and the vacuum was kept around 1.3×10^{-7} mbar. During the record of the high-angle annular dark field (HAADF) images, a 1.5 Å beam size and 120 mm camera length was applied on STEM. The acquisition time of HAADF images was 19 μs per pixel with images formed by 512 × 512 size pixels. Defocus was adjusted to -4nm, the CL aperture during image capture was 40 μm and the collection angle was 45 to 180

mrad, to obtain the continuous atomic images with high resolution and proper contrast. Wiener filtering was applied on HAADF images for reduction of noises.

Under the ultrahigh beam intensity 0.3 pA nm^{-2}, the continuous STEM electron beam scanning can easily trigger the S defects in the exposed area without generating large Re defects in 2-3 minutes. S defects provides in-plane mechanical loading with proper shear stress for ReS_2 to transform from T″ phase to T′/T phase. Real-time movement of atoms can be recorded by the *in situ* STEM serial capture (13-20s each frame) for phase and strain analysis.

3.2.3 TEM-STM on Conductivity Measurement

A Nanofactory *in situ* STM-TEM holder with JEOL 2100F TEM under 200keV accelerating voltage were applied for phase transition in TEM mode, the beam intensity was 7.5 pA nm^{-2} to avoid damage on the sample and create transformation to T′/T phase. Keithley 2400 with a LabVIEW program was used for I-V data collection. Using electrochemical corrosion under a solution of 1 mol/L NaOH at a 6 V bias, W tips can be made with a few nanometers of diameter on the top. The tip was further cleaned by ethanol and deionized water. Connected with Nanofactory holder, piezoelectric-driven fine control drove W tips move precisely in 3D space (maximum range: ±14 μm; minimum step: 2 pm). The contact area of the W tip with ReS_2 showed different contrast when the tip slightly moved on the monolayer surface, thus it ensured the contact area was phase-transformed.

3.2.4 Strain Analysis on (S)TEM Images

According to von Mises strain distributions, for monolayer ReS_2 sample, the strain can be separated in two parts including dilatational component and shear component. We use local strain hydrostatic invariant and local strain invariant to describe the dilatational and shear component separately, in order to quantify the strain distribution in a symmetric atomic structure (T phase) with the known reference state. Therefore, the dilatational atomistic local strain in 2D materials can be expressed as:

$$\eta_m^{2D} = \frac{1}{3} Tr\eta = \frac{1}{4}(d_0^{-1} TrM_i - 2),$$

and the share invariant is:

$$\eta_s^{2D} = \sqrt{\frac{1}{2} Tr(\eta - \eta_m I)^2} = d_0^{-1} \sqrt{\frac{1}{4} Tr(M_i - \frac{TrM_i}{2} I)^2}.$$

The six closest neighbor atoms are regarded as *j* for the strain calculation in each single atom *i* of 1T phase ReS_2. For each neighbor atom *j* of atom *i*, M_i is the sum of cross product of the transformation matrix *J* and its transposed matrix. d_0 is a constant depending on the average distance of two atoms in the symmetric reference material.

3.3 Results and Discussions

3.3.1 Phases in ReS_2

For 1L ReS_2, the calculated electronic structures of T (no dimerization), T′ (dimerization in one direction) and T′′ (dimerization in two directions) phases are presented in Figure 3.2a-c.

It is noted from the metallic T phase, to distorted quasi-1D dispersive T′ phase, and the most stable gapped T″ phase, the relaxed lattice parameters significantly increase.

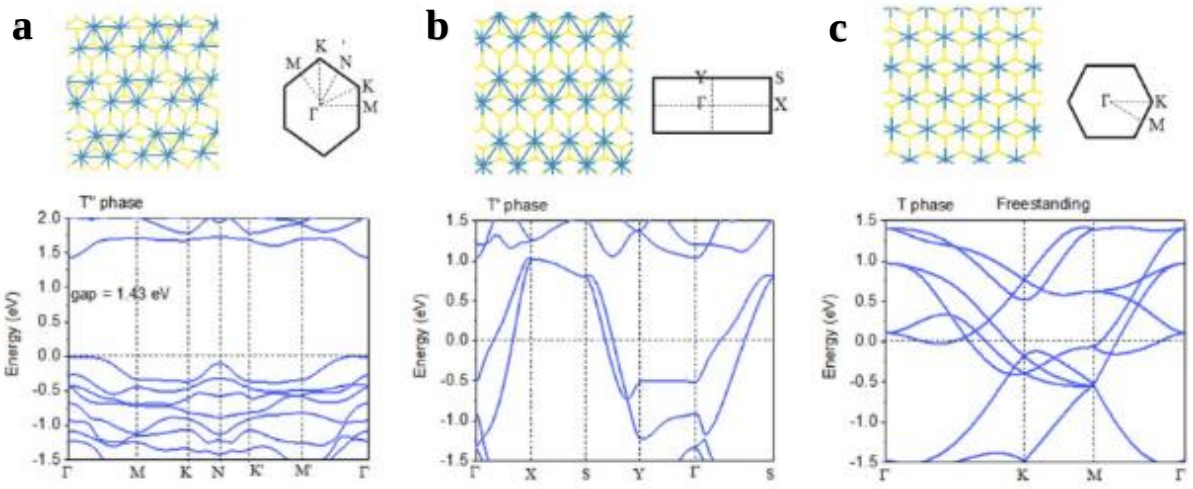

Figure 3.2 Atomic structures and electronic structures of T (no dimerization), T' (dimerization in one direction) and T'' (dimerization in two directions) phases from DFT calculation.

Prior to current work, patterning of metallic phases in 2D semiconductors has been recognized via laser irradiation or patterned doping. With much smaller beam size (down to Å scale), here we employ high energy electron beam (60 kV) to trigger phase transitions, aiming for much higher precision for phase patterning. Large area 1L ReS2 is obtained and confirmed as T'' phase (Figure

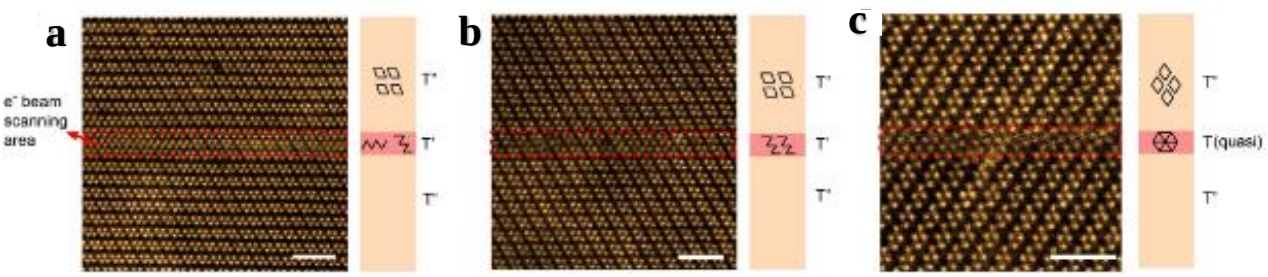

Figure 3.3 HAADF images of phase transition from *pristine* T'' ReS_2 after e^- beam patterning along **a**, **b** and **a+b**. T'' phase transforms to T' phase when e^- beam scans along **a** and **b**, while transforms to T phase when e^- beam scans along **a+b**. The scanning areas are marked by red rectangles. Scale bar=2nm.

3.3a).We first apply quasi one-dimensional (1D) electron beam (e^- beam) exposure along three directions, marked as ***a***, ***b*** and ***a+b***. The width of such 1D exposure area is approximately 1 nm, highlighted by red rectangles in Figure 3.3a-c, and the e^- beam scanning directions (in STEM mode) are identical to the elongated directions of these rectangles.

The 1L ReS_2 shows prominent atomic structural transformations on such selected area under e^- beam exposure, while completely no transformation occurs in unexposed area. Two adjacent diamond shape Re chains are zipped up along ***a*** or ***b*** directions when the e^- beam scanning direction is along ***a*** or ***b***, respectively, yielding the ultrathin T′ phase (three unit cell in width) embedded in pristine T″ phase (Figure 3.3a, b). If 1D e^- beam exposure zone (also scanning direction) is long ***a+b*** direction (Figure 3.3c), the affected diamond Re chains have reorganization and a three-unit-cell-width T phase like structures embedded in pristine T″ phase. The above results well exhibit the atomic control capability of phase patterning in 2D ReS_2 by converged e^- beam. Since the T and T′phases are metallic (Figure 3.2a, b), it implies ultrathin metallic wires (< 1nm width) can be directly written in 2D semiconductors.

3.3.2 Phases Transition on ReS_2

After successful 1D phase patterning using e^- beam, we then apply e^- beam exposure on 2D areas of 1L ReS_2. In Figure 3.4a, serial STEM images during e^- beam irradiation in a 2D square box are shown. The electron beam mainly creates S vacancies by knock-on effect and sometimes Re vacancies in 1T″ ReS_2. We extract the atomic positions for all Re atoms from

STEM images, and highlight the defective zones as well as the new phases (T or T′) in blue color (Figure 3.4a), by measuring the distance/distance ratio deviations between each Re atom and their six neighboring Re atoms (Methods). After 94s of e^- beam irradiation, the switch of diamond chain directions and domain boundaries shows up at where atomic defects formed previously. With the increasing of irradiation dose, the lattices become less distorted (Figure 3.4a,122s). Some positions turn into T′ phase as in the 1D exposure case. At 141s, two nucleuses of 1T phase emerge. Until 244s, number of Re atoms in these nucleuses rapidly increases from 50 to 100 (Figure 3.4b). We find the critical nuclei size of T phase in T″phase is *ca.* 2.5nm×2.5nm in 1L ReS_2 (Figure 3.4a, 141s). Meanwhile, after the 1T phase area grows larger, the mismatched lattices and lattice constants between T″ and T phases inevitably cause some nm-sized pores in the sample. More Re defects can delay the transition from 1T″ to 1T phase, owing to the prevail twist of diamond chain direction (Figure 3.4c, attempt 5). Therefore, S vacancies dominate the phase transition from T″to T/T″.

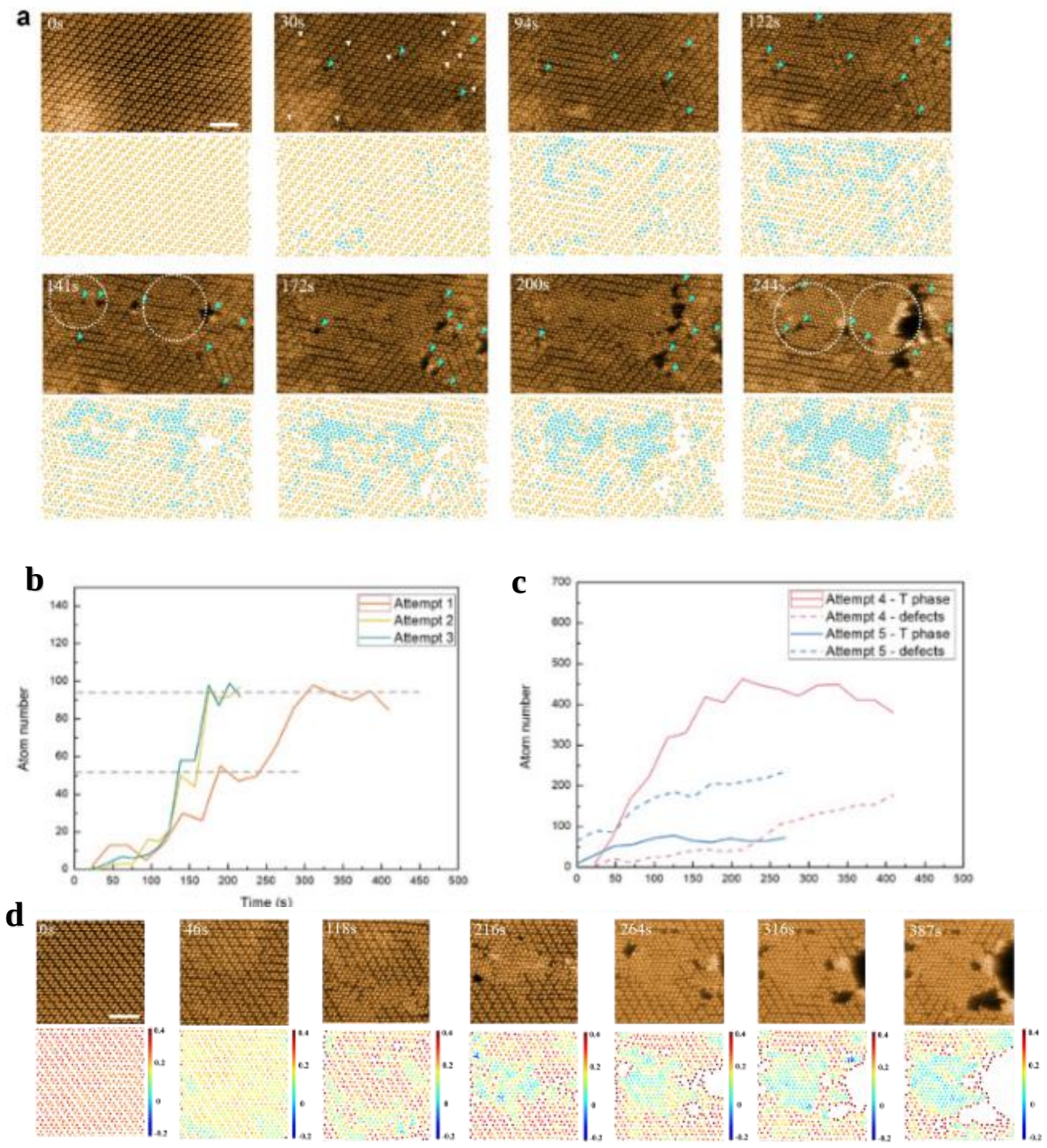

Figure 3.4 2D phase patterning of ReS_2. (a) HAADF (up) and scheme of atomic position (down) of 2D phase patterning. In HAADF images, S and Re atomic defects are highlighted by white and blue triangles separately. Two clusters of T'' to T phase transition areas are marked by white dashed circles. In schematic pictures, yellow dots stand for Re atoms in T'' phase, blue dots stand

for Re atoms in T phase. Scale bar=2nm. (b) Number of T-phased Re atoms in each cluster during e^- beam patterning. Three attempts are calculated. (c) Change of area on Re defects and T phase during two attempts. Red lines stand for Re defects rich case, blue lines stand for Re defects poor case. (d) Phase patterning(up) and the dilatational strain mapping(down) on a single cluster. Scale bar=2nm.

The electronic doping effect on the phase equilibrium in 1L ReS_2 has been evaluated by our DFT calculations. We find limited influences from electronic doping on the relative stabilities of different phases, implying the atomic defects introduced by e^- beam modulate the phase stabilities via straining effect. We measure the von Mises strain distributions from serial STEM images during phase transitions (see Methods). The dilatational strain invariant keeps shrinking from the original T″ phase (0 s) until the formation of T phase (118 s) (Figure 3.4 d). After the critical strain is reached (η_m^{2D}= 0.13), the 1T phase emerges. The shear strain invariant does not show much difference in 1T″ and 1T phases.

3.3.3 Density Functional Theory Calculation of Phase Transition

Our DFT results agree well with the above observations. The free energies as a function of lattice constants for T″, T′ and T phases of 1L ReS_2 are presented in Figure 3.5a, b. Under uniaxial strain conditions, the T″ starts to transform into T′phase (at lattice constant a=5.8 Å), while T phase is hardly formed. However, under biaxial compressive strain, the energy of T phase approach rapidly to T″phase. Considering the phase coexistence, we estimate the transition point of T″phase to T phase starts when lattices constants reach 5.98 Å. The

experimentally measured lattice constants for T phase and T′phases are within the ranges of theoretical results.

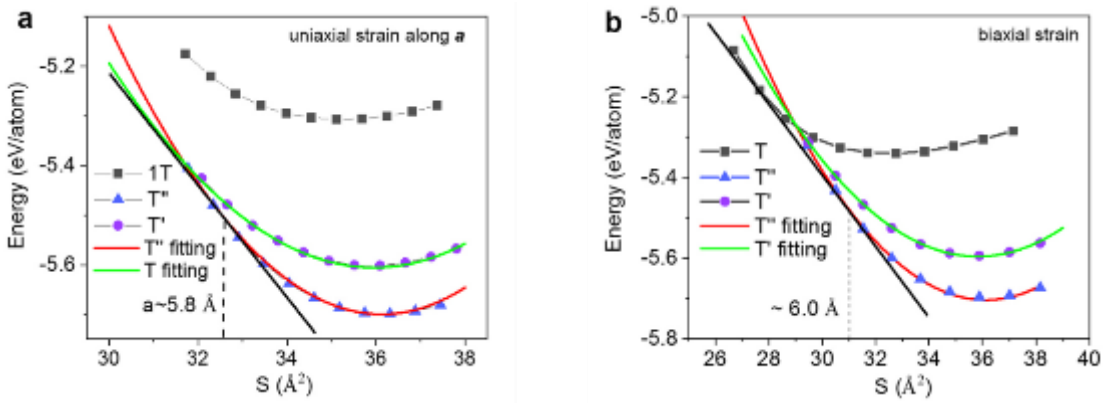

Figure 3.5 DFT calculation of free energies as a function of ReS_2 lattice constants. (a) Calculated result of applying uniaxial strain along ***a***. (b) Calculated result when the strain is biaxial (along ***a***+***b***).

S vacancy position	E_{form}(eV)
Single-1	0.13~3.09
Single-2	-0.14~3.09
Single-3	-0.99~2.25
Single-4	-0.54~2.69
Double-3,1	-0.07~3.16
Double-3,2	-0.29~2.94
Double-3,4	-0.43~2.80
Double-3,5	-0.49-2.74

Double-3,6	-0.95~2.28

Table 3.1 S atomic vacancies (Figure 3.6) and corresponding formation energies in 1L ReS_2 from DFT calculation.

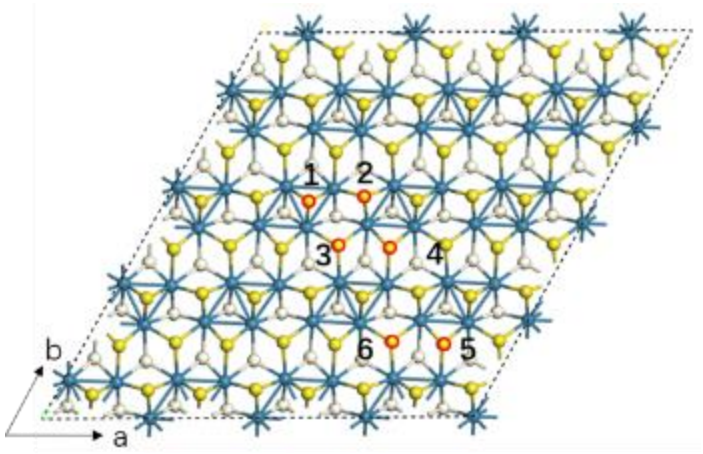

Figure 3.6 Atomic structure of 1L ReS_2 and different S atomic positions for knock-on energy calculation.

For quasi 1D-like e^- beam exposure, inherently the compressive strain perpendicular to the 1D scanning zones can be induced in the beam scanning area due to lattice contraction around S vacancies (Figure 3.4a-c). Besides, due to multiple S atoms exist in unit cell of ReS_2, we find that linearly distributed S atomic vacancies are the most energy favorable, from the vacancy formation energies in 1L ReS_2 obtained by DFT (Figure 3.6 and Table 3.1). Thus, the 1D e^-beam exposure condition is very close to the uniaxial strain condition (perpendicular to 1D direction), and the T′phase is more frequently attained. In contrast, under 2D e^- beam exposure, the S vacancies are stochastically distributed in the beam-exposed area, hence 2D biaxial compressive strain is generated more commonly, causing the nucleation and growth of T phases.

3.3.4 Conductivity Test on ReS_2 Phases

As mentioned above, T and T′phases are intrinsically metallic. To confirm the electrical properties of newly patterned phases in T′′ phase ReS_2, we further performed *in situ* TEM-STM experiment[1] to locally probe the electrical conductivities. The quasi-parallel 200 kV electron beam in TEM is employed to convert an area of $0.3\mu m^2$ of T′′phase into the T/T′ phase (Figure 3.7a). The serial selected area diffraction patterns are shown in Figure 3.7b. The reduction of dimerization and reduction of lattice constants are clearly observed. During 150s of e^- beam exposure, the *in situ* Tungsten (W) STM tip is manipulated to make intimate contact with the new phase area, and the current voltage (I-V) signals are sequentially recorded (Figure 3.7c, d). The contact area between W tip and 1L-ReS_2 are mechanically stable, so the measured conductivities directly reflect the evolution of contact resistances (the voltage drop is mainly imposed on the contact zone in our setup[2]). Compared to the contact with pristine T′′phase (Figure 3.7d, e), the same contact with new T phase zone has increased conductivity by 10 fold, after e beam exposure for 54s. The conductivity further increased to 37 fold after total 270s exposure. The integrity of 1L ReS_2 is kept and no large crack/hole over 10 nm is induced throughout the above experiment.

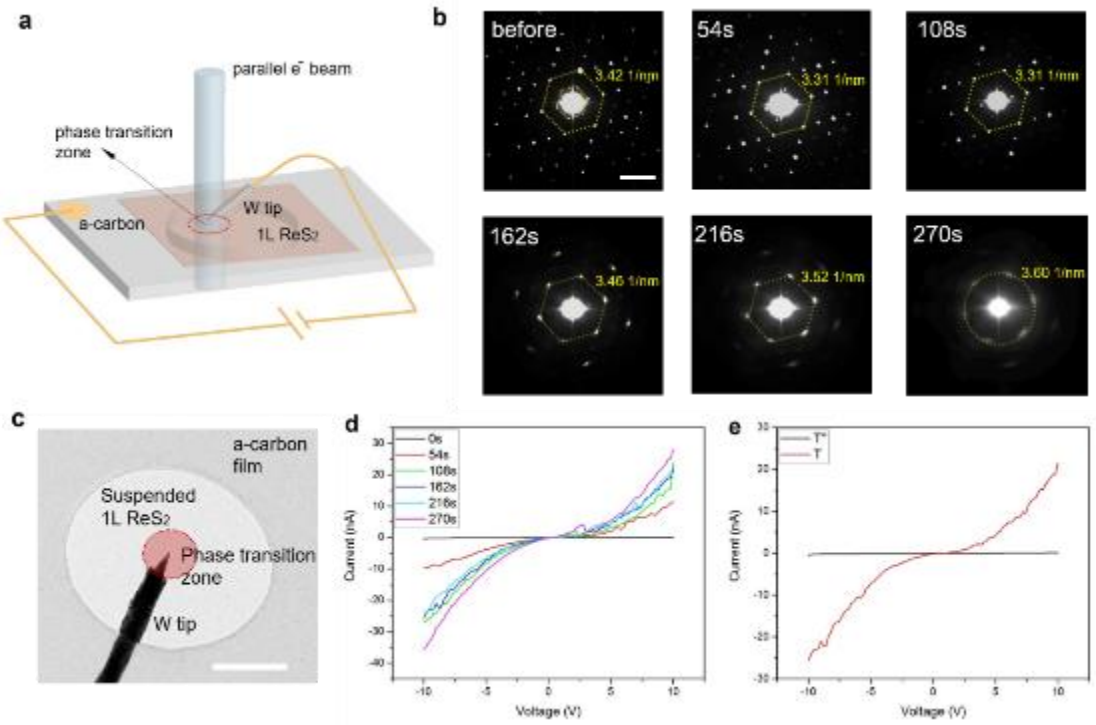

Figure 3.7 Phase transition and *in situ* conductivity test. (a) Scheme of *in situ* TEM-STM conductivity test. (b) A serial change of SAED patterns on 2D ReS_2 during e^- beam patterning. Scale bar=5 1/nm. (c) TEM figure of suspended 1L ReS_2 on a carbon grid, contacting with a W tip for conductivity test. Scale bar=0.5μm (d) Current-Voltage curves with patterning time goes by. (e) Comparison of Current-Voltage curves on T''phase ReS_2 and T phase ReS_2.

3.3.5 Summary

Therefore, here we demonstrate the e- beam direct patterning technique can be engineered to write 1D metallic wires, 2D pads or other metallic patterns in 2D semiconductive ReS_2. Both the parallel e- beam and converged e- beam mode work well for such patterning, and the allowed range of e- beam energy at least spans over 60 to 200 kV. The converged e- beam can reach single atomic precision for phase patterning (for 1D wire). With advanced aberration corrections[3], currently electron beam has been able to converge to sub-Å range, which is much

smaller than any optical lithography techniques limited by diffraction. The atomic patterning by e- beam is also much faster than traditional STM techniques for atomic lithography which can only move the atoms one-by-one. The possible atomic scale 2D semiconductor-metal heterostructures enabled by our novel e^- beam patterning method hold the promises for the facile fabrication of the quantum devices in near future.

References

1. Naitoh, Y.; Takayanagi, K.; Tomitori, M. Visualization of tip-surface geometry at atomic distance by TEM-STM holder. *Surface science* **1996**, 357, 208-212.

2. Wong, L. W.; Huang, L.; Zheng, F.; Thi, Q. H.; Zhao, J.; Deng, Q.; Ly, T. H. Site-specific electrical contacts with the two-dimensional materials. *Nature communications* **2020**, 11, 1-10.

3. Haider, M.; Rose, H.; Uhlemann, S.; Schwan, E.; Kabius, B.; Urban, K. A spherical-aberration-corrected 200 kV transmission electron microscope. *Ultramicroscopy* **1998**, 75, 53-60.

Chapter 4 Fracture and Crack Propagation on 2D ReS_2

4.1 Introduction

In general, there are three fracture modes (I, II, and III),[1] corresponding to opening, shearing, and tearing loads, which are unambiguously defined for the fracture in 3D bulk material. The three modes are shown in the schematic diagrams in Figure 4.1. Mode I is known as the opening mode refers to the applied tensile loading. It is the most common mode in the fracture of materials and in this mode the fracture toughness can be tested. Mode I is decided by the critical stress intensity value. Mode II is determined by the shear stress towards the in-plane direction, the direction of shear stress is usually on the edge of the crack because it is an in-plane stress. Tearing mode is regarded as Mode III, the shear stress is applied out of plane in this case. The direction of shear stress and edge of the crack are parallel. In terms of 2D atomic layers, here we show that the shear strain along the crack line (hence mode II) can trigger crystal rotation and atomically parallel restacking of the postcrack edges. This particular phenomenon is only allowed in such ultrathin flexible 2D materials, where the restacking of these atomic layers does not cost a high level of bending energy.

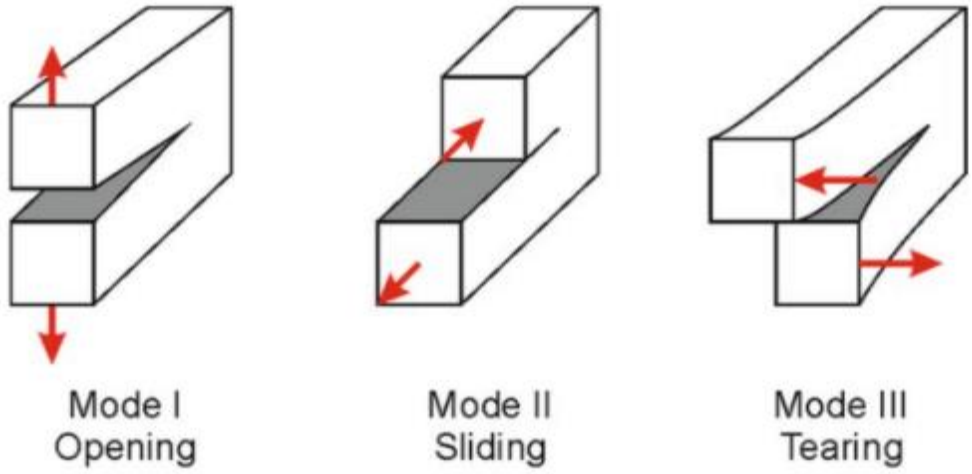

Figure 4.1 Schematic diagram of three fracture modes.[1]

4.2 Methods and Experiments

4.2.1 Growth and Transition of Monolayer ReS_2

ReS_2 was grown on a c-face sapphire substrate by the atmospheric CVD system. Ammonium perrhenate (NH4ReO4) (Aldrich, 99.999 %) and Sulfur powder (Aldrich, 99.998 %) were used as precursors with weight ratio 1: 50, separately put in two quartz boats as shown in Figure 4.2a. The clean c-face sapphire 1 cm × 1 cm substrate was placed polished face down on the top of Re source. A two-zone splitting tube furnace was used to control accurately sulfur and substrate zone temperature, respectively. Prior to the temperature ramping up, 300 sccm of

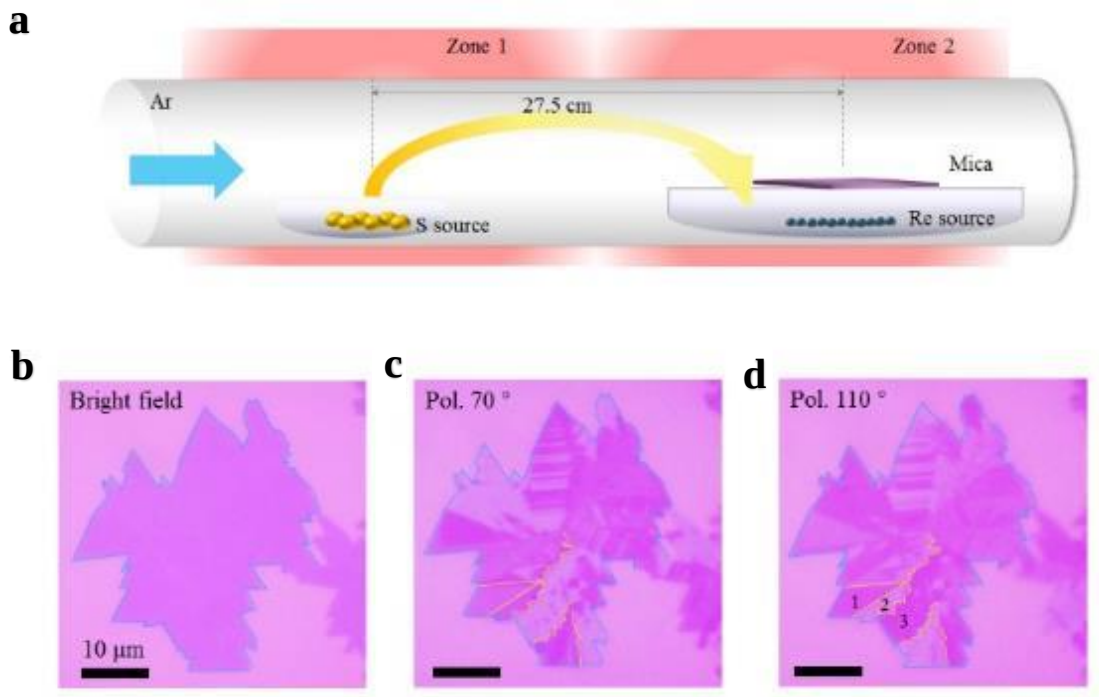

Figure 4.2 CVD growth of monolayer ReS_2. (a) Scheme showing the CVD process of ReS_2. (b)-(d) Optical microscopy images showing the size, morphology and domain structures of anisotropic monolayer ReS_2. Scale bars 10 μm.

Argon gas was purged through the quartz tube for 10 minutes. During the deposition process, argon gas (80 sccm) was as the carrier gas to transport sulfur vapor to substrate zone. The sulfur zone was ramped to 200 ° C, at the same time, the substrate zone reached 850° C in 30 minutes and then held for 10 minutes. The stable T phase in ambient condition of ReS_2 is triclinic and highly anisotropic, which stems from the tetragonal (T) phase prevalent in TMDs with "diamond" type superlattices in two directions (labeled as ***a*** and ***b***) and slightly distorted (γ=119.8°). Figure 4.2b is the major characterization results of our mono-atomic-layer ReS_2 membrane. The bilayer ReS_2 specimens were prepared by the same methods and in some flakes commensurately or incommensurately stacked bilayer ReS_2 could be found.

By PMMA-assisted technique, the CVD grown ReS_2 was transferred on a TEM grid. Initially, thin layer PMMA was spin coated on the as-grown sapphire substrate at 3000 rpm for 50 seconds. With the aid of PMMA, the ReS_2 detached from substrate by emerging in 75 ° C deionized water for two hours. Next, the PMMA/ ReS_2 layer was transferred onto a TEM grid and dried at ambient temperature. Acetone vapor was introduced for gentle removal of PMMA film.

4.2.2 *In Situ* (S)TEM Characterization on ReS_2

The aberration corrected STEM under 60 kV accelerating voltage was applied in this work to improve the image resolution and prevent beam damage. The 60 kV is lower than the energy requested to produce knock-on damage for S and Re atoms in monolayer ReS_2. Moreover, the ultrafine displacement control of the crack front down to single unit cell scale was achieved. These technical improvements are key to the realization of the atomistic crack observations. In specific, the STEM images for ReS_2 samples were performed on a JEM-ARM 200F transmission electron microscope (TEM) retrofitted with a CEOS spherical (Cs) aberration corrector. A vacuum value during measurement was 1.3×10^{-7} mbar, together with the electron beam current of 13.1 μA. At the time of performance, the scanning probe size was 1.5 Å. For image acquisition, the camera length of STEM was 120 mm. The defocus was -4 nm and acquisition time of HAADF image was 19 μs per pixel in order to minimize damage and get the figures with lower drift. The 512 × 512 size pixel images were acquired with the CL aperture of 40 μm and the range of collection angle was 45 to 180 mrad so that the atomic images with proper contrast can be obtained. Wiener filtering was applied on HAADF images for reduction of noises. The TEM images of graphene were acquired with JEOL 2010F transmission electron microscope fitted with CEOS spherical (Cs) aberration correctors. The TEM was operated under an acceleration voltage of 80 kV and the samples were measured at room temperature. The electron beam intensity during HRTEM observation is ~0.1 pA/nm^2. The Wiener filtering was carried out on the image post-processing.

Ultrahigh beam intensities (spread beam with intensity over 0.3 pA/nm^2 usually for beam shower) were exposed on controlled circled areas (~100 nm diameter) of ReS_2 for 15~30 min. Afterwards the beam was quickly switched to (S)TEM imaging on the crack dynamics outside of the beam exposed zones. These freshly generated cracks by such method can further extend 10~50 nm, depending on specific stress conditions. The particular lattice switching in ReS_2 layers also contribute to the in-plane mechanical loading. The time interval of serial *in situ* STEM imaging is between 13~20s. The specimen drift was compensated, hence the dynamics of cracks could be directly registered.

4.2.3 Strain Analysis on Fracture

The GPA strain analysis (on high resolution HAADF images) was performed with the reflexes (in reciprocal space) perpendicular to ***a*** and ***b*** axis as the two basis, respectively. The GPA analysis resolution was set as 0.3~0.4 nm, smoothing factor was set as 7.0. For the discretized atomic strain analysis on the HAADF images, considering the lattice structure and crystal symmetry in different materials, it was performed for half unit cells or Voronoi cells (for $ReSe_2$, determined by the locations of Re atoms retrieved by Gaussian fitting of STEM/TEM images). The coordination (***x*** and ***y***) of the discrete atomic stress, strains and strain gradients are defined along ***a*** axis (***y***) and perpendicular direction of ***a*** axis (***x***). Their locations are defined by the averaged three corner positions of the triangular cells, and the faces are defined as the faces perpendicular to ***x*** and ***y*** coordinates, respectively. Non-deformed state (the zero stress/strain condition) is relaxed by DFT, same as our high resolution STEM measurement results. The normal and shear strain components of the cells follow the standard of linear elastic mechanics

(finite element theory) (assume the triangular cells have constant strain over the cell if the three corner positions (u_1, v_1; u_2, v_2; u_3, v_3)) are determined (by *in situ* STEM images) under linear approximation). $\{\varepsilon_x, \varepsilon_y, \varepsilon_{xy}\}=\{\frac{\partial u}{\partial x}, \frac{\partial v}{\partial y}, \frac{\partial u}{\partial y}+\frac{\partial v}{\partial x}\}$. This formalism can be applied for all the cells in the lattices/images including the singular crack tip zone.

The theoretical values for the strain gradient maxima in crack tips can be expressed as

$$\frac{\partial \gamma}{\partial y}=\frac{\sigma_T}{tG}, \qquad \text{(Mode I)} \tag{1}$$

$$\frac{\partial \varepsilon_y}{\partial y}=\frac{\sigma_S}{tE}, \qquad \text{(Mode II)} \tag{2}$$

Where E and G are the tensile and shear modulus, respectively, t is the distance from the maxima location to crack path, σ_T and σ_S is ideal tensile and shear strengths of concerned atomic cohesive bonding at the crack front which is related to material fracture toughness. The equilibrium analysis diagrams are appended in Figure 4.3.

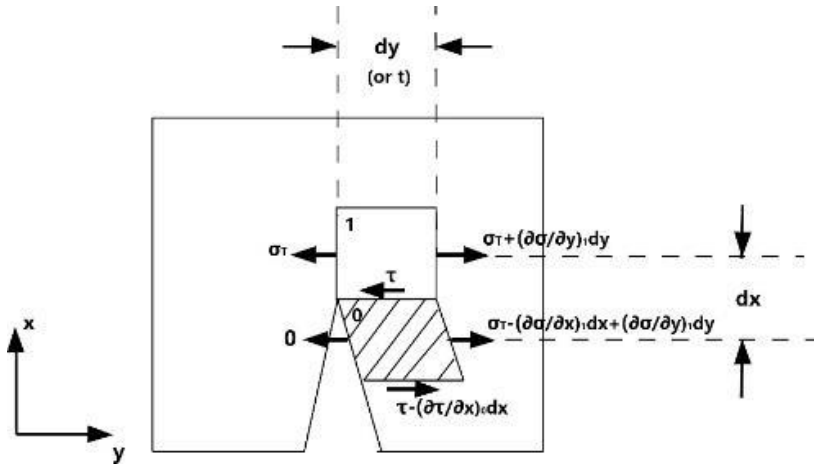

Figure 4.3 Illustration of the strain/strain gradient components, and the force equilibrium analysis diagrams for the mode I cracks.

Simply consider a singular model for the mode I crack tip, there is one atomic-block (non-shadowed) on the crack path, as shown in the above. Before the onset of atomic bonding breakage, along ***y*** direction, the tensile stress is equal to the ideal material strength ($\boldsymbol{\sigma}_T$). Right after atomic bonding breakage (shadowed block), one side (towards the newly formed crack surface) has the normal stress almost drops to 0 (cracked state, atomic interaction negligible), and the other side has the tensile stress $\boldsymbol{\sigma}_T-(\partial\boldsymbol{\sigma}/\partial\mathbf{x})_1 d\mathbf{x}+(\partial\boldsymbol{\sigma}/\partial\mathbf{y})_1 d\mathbf{y}$. Here the normal strain gradients are referring to the non-cracked (non-shadowed) block (subscript 1), while the shear strain gradient are for the cracked (shadowed) block (subscript 0). Experimentally, the 0 and 1 blocks are neighboring pairs of atomic cells. Using the force equilibrium along y axis, the derivation of the strain gradient criterion is shown below and in the supplementary materials of the manuscript.

According to the force equilibrium along y axis on the shadowed block (block 0),

$(\partial\tau/\partial x)_0 dx\times dy=(\sigma_T-(\partial\sigma/\partial x)_1 dx+(\partial\sigma/\partial y)_1 dy)\times dx,$

Hence $(\partial\tau/\partial x)_0-(\partial\sigma/\partial y)_1=(\sigma_T-(\partial\sigma/\partial x)_1 dx)/dy,$ $(\tau=G\gamma,\ \sigma=E\varepsilon)$

$(\partial\sigma/\partial x)_1 dx$ is negligible compared to σ_T, meanwhile, as we measured directly from the experimental images and the simulation results for a wide range of materials, $(\partial\sigma/\partial y)_1$ is negligible compared to $(\partial\tau/\partial x)_0$. Finally, we got $(\partial\gamma/\partial x)_0=\sigma_T/tG$ (eq. 1). The eq. 2 can be derived by a similar fashion.

4.2.4 Density Functional Theory Calculations

All atomistic calculations in this study were carried out by using spin-polarized DFT calculations as implemented in the Vienna ab initio simulation package (VASP) program package to explore the geometries of ReS_2 monolayer. The exchange-correlation interactions are described by using PBE functional with a gradient approximation (GGA). The kinetic energy cutoff for the plane-wave basis set was 400 eV, and the electronic SCF tolerance was set to 10^{-4} eV. The distance of vacuum layer was set to be more than 15 Å, which was adequately large to avoid interlayer interactions. Fully relaxed geometries were obtained by optimizing all atomic positions until the Hellmann–Feynman forces are less than 0.05 eV/Å. The k-points samplings are 3×1×1 in the Brillouin zone for structural optimizations. The size of the DFT supercell is 2.74 nm width (***x*** axis) by 4.00 nm length (***y*** axis), and ***z*** direction is 15 Å which can provide enough space to avoid the interactions by layers. The system contains 80 Re atoms and 156 S atoms to simulate the entire fracture process. The uniaxial load is applied by elongating the length the supercells along ***x*** coordinate (perpendicular to ***a*** axis in ReS_2). The strain, $\varepsilon = (c_s - c_0)/c_0$ corresponds to the applied stretching (6-10%), where c_s and c_0 are the lattice constant of strained and the pristine ReS_2 monolayer along ***y*** axis (crack direction). The pre-cracks were introduced by removal of four neighboring S atoms.

4.3 Results and Discussions

4.3.1 Crack Extension in Atomic Scale

The TEM characterization of transferred pristine ReS_2 including low-magnification figure, SAED and STEM-HAADF for atomic structure is shown as Figure 4.4. The cracks made by in-situ method and the condition of the edge is shown in Figure 4.5 In addition, the exact

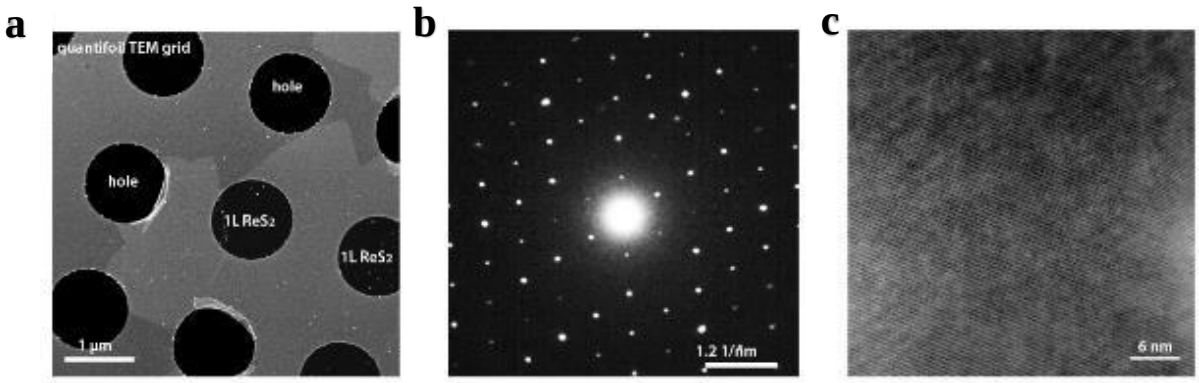

Figure 4.4 (a) Low magnification STEM image of transferred ReS2 membrane on QuantifoilTM TEM grid. (b) Selected area diffraction (SAED) pattern of 1L ReS2 single crystal. (c) HAADF image of pristine single crystal area of ReS2 showing the good crystallinity.

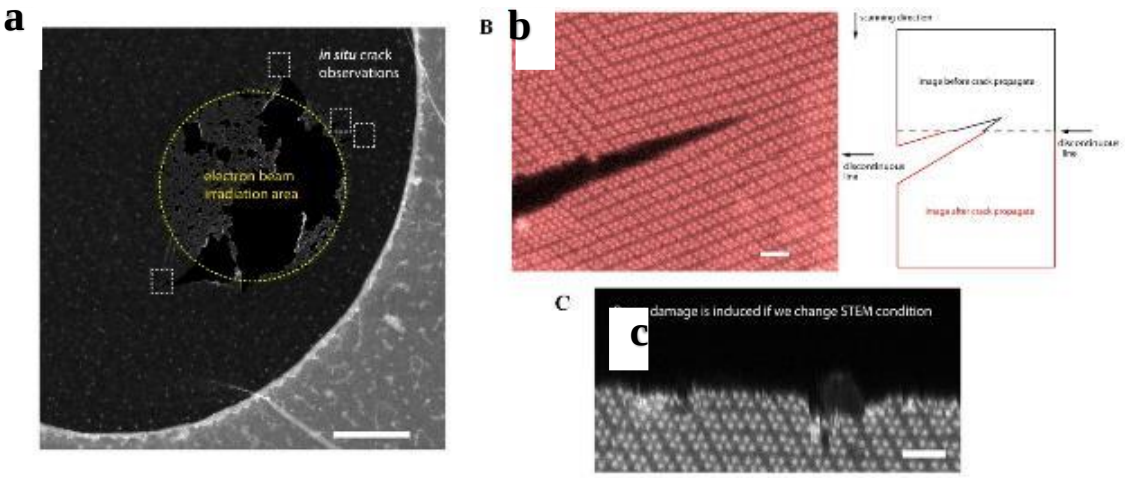

Figure 4.5 The in situ cracking method and conditions. (a) Low magnification image of 1L ReS2 after controlled beam irradiation in circled area, several cracks are formed and left for higher magnification imaging, these observation areas (dashed rectangles) are without any prior electron beam irradiation. Scale bar 100 nm. (b) No electron beam effect on crack tip zone when crack

moving. (c) The HAADF image of beam damaged edges if the scanning time for each pixel is doubled. Scale bar 1 nm.

time for each step of crack propagation could be occasionally determined by the discontinuous lines in images due to the crack front movement while electron beam scanning. However, such movements close to the crack tip/front (within 2-3 unit cells) were rarely seen, showing the crack tip movement is normally irrelevant to the beam excitations, but triggered by mechanical origins. The crack along ***a*** axis was straight and atomically smooth. No loss of atoms or reconstruction was noticed at the cracking tips. Beam damage will be induced only if we change the STEM conditions. Anisotropic monolayered 2D ReS_2 (Figure 4.6a) was used to understand the structure of crack tip and its propagation behavior at the atomic scale. The defect-less nature of our specimens has been confirmed by the atomic force microscopy (AFM) indentation tests. Further, the *in situ* STEM experiments were carried out at room temperature. While electron beam irradiation was initially used to generate cracks, beam effects have been excluded in the *in situ* mechanical tests. Mode I crack – which occurs when tensile load is applied perpendicular to the crack direction – was most commonly observed (Figure 4.6b). Two snapshots of Mode I crack along ***a*** axis of ReS_2, acquired through high angle

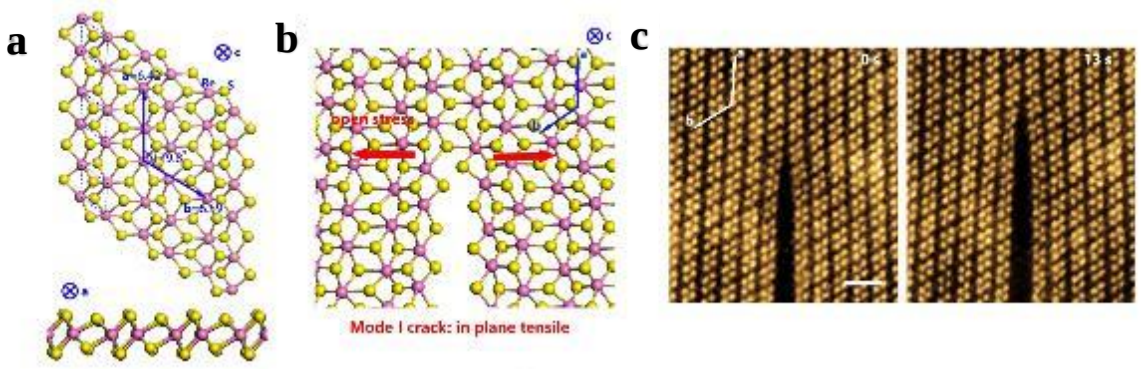

Figure 4.6 The Mode I cracks in 2D ReS_2 along a axis. (a) The monoclinic crystal structure

model of 2D monolayer ReS2, plan view (upper) and side view (lower), with a,b,c as basis vectors. (b) Scheme for the Mode I crack in ReS2 under tensile stress. (c) Two HAADF snapshots of the crack tip zone of an on-going crack. Scale bar = 1nm.

annular dark field (HAADF) imaging are shown in Figure 4.6c. The crack was straight and atomically smooth.

We find that continuous cracking is discretized down to the atomic scale. That is, cracking is periodic and repeatable along the unit cells. Further observations suggest that cracking occurs in two temporal stages: (1) Local strain energy gained by crack front so larger opening is formed (0 s and 39 s in Figure 4.6a, 13 s and 26 s in Figure 4.7b); and (2) release of the strain energy and crack propagation (26 s in Figure 4.7a, 0 s in Figure 4.7b). The continuous propagation of one crack tip (outline edge contours) is depicted in Figure 4.7c. Although

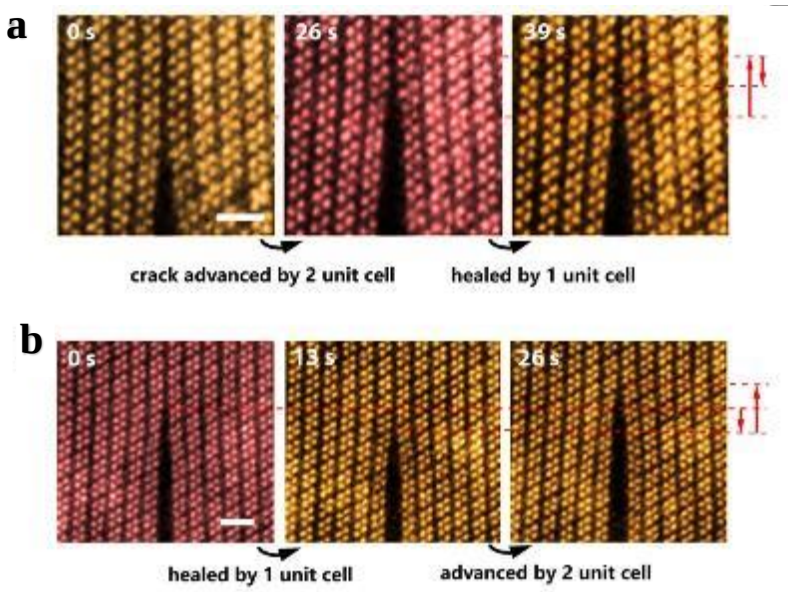

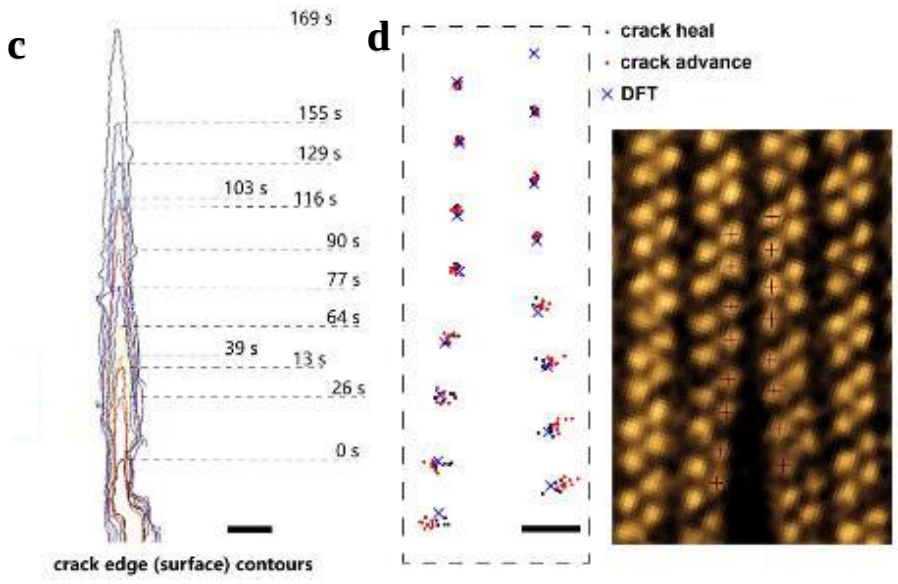

Figure 4.7 (a, b) *In situ* snapshot series of cracking and healing processes in 2D ReS_2 by single steps (unit cell). Cracking in yellow and healing in red. Scale bar = 1nm. (c) Evolution of a crack edge contour observed by *in situ* TEM with observation times marked, scale bar = 2 nm. (d) The inner most 16 Re atoms.

fracture is usually irreversible, we were able to observe crack "healing" by re-bonding of free edges behind the crack front (26 s to 39 s in Figure 4.7a and 0 s to 13 s in Figure 4.7b).

The maximum length of continuous crack healing was three unit cells in our observations. The healing implies that the fracture is entirely brittle, and plasticity or reconstructions are absent in the ReS_2. The inner most Re atom positions within the crack tip zones were extracted from experimental images and overlaid with our DFT analysis results (Figure 4.7d). The experimental atomic positions for crack advance and healing were distinctly separated, in agreement with the DFT simulated atomic structures. Our DFT analysis results (Figure 4.8a) on Mode I cracks along ***a*** axis in ReS_2 also reproduce the atomically smooth edges and the

sequential rupture of Re-S bonding at the crack tips. The free edges formed due to cracking were occupied by dangling S atoms, suggesting that there was no loss of atoms during fracture (Figure 4.8b).

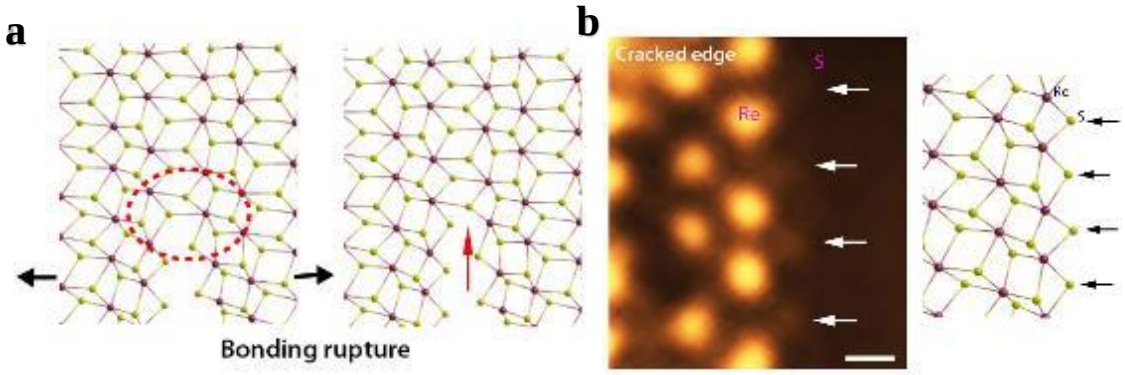

Figure 4.8 Atomic-scale strain analysis on the crack tip zones. (a) Two sequential snapshots of DFT simulated Mode I cracks in ReS_2. The ruptured Re-S bond is marked by red arrow. (b) Magnified HAADF image of one ReS_2 cracked edge, white arrows indicate the position of dangling S atoms. Scale bar = 0.3 nm. Corresponding DFT results of ReS_2 cracked edge shown on right side.

4.3.2 Strain Distribution on Crack Tips

The strain fields near tip zone were mapped through the geometric phase analysis (GPA) on the HAADF images. Negligible far field (>5 nm away from crack tip) strain was found in the sample, implying that the driving force for crack growth is localized, and the cracking step spans one or a few unit cells throughout observations. Meanwhile, utilizing experimentally

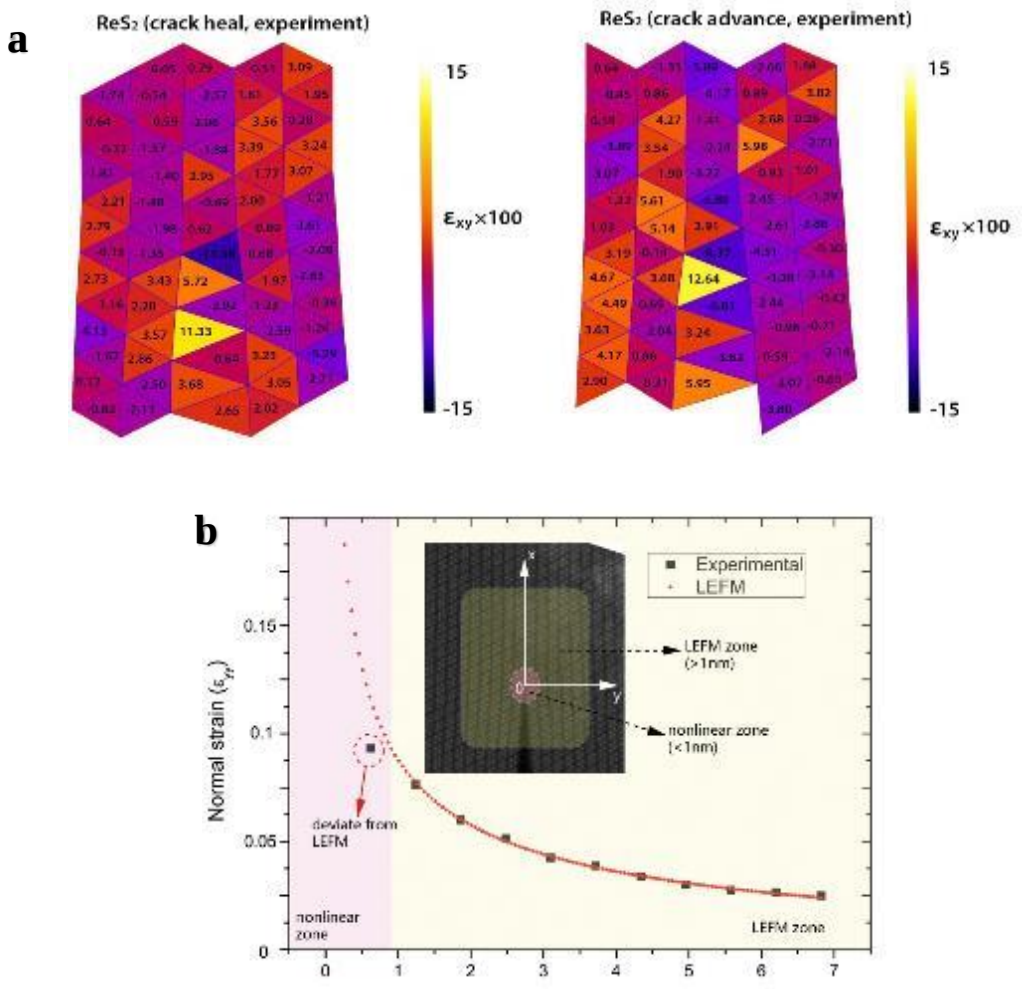

Figure 4.9 (a) Shear strain results (color encoded, discretized by half unit cell) of ReS_2 Mode I crack and healing along ***a*** axis in our experiments. (b) The normal strain on the x axis (shown in the inset) for Mode I crack in 1L ReS_2. The strain inside the 1 nm region deviate from the LEFM theory ($\varepsilon_{yy}E=K(2\pi x)^{-1/2}$). The stress intensity factor (K) can be derived from the fitting parameter in LEFM zone.

determined atomic structure of crack tips, the atomic strains were analyzed for each half unit cell or Voronoi cell to study the critical condition for crack advance (growth) or healing (Figure 4.9a). According to the obtained atomic strains, in the range of 1~5 nm away from the crack tips, the asymptotic strain field by the LEFM (linear elastic fracture mechanics) (Figure 4.9b)

and the J integral approach still hold. For the area within 1 nm distance to the Mode I crack tips, the strain field deviate from the LEFM and the J integral theory, while nonlinear deformation dominates.

Mode I cracks along directions other than ***a*** axis in 2D ReS_2 have been also studied. Lattice reconstruction and switching of ***a/b*** axis were observed, and we found limited dislocation dynamics within tip zone was allowed. In addition, defects influence Mode I crack paths. For example, coherent or incoherent domain/grain boundaries can either accommodate or exclude cracks, respectively. For the commensurately stacked bilayer ReS_2 samples, the cracking in both layers is synchronized which yield similar atomically sharp tips as monolayer ReS_2 (Figure 4.10a, b), the strain distributions are almost identical for the crack tips in bilayers and monolayers (Figure 4.10c, d). In contrast, the incommensurately stacked bilayer ReS_2 could have roughened crack surfaces and different crack paths/directions in the two layers.

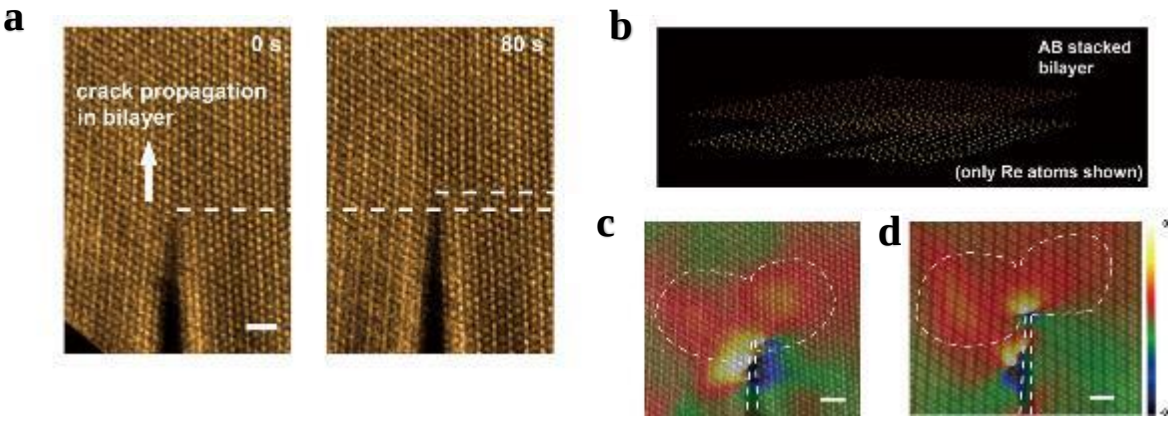

Figure 4.10 Cracks in bilayers, Mode II and Mode III cracks. (a) The STEM snapshots of a crack in bilayer (2L) ReS_2 which propagate by one unit cell. Scale bar=1 nm. (b) Scheme for the bilayer ReS_2 and the always synchronized cracking in the upper and lower layers. (c) The normal (tensile) strain (e_{yy}) distribution corresponding to (a). Scale bar=1 nm. (d) The normal strain

distribution for another 1L ReS_2 sample, showing similar strain fields for 1L and 2L specimens. Scale bar=1 nm.

Typically, in-plane compressive strain in 2D materials cause out-of-plane buckling, therefore Mode II fracture – where shear stress is acting in the plane of the crack – is difficult to observe. Surprisingly, we were able to observe straight cracks steadily propagating in parallel with atomically stacked post-crack edges in ReS_2 samples (Figure 4.11a, b). High resolution images were captured and analyzed for strain distributions at the crack tips (Figure 4.11c, d). Here the major driving force was the shear stress (Figure 4.11b) – originating from faulted stacking by half unit cell. The shear stress is proportional to the magnitude of mismatch in stacking, and the driving force for this crack was gradually reduced by leaving "dislocations" in the crack path (Figure 4.11a). The in-plane shear strain in the near field of the crack tip is again highly

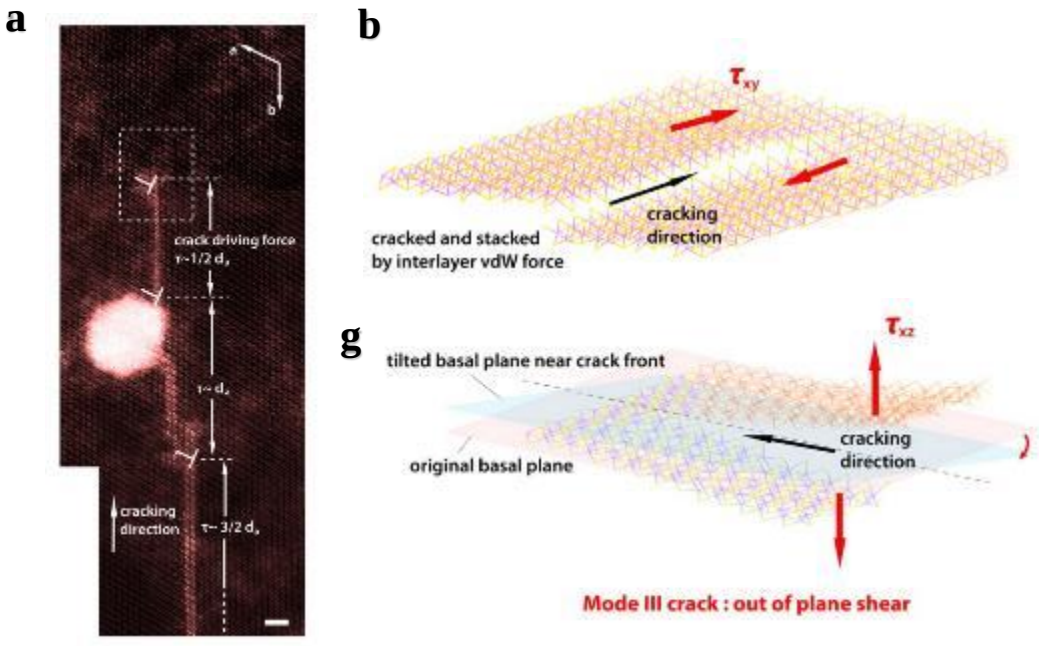

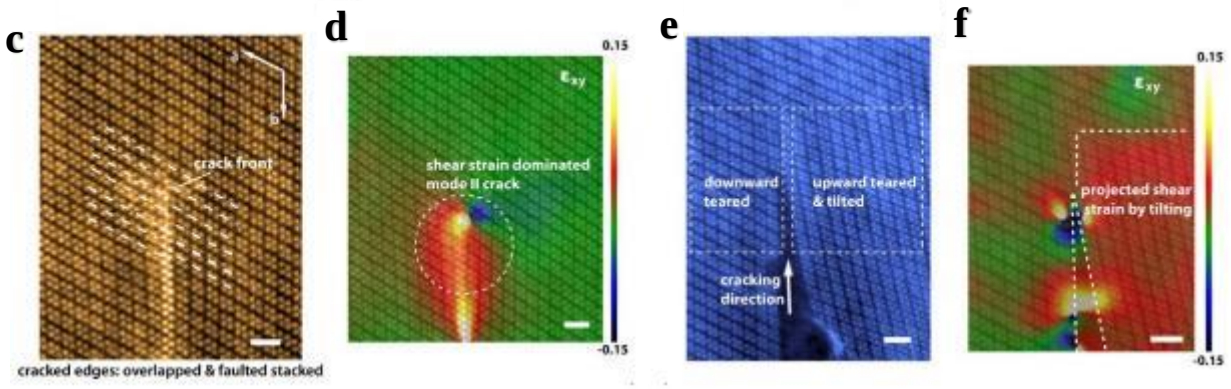

Figure 4.11 (a) Typical Mode II crack in ReS_2, crack edges are stacked and thus have brighter contrast in HAADF. Driving forces (shear) are gradually consumed by emission of partial dislocations (marked). The bright spot (on the left) is caused by PMMA residue during specimen transfer. Scale bar = 2 nm. (b) Scheme of the Mode II crack. (c) Magnified HAADF image corresponding to the dashed rectangle in (a). Scale bar = 1nm. (d) The in-plane shear strain analyzed by GPA method on (c), the dashed circle highlighted the crack front. Scale bar = 1 nm. (e) Example of Mode III crack viewing in original basal plane, scale bar = 1nm. (f) The shear strain analysis by GPA method on (e), showing the tilting in right side of crack, scale bar = 1nm. (g) Scheme of Mode III crack, the original basal (pink) plane is tilted (blue) after crack.

changed. Meanwhile, in mode III crack, Figure 4.11f presents the GPA shear strain analysis of Figure 4.11e, manifesting the plane tilting.

The macroscopic fracture criterion has been well established in the classical fracture mechanics. Here our experiments have confirmed the LEFM can be applied until very small region (nm sized) within the crack tip for entirely brittle materials. On the other hand, for the nonlinear zone in the crack tip core, here we introduce a strain gradient criterion, correlated to the external stress intensity factor, to explain the crack/healing behavior. Defining the crack direction as $\boldsymbol{y}$, basically the shear strain gradient ($\partial\gamma/\partial y$) were used for Mode I cracks, whilst normal strain gradient ($\partial\varepsilon_y/\partial y$) were used for Mode II cracks. It is clear that the shear strain

gradient maxima for Mode I were prevalently larger in cracking cases than in crack healing cases, unlike the strain maxima distributions which were more dispersive. Meanwhile the normal strain gradient maxima in Mode II cracks were stable throughout the cracking process. For the atomic-scale shear strain gradient is a measure of the bond distortion, the maximum strain gradient criterion can also be understood as the maximum bond distortion criterion.

4.3.3 Dynamics of Fracture in ReS_2

Direct strains are unsuitable as criterion for crack growth/healing because an *ad hoc* assumption is needed for the exact location of crack front, which is unrealistic. The crack front is no longer a point, as the traditional fracture theories have assumed,[2] instead it consists of a group of atoms that are strongly deformed within the range of cohesive interactions. We also analyzed the strains obtained from DFT simulations on ReS_2 Mode I cracks. We simulated cracks under different loading conditions (stress intensities) and found that the shear strain gradient maxima in the propagating crack tips are all within 0.18~0.24(1/d), which is in agreement with our *in situ* STEM results and the theoretical value of ReS_2 - validating the strain gradient criterion. Further, the concept of strain gradient could be generalized to other 2D and bulk materials such as graphene and silicon (Si). The DFT and molecular dynamics (MD)[3,4] simulation results on graphene, our TEM results on graphene, and MD simulation results on Si were all tested with the strain gradient criterion (Figure 4.12), yielding strain gradient maxima conditions in accordance with the theoretical values.

The chaotic behavior of crack in atomic scale predicted by can result in the atomic motion virtually unpredictable only by the stress loading conditions. According to our experiments, a regime of the chaotic motion of cracks have been indeed confirmed, when the loading condition (stress intensity factor) satisfies $K>K_c$, K_c defines the boundary between quasi-static cracking and healing. When K is above but close to K_c, the crack will intermittently propagate and stop. In this regime, each step of crack propagation length (crack step length) is not

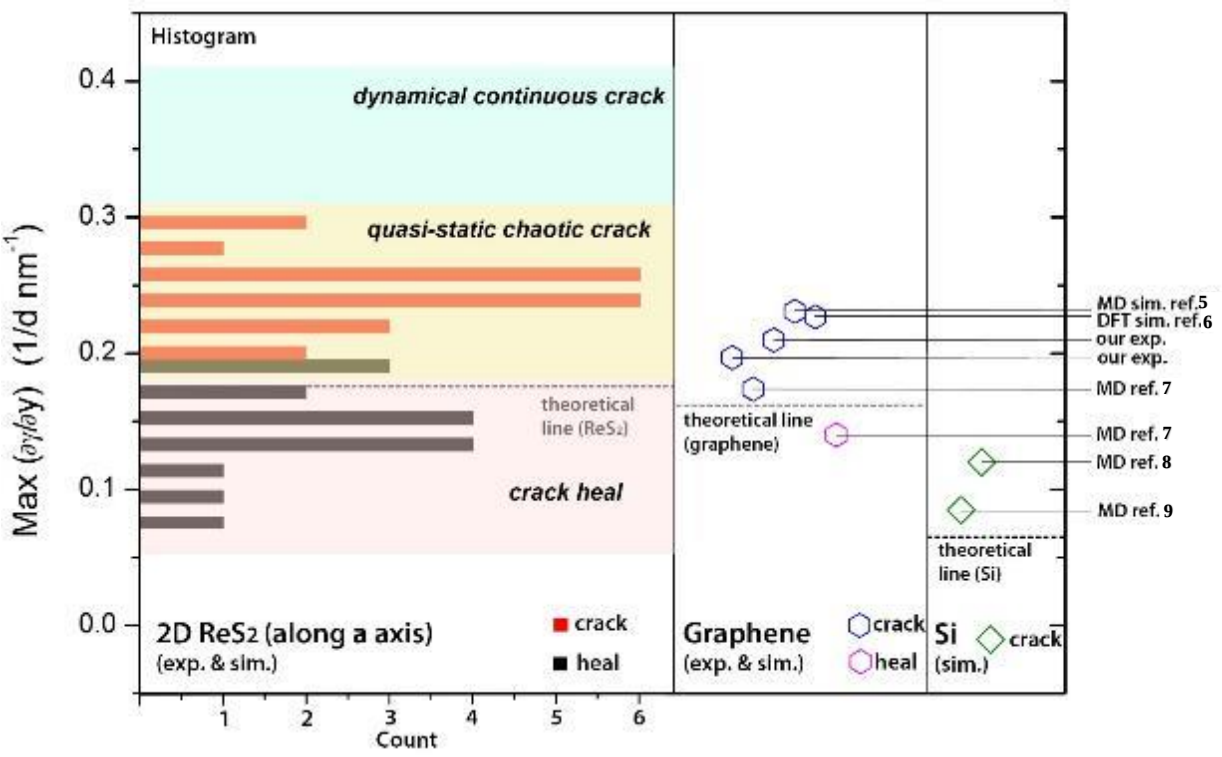

Figure 4.12 (Left panel) The histogram of maximum shear strain gradient in ReS_2 Mode I cracks by TEM experiments. Crack and heal are shown in red and black, respectively. Theoretical result is shown as dashed line. The crack dynamics regimes are highlighted in colors. (Middle panel) The shear strain gradient maxima data for graphene (experiments and simulations) Mode I crack and heal. (Right panel) The shear strain gradient maxima in silicon mode I crack based on simulation data.

dependent on K or the strain gradient maxima, but randomly distributed, showing the first characteristic of chaotic motion. More importantly, the frequency analysis on the crack steps in total 260 moves of the observed mode I cracks in ReS_2 shows a well-defined ($\sim(1/2)^s$) distribution, where *s* is the step length (Figure 4.13), implying the counts/frequency decay by

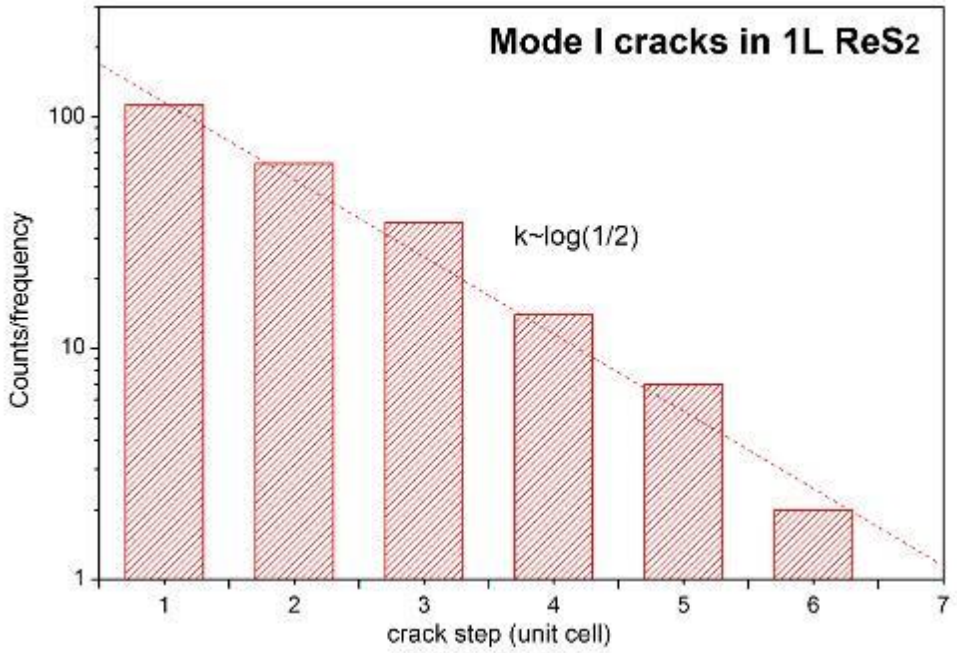

Figure 4.13 The experimental histogram of the crack steps by statistics on 260 moves of mode I crack in 1L ReS_2.

half after each unit cell crack extension. It shows that during crack of each unit cell, there are two attractors in the chaotic motion - the crack extend and stoppage. Therefore, in this regime (quasi-static crack), the possibility of crack propagation decreases by a factor of 1/2 after each unit cell propagation in the dynamic crack process within a single crack step. Furthermore, the crack path switching or crack direction switching and the emergent terraces/steps on cracked surfaces in entirely brittle materials are resulted from these chaotic processes. Accordingly, the

entire distribution of the fracture regimes (healing, quasi-static crack, continuous dynamic crack) for Mode I crack in monolayer (1L) ReS_2 can be summarized in Figure 4.12. Owning to the continuous dynamical crack are too fast to capture (well beyond the current capability of the current STEM imaging system), the boundary between the quasi-static crack and continuous dynamical crack remain unclarified. Nevertheless, our observations have set a lower bound for the continuous dynamical crack regime.

4.3.4 Summary

In summary, our *in situ* STEM observations have unveiled the atomic structure of dynamic crack tips. We observed entirely brittle fracture down to atomic scale without tip blunting. Beyond the asymptotic field in classical theories, the atomistic process in the singular crack tip zone is basically the sequential atomic bonding dissociation, so it is reversible under critical loading, and both cracking and healing can occur. We propose that the condition for atomic bonding rupture can be correlated with local strain gradient maxima, the latter serves as simple criterion for the brittle crack propagation or healing in atomic scale. These experiments open the avenue for the visualization of crack dynamics and contribute to the deep understandings of fracture mechanics of materials.

Reference:

1. Irwin, G. R. Plastic zone near a crack and fracture toughness, sugamore ordinance materials conference. *Syracuse, NY: Syracuse university research institute* **1961**.

2. Wiederhorn, S. M. Brittle fracture and toughening mechanisms in ceramics. *Annual review of materials science* **1984**, 14, 373-403.
3. Budarapu, P. R.; Javvaji, B.; Sutrakar, V. K.; Roy Mahapatra, D.; Zi, G.; Rabczuk, T. Crack propagation in graphene. *Journal of applied physics* **2015**, 118, 064307.
4. K. VijayaSekhar, S. G. Acharyya, S. Debroy, V. P. K. Miriyala, A. Acharyya, Self-healing phenomena of graphene: potential and applications. *Open physics.* **2016**, 14, 364-370.
5. Budarapu, P. R.; Javvaji, B.; Sutrakar, V. K.; Roy Mahapatra, D.; Zi, G.; Rabczuk, T. Crack propagation in graphene. *Journal of applied physics* **2015**, 118, 064307.
6. Zhang, Z.; Kutana, A.; Yakobson, B. I. Edge reconstruction-mediated graphene fracture. *Nanoscale* **2015**, 7, 2716-2722.
7. VijayaSekhar, K.; Acharyya, S. G.; Debroy, S.; Miriyala, V. P. K.; Acharyya, A. Self-healing phenomena of graphene: potential and applications. *Open physics* **2016**, 14, 364-370.
8. Swadener, J. G.; Baskes, M. I.; Nastasi, M. Molecular dynamics simulation of brittle fracture in silicon. *Physical review letters* **2002**, 89, 085503.
9. Hauch, J. A.; Holland, D.; Marder, M. P.; Swinney, H. L. Dynamic fracture in single crystal silicon. *Physical review letters* **1999**, 82, 3823.

Chapter 5 Critical Stable Length in Wrinkles of 2D Materials

5.1 Introduction

Contrary to the unstable nature of the conventional wrinkles, the stable wrinkle structures revealed in the 2D materials, causes by the van der Waals (vdW) interactions, means an energy barrier needs to be overcome before flattening. Furthermore, the minimum length (or height) for stabilizing the wrinkles of 2D materials can be determined both experimentally and theoretically. Particularly, some *in situ* TEM experiments have allowed the dynamic observations of rippling[1] or exfoliation[2] processes of 2D materials, but the dynamics of the wrinkle structures dependent on the lengths are unexplored, in part due to the difficulties regarding the loading fixture and the atomic-scale manipulation of 2D membranes. Standard flexural testing applies a two- to four-point fixture on the sample, [3,4] and the elastic modulus of bending, flexural strength and flexural stress-strain responses can be retrieved. [5-8] However, all the classical flexural methods apparently fail in cases of ultra-thin or ultra-flexible membranes due to the infinitesimal bending rigidity in membranes, which are not stable or self-standing during external perturbations, such as gravity or thermal fluctuations. [9-12] Indeed, similar with polymer molecules, the persistence length of atomic-thick 2D materials falls into the nanometre (nm) scale. [13,14] The basic bending shape of a monolayer was predicted by the energy analysis. Figure 5.1 illustrates the shape of monolayer bending curve is close to a circle

ring and the driven force is vdW interaction between adjacent graphene layers. Thus the energy of the whole wrinkle is formed by two parts: the energy of bending curvature and the energy of vdW cohesion layer. Combining the previous work on bending test and characterization of 2D materials, therefore, here we apply the atomic force microscopy (AFM) and direct *in situ* TEM approaches to understand the wrinkle dynamics and stability under thermal and mechanical perturbations.

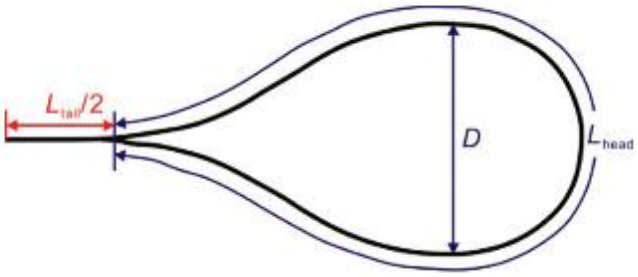

Figure 5.1 Schematic diagram of the geometry of self-folding monolayer graphene nanoribbon.[14]

5.2 Methods and Experiment

5.2.1 Sample preparation

Graphene was synthesized on a 75 μm thick copper foil (Goodfellow, England) using tube furnace (Nabertherm, Germany) in atmospheric pressure. The temperature in the tube was elevated to the growth temperature within 30 minutes, and samples were annealed at the growth

temperature for 2 hours with flow gases of 50 sccm H_2 and 50 sccm Ar. Monolayer graphene was synthesized with a flow of 50 sccm H_2, 10 sccm CH_4 (1% in Ar) and 1000 sccm Ar for 45 minutes. The sample was then cooled to room temperature while maintaining the 1000 sccm Ar flow. After synthesis, PMMA was spin-coated onto the graphene-grown Cu foil at 800 rpm for 10 seconds and then 3000 rpm for 1 minute. Copper etchant (Aldrich 667528) was used to dissolve the underlying copper. The PMMA-coated graphene was transferred onto the SiO_2/Si substrate. This sample was dried in a dry oven at 65 °C before PMMA was removed with acetone. Further, the graphene/SiO_2/Si substrate was put back to the tube furnace then annealed at 200 °C for 8 hours. Low vacuum of 2×10^{-2} mbar was maintained from beginning until cooling to room temperature. Before and after annealing, surface of transferred graphene was investigated by AFM. The topography and phase images were obtained using the AFM5300 system (Hitachi, Japan) in tapping mode. A NSC30-type silicon tip (Tipsnano, Estonia) with an approximately 10-nm tip curvature radius was used.

The multilayer graphene and MoS_2 membranes were produced by mechanical exfoliation from bulk ma-terials using adhesive tapes. Bulk graphene (ZYA Grade, provided by 2D Semiconductors Inc., USA) and TMDs were mechanically exfoliated into several layers on Scotch tape. Then, TMDs monolayers with good quality but small flakes could be dry-transferred on a TEM grid directly by the heat release tape method with clean surfaces. The grids are then fixed on an *in situ* TEM manipulation holder (NanofactoryTM) fitted in the JEOL 2100F TEM, while an electrochemically etched tungsten (W) tip is installed on the counter position, which can be finely piezo-controlled with a precision better than 0.1 nm in

three-dimensional (3D) space. The W tips used for the *in situ* TEM manipulator were made by electrochemical corrosion with a solution of 1 mol/L NaOH at a 2~3 V bias.

5.2.2 TEM Characterizations and Analysis

The TEM images and videos were collected on a JEOL 2100F transmission electron microscope under an accelerating voltage of 200 kV with a Nanofactory^{TM} STM-TEM holder. The bright-field TEM imaging in our *in situ* experiments was acquired via a 0.5s exposure time and electron dose lower than 0.1 A/cm^{-2}. The position of each wrinkle and corresponding *x* and *l* were measured from five different spots on the wrinkles and averaged. The pixel size is 2004*1336.

Form the captured video images of the samples, the carbon film is in ellipse but not circle. This shape is caused by the inclination of the sample for better contact with the W tip and the distortion of the carbon film under the force of the W tip. The value of the distortion can be calculated by the ratio of the major and minor axes of the ellipse, and obviously, the length of the wrinkle is along the minor axis. We need to take the distortion value into account during the measurement.

In addition, during the measurement, we notice that the moving direction of the W tip between each pair of frames is not exactly the same due to the rotation of ripples and the Nanofactory controller. To obtain the precise values, the movement of 5 different spots on the wrinkle is

measured each time and the average value is obtained. Additionally, the direction of wrinkles slightly changes from one direction to another. Furthermore, the distance of the two adjacent wrinkles is different from left to right, which causes a difference in the friction. Here, we also take the average values of several spots on the wrinkles. Other factors, such as the contamination on the sample and the influence of the electron beam, which can lead to errors, are minimized by the dry transfer method, low magnification and low electron dose observation of TEM, respectively.

5.2.3 Continuum Mechanics Model of Wrinkling

The bending moment at the start point of curvature is balanced by

$$M - M_R + fx = 0,$$

where M, M_R, and f are the bending moment at cut, the bending moment at the contact edge and the friction force between the top layer and the multilayer substrate, respectively. The expression of M is given by

$$M = D\frac{d\phi}{ds},$$

where D is the bending stiffness, which can be expressed by $D = \frac{Et^3}{12(1-v^2)}$; E is Young's modulus; v is Poisson's ratio and t is the effective thickness of the material. From the bending curvature of the sheet, we know $dx/ds = sin\,\phi$, $dy/ds = -cos\,\phi$. Deriving from the above equations, we have

$$\frac{d^2\phi}{ds^2} = -\frac{f}{D}\cos\phi,$$

Define $\gamma \equiv \sqrt{\frac{W_{ad}}{f}}$, $\Phi'(0) = \sqrt{\frac{W_{ad}}{D}}$, where W_{ad} is the adhesion energy between two vdW layers, which can be regarded as the boundary condition since it balances the adhesion energy and strain energy. Given a value of γ, the curvature of the sheet under a certain value can be determined and fitted with experiments, which represents the shape of the graphene wrinkles. In addition to the flexural texting on graphite substrate, we also simulate the flexural on SiO_2 substrate. The main difference between graphite and SiO_2 as the substrate is the adhesion energy of graphene with them, which makes slight change in boundary conditions in the model.

In our modelling, the value of W_{ad}, f and the energy calculation are apparently determined by the materials and contact of the bottom, as shown in Figure 5.2. For monolayer graphene with the graphene substrate, it is not difficult to find the related parameters from the results of experiments and calculations. However, it can be complicated when deciding the parameters in a freestanding monolayer. More calculation and dynamical tests are needed to obtain an accurate value of W_{ad} since the supporting force is derived from the unpeeled part connected with the whole membrane and the carbon film under the sample.

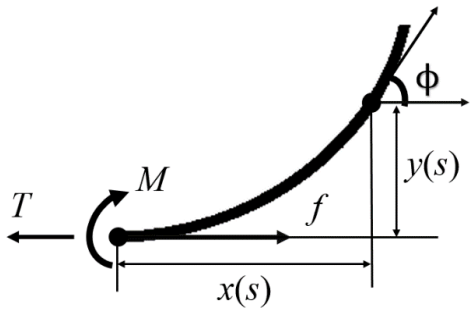

Figure 5.2 Schematic diagram of the mechanical directions of the bended monolayer graphene.

From the equations above, the boundary conditions decide the shape of wrinkles in different cases during modelling. During the exfoliation and recovery process of monolayer graphene in the main text, the movement of the wrinkle is controlled by the W tip. For the curvature of the wrinkle, one side is connected with the whole graphene flake so it always starts with the boundary condition $\phi(0) = 0$, as well as $x(0) = 0$, $y(0) = 0$. Another boundary condition is $\phi'(0) = \sqrt{\frac{W_{ad}}{D}}$, as a result of J-integral, stationary potential and material force balance. From the normalization of *x*, *y*, *s*, and ϕ, the curvature of wrinkles under different values of *f* (friction force) can be determined, which corresponds to the wrinkle state under the force applied by the W tip. There is a slight change in the boundary conditions. Both sides of the edge are flexible and can move, so $x(0) = 0$ is unsuitable. The way in which the W tip contacts the sample is not from the bottom but from the side, so the end connected with the W tip cannot reach $\phi(0) = 0$ and the curvature of the first wrinkle is less than a whole period. Meanwhile, there is no friction force between the wrinkles and substrate due to the dangling ripple. Nevertheless, additional dynamical tests are needed to determine the mechanical properties of these unknown materials in further studies.

5.3 Results and Discussions

5.3.1 Thermal Effect on Graphene Wrinkles

In the first experiment, the thermal stability of wrinkles in monolayer graphene is examined in Figure 5.3a. The large-area graphene samples used are grown by the CVD method and transferred onto the SiO_2/Si wafers by a PMMA transfer process[15] which has been routinely used in the processing of 2D materials.

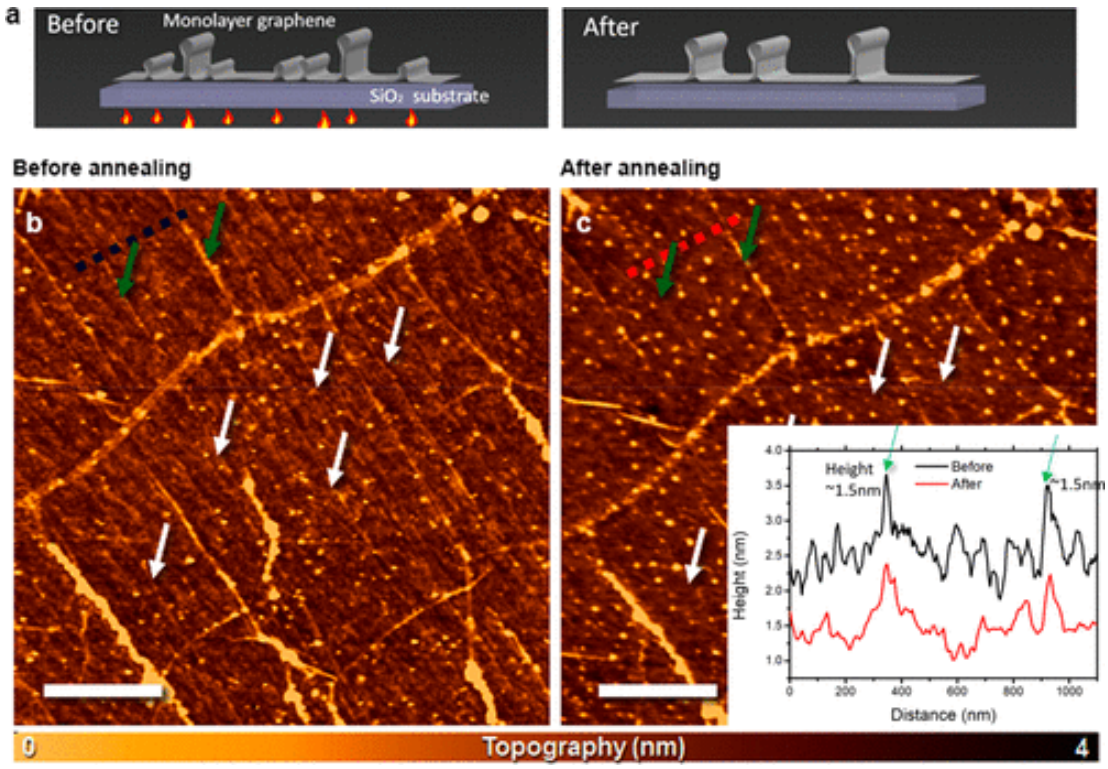

Figure 5.3 Thermal annealing effect on graphene wrinkles. (a) Scheme of the monolayer graphene under thermal annealing. Wrinkles with lengths below a critical value are removed, while wrinkles with lengths above a critical value are stable. (b, c) AFM topographic images of the same position of a monolayer graphene sample, before and after annealing. Wrinkles with lengths above a critical value (e.g., green arrows marked) over 1.5 nm in height are stable during annealing, and wrinkles with lengths below a critical value (e.g., white arrows marked) less than a critical length are removed by thermal annealing. The inset of (c) shows the height profiles for the dashed line positions of AFM images in (b) and (c); black and red lines are before and after annealing, respectively. Scale bars = 1 μm.

As usual, the morphology of monolayer graphene on SiO_2 is found to be quite rough on the nanoscale. Figure 5.3b shows a typical AFM topographic image for the transferred monolayer graphene sample. On the random graphene wrinkles formed by the natural transferring, the

preferable directions for wrinkling are also predominantly zigzag or armchair as shown in Figure 5.4. The crossed parallel stripes are the wrinkle patterns induced naturally during

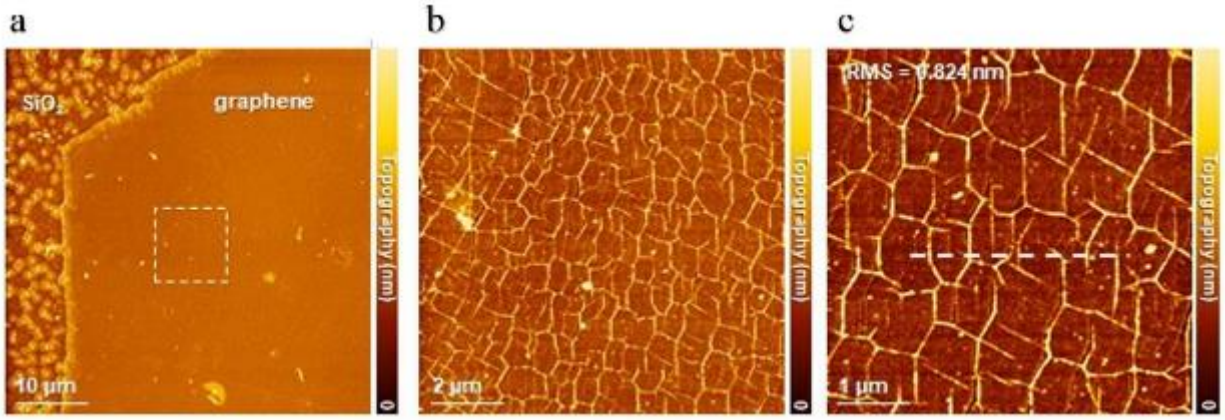

Figure 5.4 The wrinkles formed on SiO_2 after transfer, AFM topographic images with three magnifications for the same area (white dashed rectangle).

PMMA transfer, which are tiny and close to equilibrium. They are different from the wrinkles in fixed end types with considerable strain (Figure 5.5). The wrinkles formed after transfer

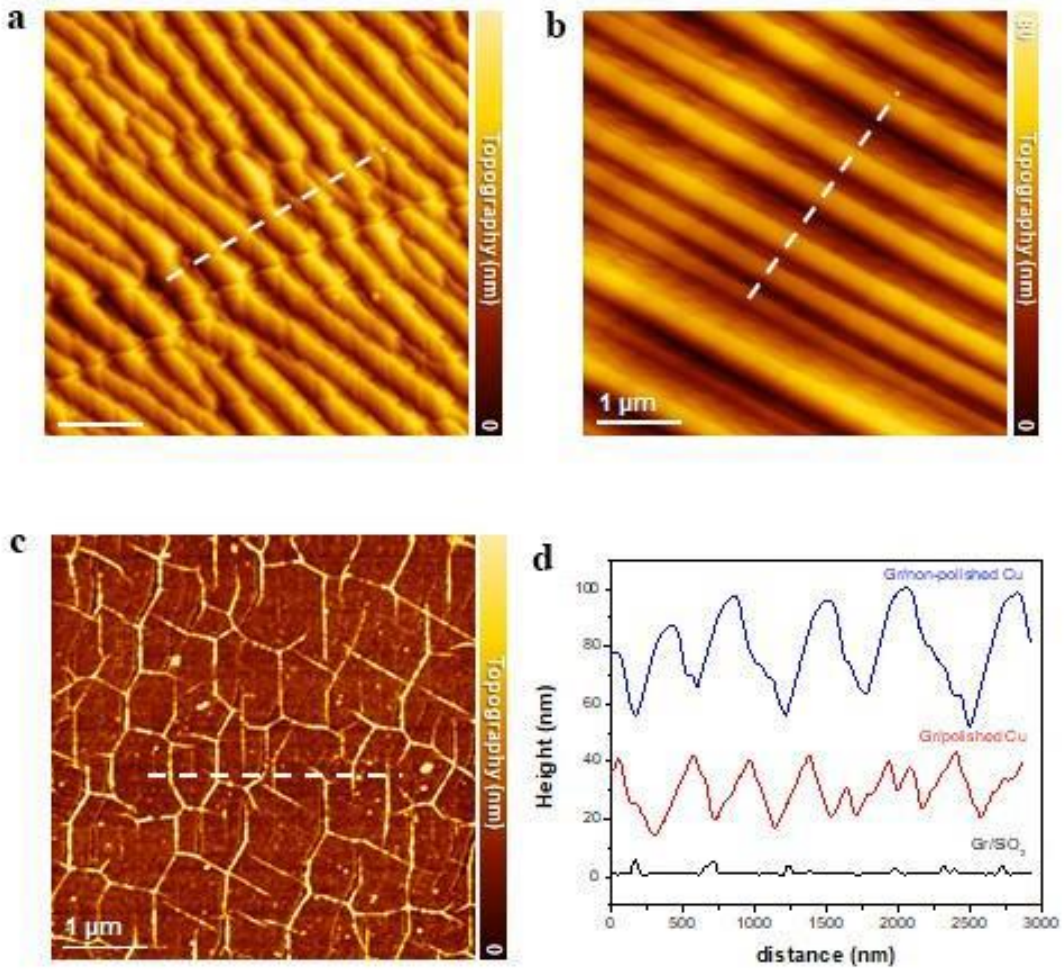

Figure 5.5 (a-c), The AFM topographic image for the 1L graphene on polished Cu, 1L graphene on non-polished Cu, and 1L graphene on transferred SiO_2 substrate. (d), The height profiles corresponding to the white dashed lines in (a-c).

are much smaller than the original terraces/steps of Cu foils. The smaller wrinkles after transfer does not follow the direction of any surface steps, instead, they follow the graphene lattices, zigzag or armchair directions (two energy favorable directions for wrinkle formation), therefore, the angles between wrinkles in Figure 5.5c are 30°, 60°, 90°, 120° and 150°. The graphene growth on polished Cu foil still have parallel and sparse wrinkles because of the

different thermal expansion coefficient between graphene and Cu foil, these wrinkles mainly follow the surface terraces/steps of the Cu, and they are much higher (10~50 nm height) than the lower wrinkles (1~5nm height). The spikes on the AFM line profile (Figure 5.5b) correspond to the position and height (distance from the top of a wrinkle to the substrate) of the individual wrinkles. The height of wrinkles spans from 0.1 to 1.7 nm with a sample roughness of *ca*. 0.7 nm. After thermal annealing at 200 °C for 8 h, the same sample position is checked using AFM (Figure 5.5c). The original big wrinkles (height over 1.5 nm) are unaffected by the thermal annealing, while the small wrinkles are mostly eliminated or combined with big wrinkles.

5.3.2 *In Situ* TEM Wrinkling Tests

In our *in situ* TEM test conducted later, multilayer graphene samples are mechanically exfoliated from highly ordered pyrolytic graphite (HOPG) crystals using Scotch tape. The selected area electron diffraction (SAED) pattern of multilayer graphene exhibits good crystallinity in the samples and facilitates crystal direction identification in the flakes. The *in situ* TEM manipulation holder (Nanofactory^{TM}) with a precision better than 0.1 nm in 3D space is employed (Figure 5.6a). In the first step, an electrochemical etched W tip is controlled by the piezo-manipulator and is firmly pressed on the top surface of the multilayer (layer number >10, counted at edge) graphene (Figure 5.6b, c). Then, the W tip (less than 5 nm by 5 nm) intentionally scratches along the graphene surface until a one-nm crack emerges on the top layer of graphene. Afterwards, the W tip is laterally moved on the flake surface for further

tearing of the top graphene layer until it is gradually exfoliated from the multilayer underneath (Figure 5.6b). The monolayer thickness of the exfoliated layer is confirmed directly at the flake edge, and no additional exfoliation in the separated top layer can be seen with further manipulation. The initial crack edge in the top layer is adsorbed/connected to the W tip. Following the initial exfoliation, sequential wrinkles are spontaneously formed in the top monolayer (Figure 5.6b) by vdW interactions. The wrinkle direction is along the zigzag direction, as confirmed by SAED. Owing to the three-fold symmetry of graphene, the bending properties can be considered almost isotropic in the basal plane.[16]

After several wrinkles are shaped, the movement of the W tip is reversed in the opposite direction, namely, the recovery direction (Figure 5.6d, e). A straight stripe with sharper contrast starts to replace the previous obscured wrinkled images (Figure 5.6f, red triangle marks). This observation agrees with our following analysis, indicating that a self-standing wrinkle with a regular shape between two vdW contacts is naturally formed. Afterwards, the W tip is further moved along the recovery direction, thus resulting in the gradual shortening of the total wrinkle length (l) and height, manifested by a decrease in the stripe contrast (Figure 5.6f). Next, a quick drop in the wrinkle image contrast and wrinkle length led by the continuous movement of the W tip (last snapshot in Figure 5.6f) shows the entire recovery of the wrinkle. Interestingly, after recovery, the image contrast in the exfoliated top layer and the adjacent perfect part are almost the same, implying that the wrinkle has perfectly recovered. Notably, other wrinkles with the W tip demonstrate no appreciable change in morphology during manipulation.

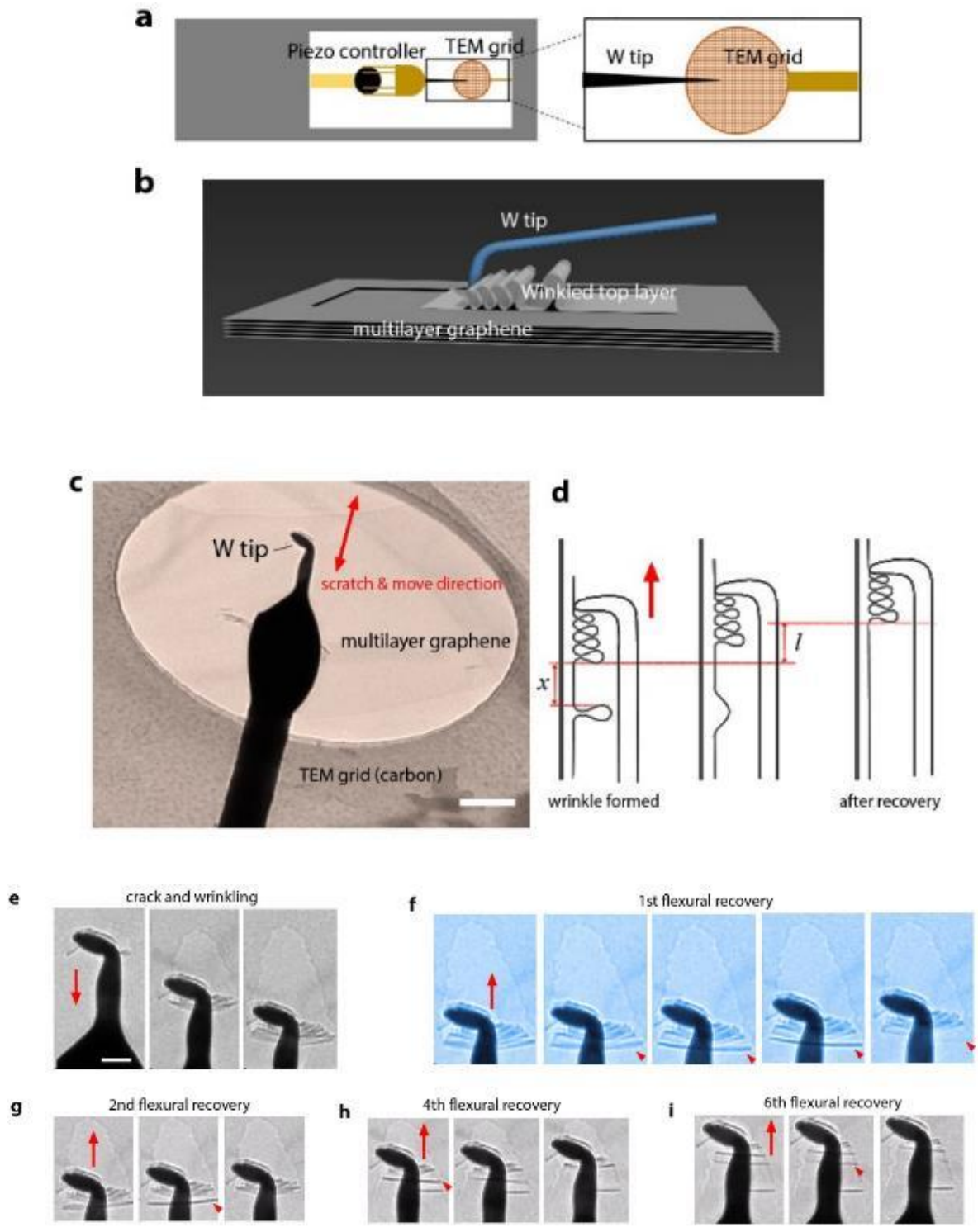

Figure 5.6 The *in situ* TEM flexural tests on supported monolayer graphene. (a) Scheme for the *in situ* TEM setup. (b) Scheme for the exfoliation, wrinkling and manipulation on the surface top layer of graphene. (c) TEM image of the suspended multilayer flake and W tip, red arrow shows

the tip moving direction, scale bar 100 nm. (d) Sequential scheme for the recovery flexural test and nomenclatures. (e) Sequential TEM micrographs for the cracking and wrinkle formation, scale bar 30 nm and following TEM images (f-i) at the same magnification. (f-i) Serial TEM micrographs show the recovery flexural tests for the 1st, 2nd, 4th and 6th times, respectively; the red arrows mark the tip moving directions; and the red triangles highlight the specified wrinkles under testing.

After the first recovery is completed, the W tip is further moved along the recovery direction. Since a few more wrinkles are reserved during the tearing process, a total of seven similar recovery processes are completed in this experiment (Figure 5.6g-i shows three of them). After the last few recoveries (Figure 5.6h, i), some short wrinkles remain close to the cracks/edges due to a slight rotation in the top layer with respect to the multilayer underneath. In addition, the recovery mainly occurs when the sliding contact area (area denoted by x in Figure 5.6d) is small; once the contact area increases after sliding, some remaining wrinkles can be "locked" due to high frictional forces.

5.3.3 Statistic Calculation of Wrinkles

The observed continuous manipulation can be quantified via measurements on the physical positions of the wrinkles, including the wrinkles due to ongoing tests and their adjacent wrinkles. For the convenience of analysis, here we define the total length of a wrinkle (denoted as l) as the integrated curved length excluding the underlying flat length, which can be determined by the variation in the positions (prior to/after recovery) of the adjacent wrinkles (Figure 5.6d). During the manipulations, based on our measurements, the lengths of all the

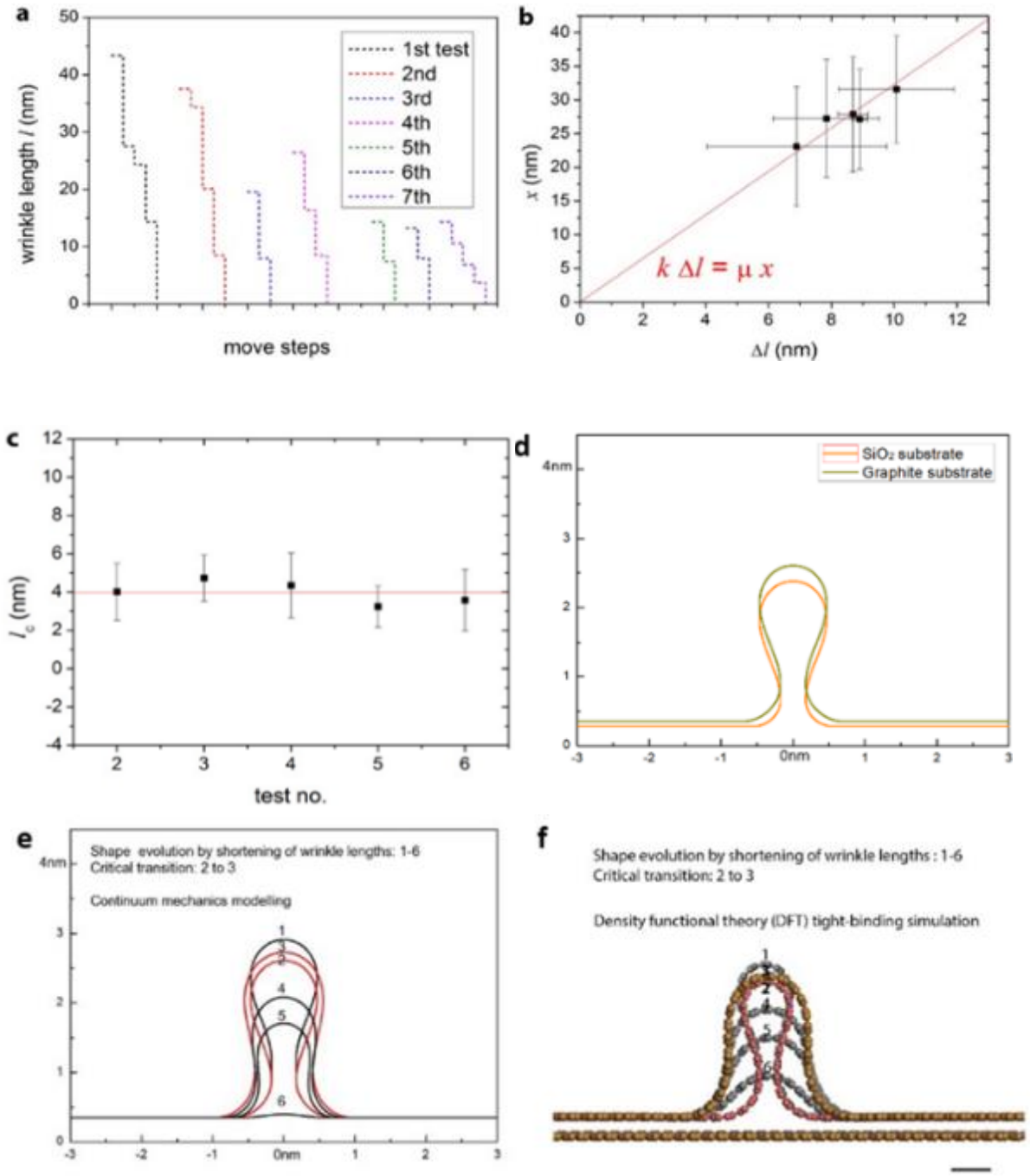

Figure 5.7. The results of TEM tests and analysis of the flexural behaviour of monolayer graphene. (a) The stick-slip motion (wrinkle lengths) for each test. (b) Linear relationship between the change step of the wrinkle lengths (Δl) and sliding contact area (x). (c) The measured critical wrinkle lengths (after subtraction of the last move of the W tip). (d) The critical wrinkle states on graphite and SiO_2 substrates. (e) The continuum mechanics models for the wrinkles at different lengths (length shrinking from state 1 towards state 6), unclip critical

transition between state 2 and state 3. (f) The DFTB simulation results for the monolayer graphene wrinkles at different lengths (length shrinking from state 1 towards state 6) and the unclip critical transition between state 2 and state 3 (scale bar 0.5 nm).

wrinkles are stepwise shortened (the last few steps for each wrinkle are shown in Figure 5.7a). The corresponding distances between the last two wrinkles (Figure 5.6d), the same as the area of the sliding contact zone (x), are recorded as well. Although the continuous movement of the W tip is piezo-controlled with a constant speed and precision as high as 0.1 nm, a stick-slip behaviour in the sliding is observed. The lattice-commensurate vdW contact between the two vdW bearings introduces a frictional force (f), which is proportional to the contact area x.[17] Thus, the distance or step of each "stick-slip" move (Δl) can be expressed as

$$f = k\Delta l = \mu x, \quad (1)$$

where k is the (lateral) force constant of the W tip and μ is the friction coefficient between the vdW layers. The above linear dependence of each stick-slip movement on the contact area coincides with our experimental results (Figure 5.7b). Each x and l are statistically measured from multiple positions on the wrinkles. Moreover, by excluding the distance of the last stick-slip frictional movement, the critical lengths (l_c) for the wrinkles before the last flattening step (drop to zero of l) are shown in Figure 5.7c (the distances in the last move of the W tip are subtracted according to eq. 1 and Figure 5.7b). The results are surprisingly close to a common threshold length of ca. 4.0 nm, which is due to the specular mechanical responses in the top graphene layer.

A linear continuum mechanics model[18] can be applied and verified on monolayer graphene[19]. The differences between graphene on SiO_2 in our first experiment and graphene on multilayer graphene in the second experiment is just the different vdW interactions with the substrates (Figure 5.7d). The shapes of the wrinkles with minimized energy at different total lengths (l) are exhibited in Figure 5.7e. For the bending rigidity and the vdW interlayer energy of graphene, widely accepted experimental values are adopted.[20,21] A clear transition from the "clip" shape (Figure 2.15e, state 1 to state 2, also called type 3 shape) to the "bump" shape (state 3 to state 6, also called type 2 shape) is denoted. A transition occurs near the wrinkle length (l) of 4.1~4.3 nm for the multilayer graphene case (l_c=3.9 nm for graphene-SiO_2 case). The strain forces restored in the wrinkles are calculated and presented in the supplementary materials. In long wrinkle cases, due to vdW adsorption, the clipped wrinkles (type 3) are stabilized and no strain is applied to the two vdW contact bearings; however, after the critical transition (state 2 to state 3), considerable shear strain is set in the contact bearings due to the bending strains in the top layer. Thus, the wrinkles become unstable and are liable to be flattened if the frictional vdW forces are insufficient to balance the bending strains. Comparing the results of modelling with our AFM and *in situ* TEM experiments on the critical height/length of the wrinkles, the height by AFM (critical height ~1.5 nm) has larger error with the 2.3 nm by modelling, possibly resulted from the larger friction at the graphene-SiO_2 interface, while the *in situ* TEM results (l_c~4.0 nm) coincides well with the results (l_c =4.1~4.3nm) of modelling.

To further confirm the wrinkling behaviour, the structural optimizations of the wrinkles are carried out by the self-consistent charge density functional tight binding (SCC-DFTB)

method.[22,23] The longest length of the wrinkles is set from approximately 6 nm to accommodate the clipped wrinkles (Figure 5.7f, states 1 and 2) until the shortest single unit cell (l=0.24 nm) wrinkle (Figure 5.7f, state 6), which actually becomes an edge dislocation. The short wrinkles can indeed be considered a dislocation or a rip location in 2D.[24,25] The relaxed wrinkled structures in monolayer graphene are in agreement with the previous continuous mechanics models (Figure 5.7e, f). According to the continuous mechanical model and DFTB simulation, the transition between the clip state to the bump state (Figure 5.7f, critical transition from state 2 to state 3) occurs at a wrinkle length of approximately 3.8 nm. Therefore, the experimental results (4.0 nm) again largely agree with the DFTB results (3.8 nm) for the critical transition point of "unclipping" and strain release.

Except for the bended shapes and total wrinkle lengths, which are in equilibrium, the dynamical positions of wrinkles under testing exhibit an interesting dependence on the wrinkle lengths as well. The displacement of the wrinkles (Δx) versus the total wrinkle length change (Δl) at different wrinkle lengths (l) in our experiments is shown in Figure 5.8a. With the pulling forces (see schematic Figure 5.8b) by the W tip, the wrinkles slowly move along the recovery direction. The pulling effect (defined as $\Delta x/\Delta l$) on the wrinkle decreases with reduced wrinkle lengths. Short wrinkles have Δx=0 in recovery due to the direct momentum transfer to the whole wrinkle and frictionless dynamics in the clipped areas (Figure 5.8b). In contrast, for long clipped wrinkles, the recovery process tends to cause no relative sliding between the two clipped sides of the wrinkles (Figure 5.8b). Therefore, the wrinkles in the long length limit will

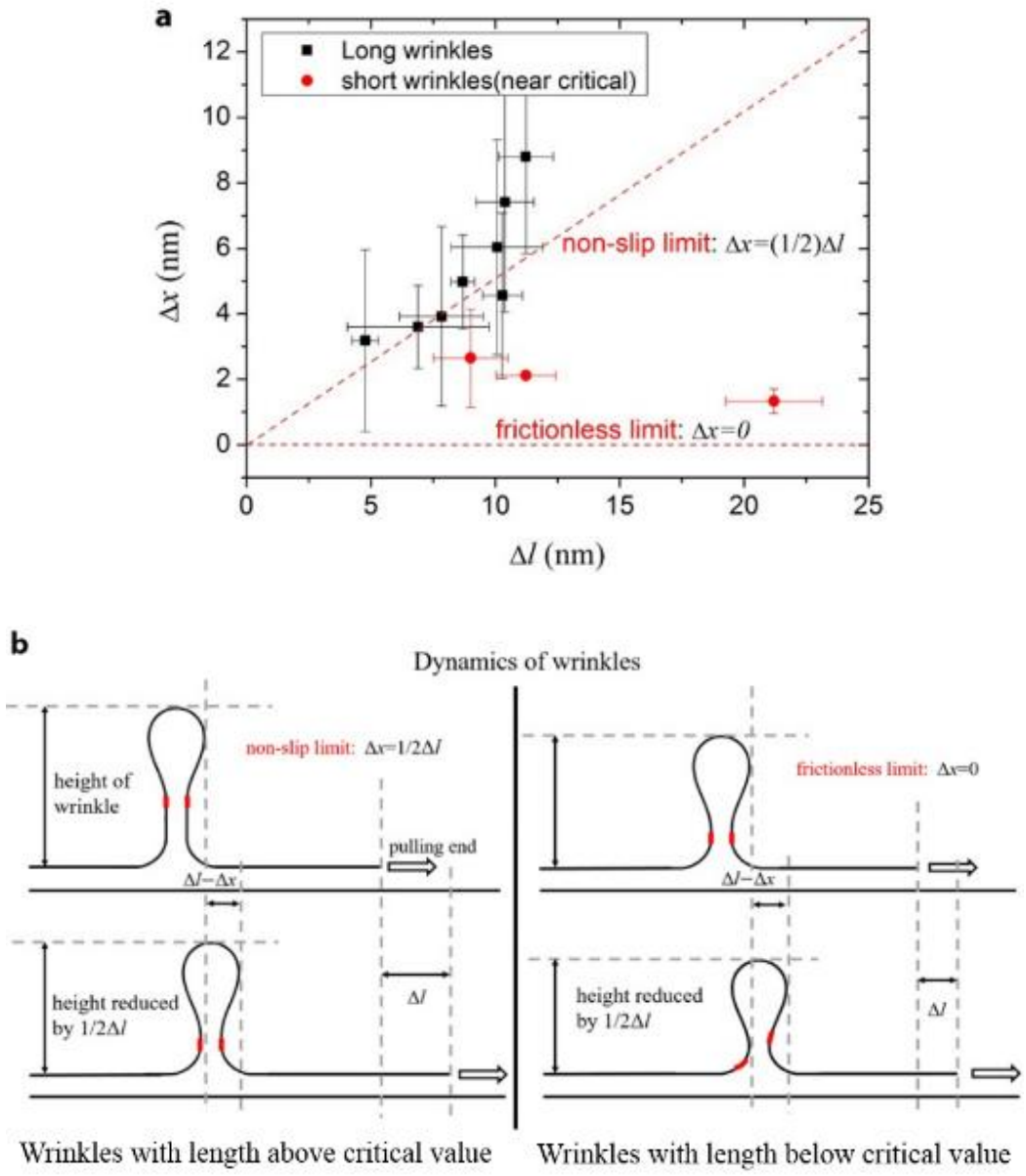

Figure 5.8 The experimental dynamics of the wrinkle position and lengths. (a) The experimental relationship between the length change and position change. The oblique and horizontal lines represent the non-slip limit and frictionless limit, respectively. (b) The schematics for the wrinkle dynamics in two limit cases (left and right). The red sections on the wrinkles labelled the same position on the wrinkle before and after pulling, respectively.

have the maximum $\Delta x/\Delta l$ equal to 1/2 (Figure 5.8b), which is consistent with our experimental observations (Figure 5.8a). The *in situ* monitoring of the entire wrinkling and dewrinkling process provides important additional insights. To further improve the test setting, the manipulating tip with a larger force constant can be sought, which means that the stick-slip steps will be finer; hence, the dynamics close to the critical threshold of state transition during the entire testing can be more clearly unravelled.

5.3.4 Summary

In conclusion, the experiments here directly exhibit the wrinkling and dewrinkling process of graphene, the concepts here can be readily generalized to other vdW layered 2D materials. Wrinkles can either facilitate or deteriorate the performances, depending on the way they are treated. The 2D materials com-munity is always keen to the flatness and uniformity, but also enthusiastic for the flexibility. The obtained critical lengths for wrinkling/dewrinkling here is expected to have profound impacts in the future development of flexible electronic/optoelectronic devices, nanoelectromechanical systems (NEMS) and other related fields.

References:

1. Ludacka, U.; Monazam, M. R. A.; Rentenberger, C.; Friedrich, M.; Stefanelli, U.; Meyer, J. C.; Kotakoski, J. In situ control of graphene ripples and strain in the electron microscope. *2D materials and applications* **2018**, 2, 25.
2. Tang, D. M.; Kvashnin, D. G.; Najmaei, S.; Bando, Y.; Kimoto, K.; Koskinen, P.; Golberg, D. Nanomechanical cleavage of molybdenum disulphide atomic layers. *Nature communications* **2014**, 5, 3631.
3. Landau, L.; Lifshitz, E. Theoretical Physics. Vol. 3. Continuum Mechanics. *Pergamon Press, Oxford* **1944**.
4. Mujika, F. On the difference between flexural moduli obtained by three-point and four-point bending tests. *Polymer testing* **2006**, 25, 214-220.
5. Boukhili, R.; Hubert, P.; Gauvin, R. Loading rate effect as a function of the span-to-depth ratio in three-point bend testing of unidirectional pultruded composites. *Composites* **1991**, 22, 39-45.
6. Quinn, G. D.; Sparenberg, B. T.; Koshy, P.; Ives, L. K.; Jahanmir, S.; Arola, D. D. Flexural strength of ceramic and glass rods. *Journal of testing and evaluation* **2009**, 37, 222-244.
7. Combes, S. A.; Daniel, T. L. Flexural stiffness in insect wings II. Spatial distribution and dynamic wing bending. *Journal of experimental biology* **2003**, 206, 2989-2997.
8. Yoo, D. Y.; Yoon, Y. S.; Banthia, N. Flexural response of steel-fiber-reinforced concrete beams: Effects of strength, fiber content, and strain-rate. *Cement and concrete composites* **2015**, 64, 84-92.
9. Castellanos-Gomez, A.; Singh, V.; van der Zant, H. S.; Steele, G. A. Mechanics of freely-sus-pended ultrathin layered materials. *Annalen der physik* **2015**, 527, 27-44.

10. Huang, R., Stafford, C. M.; Vogt, B. D. Effect of surface properties on wrinkling of ultrathin films. *Journal of aerospace engineering* **2007**, 20, 38-44.
11. Bao, W.; Miao, F.; Chen, Z.; Zhang, H.; Jang, W.; Dames, C.; Lau, C. N. Controlled ripple tex-turing of suspended graphene and ultrathin graphite membranes. *Nature nanotechnology* **2009**, 4, 562-566.
12. Fournier, J. B.; Ajdari, A.; Peliti, L. Effective-area elasticity and tension of micromanipulated membranes. *Physical review letters* **2001**, 86, 4970.
13. Fasolino, A.; Los, J. H.; Katsnelson, M. I. Intrinsic ripples in graphene. *Nature materials* **2007**, 6, 858-861.
14. Xu, Z.; Buehler, M. J. Geometry controls conformation of graphene sheets: membranes, ribbons, and scrolls. *ACS nano* **2010**, 4, 3869-3876.
15. Gao, L.; Ni, G. X.; Liu, Y.; Liu, B.; Neto, A. H. C.; Loh, K. P. Face-to-face transfer of wafer-scale graphene films. *Nature* **2014**, 505, 190–194.
16. Lu, Q.; Arroyo, M.; Huang, R. Elastic bending modulus of monolayer graphene. *Journal of physics D: Applied physics* **2009**, 42, 102002.
17. Enachescu, M.; Van den Oetelaar, R. J. A.; Carpick, R. W.; Ogletree, D. F.; Flipse, C. F. J.; Salm-eron, M. Observation of proportionality between friction and contact area at the nanometer scale. *Tribology letters* **1999**, 7, 73.
18. Yakobson, B. I.; Brabec, C. J.; Bernholc, J. Nanomechanics of carbon tubes: instabilities beyond linear response. *Physical review letters* **1996**, 76, 2511.
19. Wang, C. Y.; Mylvaganam, K.; Zhang, L. C. Wrinkling of monolayer graphene: a study by molecular dynamics and continuum plate theory. *Physical review B* **2009**, 80, 155445.

20. Zhao, J.; Deng, Q.; Ly, T. H.; Han, G. H.; Sandeep, G.; Rümmeli, M. H. Two-dimensional mem-brane as elastic shell with proof on the folds revealed by three-dimensional atomic mapping. *Nature communications* **2015**, 6, 8935.
21. Lu, Q.; Arroyo, M.; Huang, R. Elastic bending modulus of monolayer graphene. *Journal of physics D: Applied physics* **2009**, 42, 102002.
22. Elstner, M.; Porezag, D.; Jungnickel, G.; Elsner, J.; Haugk, M.; Frauenheim, T.; Seifert, G. Self-consistent-charge density-functional tight-binding method for simulations of complex materials properties. *Physical review B* **1998**, 58, 7260.
23. Aradi, B.; Hourahine, B.; Frauenheim, T. DFTB+, a sparse matrix-based implementation of the DFTB method. *The journal of physical chemistry A* **2007**, 111, 5678-568.
24. Kushima, A.; Qian, X.; Zhao, P.; Zhang, S.; Li, J. Ripplocations in van der Waals layers. *Nano letters* **2015**, 15, 1302-1308.
25. Rappé, A. K.; Casewit, C. J.; Colwell, K. S.; Goddard III, W. A.; Skiff, W. M. UFF, a full periodic table force field for molecular mechanics and molecular dynamics simulations. *Journal of the American chemical society* **1992**, 114, 10024-10035.

Chapter 6 Summary and Outlook

In this thesis, we studied four types of mechanical behaviors in 2D materials: GBs, phase transition, fracture and wrinkling. Graphene and MoS_2 are used for the wrinkling behavior, ReS_2 is used to observe the atomic structure in fracture, grain boundaries and phase transition due to its anisotropic orientation. We mainly use (S)TEM to obtain the clear images of atomic structures in nanoscale so the movement of every single atom can be tracked. For mechanism, strain analysis with different mechanical modellings is applied on statistic calculation and corresponding dynamical properties can be analyzed. DFT calculations are conducted to compare the theories with experimental results and explain the change of energy in atomic scale during the formation of various defects.

In classical materials science, the mechanical twinning requests higher stress than slip mediated by dislocations in polycrystalline materials. Thus, the TBs or GBs can be used for dislocation pinning and for material strengthening. We discovered that in 2D materials, the GBs can be more mobile than dislocations and can be inversely pinned by the immobile dislocations. It has been previously found the anisotropic 2D material ReS_2 consists of "domain" structures. However, the kinetics of these domain boundaries have been overlooked. Distinct from all the previously reported GBs in all the other 2D materials as well as the 3D bulks, the GBs in 2D ReS_2 have three main new features: (1) Easily generated and mechanically driven, shear angle of crystal planes during certain GB formation/movement can be ultrasmall. (2) Can be pinned by either dislocations or sulfur sub-lattices. (3) The misfit strain at the (low index) incoherent GBs and high mobility. We employed HRRDF-STEM, DFT simulations and *in situ*

(S)TEM techniques, fully exploited atomic structures for all kinds of GBs in 2D ReS_2 and completed their classifications. In view of the lowest symmetry in 2D materials for ReS_2 and the most complicated GB structures in 2D, a library of GBs in 2D materials has now been established.

The phases of solid materials usually become disturbed under thermodynamic conditions such as temperature, pressure, electric or magnetic fields. For materials without obstacle in phase transition, the phase structures tend to transform into a more stable state. In another work, we recorded the motion of 2D ReS_2 with *in situ* aberration corrected (S)TEM, from which the motion of each single atoms was revealed clearly in real-time. Remarkably, we used the electron beam irradiation as the thermodynamic source to eliminate the external disturbance and proved the energy from irradiation can accomplish the phase transition process without damaging the sample. The continuous nanoscale images enable the analysis on atomic defects, dislocation and lattice distortion during the growth of new phase, which are closely related to the scanning directions of electron beam. For monolayer ReS_2 sample, we obtained the diamond chain structures of three different phases: the pristine anisotropic $1T^{''}$ phase, $1T^{'}$ with P21/m space group symmetry and P-3m1 symmetric 1T phase. The corresponding bandgap energy as well as energy for phase patterning from calculations were also identified.

For the fracture in 2D materials, the tests are conducted in both monolayer and bilayer ReS_2. Through high-resolution (S)TEM observations, the atomic reconstruction process of the fracture is successfully analyzed in three fracture modes. 2D ReS_2 produces a lattice

reconstruction process near the fracture. A high-resolution STEM image of the 2D ReS_2 fracture is observed in Mode II. Due to the shear stress, the films on both sides near the fracture can be automatically stitched to form an atomic-wide stack. Affected by the out-of-plane shear stress, a lattice reconstruction process different from Mode I can occur in 2D ReS_2 under Mode III fracture. The results directly reveal that due to the special dimensional effect of 2D materials, the shear stress reduces. Under this influence, lattice reconstruction occurs on the tip of the fracture and interacts with the fracture process of the material, which increases the brittleness of 2D material. This work also observes the special Mode II in-plane shear fracture in the 2D material. The model proposes a new method of manufacturing atomic-level stacks of 2D materials. Apart from these, the atomic strain at the tip of a crack consisting of only a few atoms is measured. This provides experimental evidence for understanding how the atoms at the tip of the crack can withstand excessive strain before the chemical bond breaks. Experiments directly show that due to the lattice constraint, the crack propagation occurs discretely on the atomic scale (as opposed to the continuous crack propagation in continuum mechanics). *In situ* experiments have also clarified the local atomic structure of the crack tip. The method in this experiment allows people to build theoretical models with unprecedented spatial resolution and strain accuracy to predict the mechanical properties of materials. It has a deeper understanding of the fracture mechanism of low-dimensional materials such as 2D materials, paving the way for the practical application of 2D materials in the future.

In flexural test, we innovatively performed the direct *in situ* TEM experiments on the flexural bending of the membrane. The mechanical properties revealed by *in situ* TEM show a strong relevance to vdW force and dynamical properties. It breaks the limit and achieves the ultrathin

thickness prohibited normal mechanical tests on these atomic membranes. In the ultra-thin membranes, the bending rigidity cannot bear stability and self-standing against external perturbations. We observed the complete formation and recovery process of wrinkles of 2D monolayer membranes in nanoscale under external manipulations. We discovered that: (1) The continuous flexural test on 2D materials can be achieved by a vdW sliding fixture method, which give well-reproducible results. (2) The bending and wrinkling in this range of 2D materials are totally elastic and recoverable. (3) The buckling processes occur during the formation and recovery of 2D wrinkles. The flexural properties can be retrieved from these tests. The flexural mechanics displayed here will greatly benefit the fundamental studies of 2D atomic structures and promote more applications in 2D. The interesting and innovative experimental design and the significance of the basic mechanics in this work provides new method of flexural test in nanoscale.

All the works above provide new ways of the *in situ* direct observation on structural and dynamical properties of 2D materials. The series (S)TEM image recording allows the analysis on the continuous atomic movement in the scanning area. The challenge is mainly about the control on the electron beam energy. At the present stage, energy provided by electron beam irradiation to create defects on 2D materials is not easy to quantify, and the mechanical defects generated in this case are limited. Possibility of applying an external strain directly on materials with nanoscale precision can broaden the discovery of mechanical behaviors and structural properties under (S)TEM, as well as calculate the dynamical properties of 2D materials. The equipment deciding the resolution of (S)TEM such as Cs correctors can also be improved, thus not only metal atoms but also lighter elements atoms can be observed clearly. It can lead to a

better vision on the formation of defects and determine the change of energy. Apart from this, there are more structures and phases in 2D materials still under exploration, a deeper understanding with a more completed library of materials is the main goal of future study.